Optimal UAV Approaches in Wind-Affected Maritime Operations

Trajectory optimization of an unmanned helicopter to a ship's deck in various wind conditions

D. Zilver

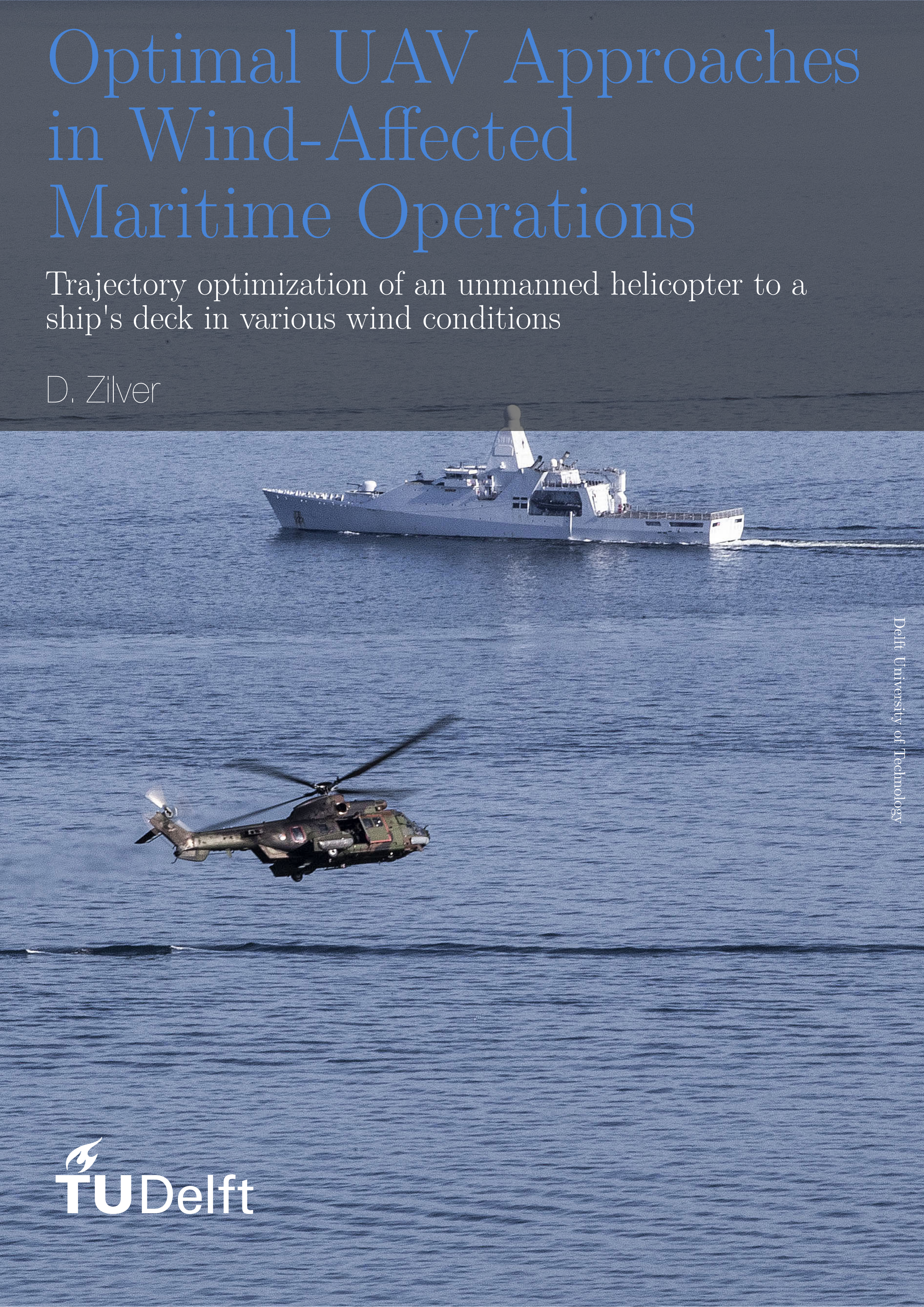

Delft University of Technology

This page is intentionally left blank.

Optimal UAV Approaches in Wind-Affected Maritime Operations

Trajectory optimization of an unmanned helicopter to a ship's deck in various wind conditions

Thesis report

by

D. Zilver

to obtain the degree of Master of Science
at the Delft University of Technology
to be defended publicly on September 24, 2024 at 15:45

Thesis committee:

Chair:	Ir. J.A. Melkert
Supervisors:	Dr. C. Varriale
	Dr. M.D. Pavel
	Prof. Dr. Ir. M. Voskuijl
Place:	Faculty of Aerospace Engineering, Delft
Project Duration:	October 2023 – July 2024
Student number:	5875242

Cover: AS-532U2 Cougar flying towards Ocean-Going Patrol Vessel Zr.Ms. Friesland during Joint Warrior 2019, Scotland, 25 March 2019. Photographer: Jasper Verolme. Copyright: Mediacentrum Defensie (MCD)

Faculty of Aerospace Engineering · Delft University of Technology

TU Delft

This page is intentionally left blank.

Preface

After my achievements at the Netherlands Defence Academy, I got the chance to broaden my horizon by participating in a Master's education. This thesis concludes that two-year journey at the Delft University of Technology, Faculty of Aerospace Engineering. My experience at TU Delft would not have been possible without the Royal Netherlands Navy, for which I am grateful. During my first year of courses, I acquired new knowledge in the Flight Performance and Propulsion track, such as aircraft design, aerodynamics, thermodynamics, structures, optimization, and control systems. The second year greatly consisted of the thesis project, in which I wanted to pursue my passion: helicopters. I figured "What is better to combine this passion with the maritime world?" and my thesis idea was born. I am grateful to have found three supervisors wanting to aid my passion and bring this project home. The final thesis project proved that you never stop learning, as I got to know things that were not taught before in courses, such as the method of trajectory optimization.

I would like to thank all my supervisors for their invaluable guidance during our project sessions. Without you, I would not have been able to carry out this project. My main supervisor, Dr. Varriale, always provided me with helpful feedback and asked the right questions. He also helped me out a lot whenever I was stuck with the optimization framework. I also want to thank Dr. Pavel for her help in modelling the helicopter and providing helicopter-related knowledge. Lastly, I would like to express my gratitude to Prof. Dr. Ir. Voskuijl. From teacher and supervisor during my BSc at the NLDA, to supervisor of my MSc thesis, you were always available and helped me whenever you could.

My family always believed in me and made it possible to pursue my passion. I am very grateful for this because I would not be where I am today without your love and support. I am also deeply grateful to my girlfriend, who happens to have a similar passion for aviation. In our countless conversations, you tried to help me in the best way possible, even if only by listening and nodding during my technical monologues when I needed to express my creativity.

My journey in Delft improved my academic skills and provided me with other perspectives to look at present-day problems. At the end of this chapter, a new one opens up with new adventures and goals to pursue. I am excited for what the future may bring!

D. Zilver
Delft, July 2024

This page is intentionally left blank.

Summary

A rotary-wing aircraft, or helicopter, is crucial for maritime operations due to its Vertical Take-Off and Landing (VTOL) capabilities, making it essential for small-deck Naval ships. Helicopters serve multiple roles, enhancing the Royal Netherlands Navy's (RNLN) missions. However, the rise of Unmanned Aerial Vehicles (UAVs) in the past decade has introduced a cheaper, expendable, and more efficient alternative for certain operations, as UAVs require no pilot and can operate continuously. UAVs are ideal for tasks related to improving situational awareness, thereby increasing mission effectiveness, reducing pilot risk, and lowering fuel consumption. The RNLN aims to utilize UAVs alongside crewed helicopters on new ships to maximize operational efficiency. Both helicopters and UAVs follow three mission phases: launch, mission, and recovery, with the recovery phase being the most challenging.

During the recovery phase, a crewed helicopter approaches the sailing vessel in a standardized way for which operational limits are established. These limits are essential for rough weather situations and are determined through many flight tests, which is a time-consuming, expensive and hazardous task. In addition, these operational limits only apply to a standardized approach manoeuvre. No approaches for UAVs are prescribed yet, making it difficult to determine such limits, but opens the possibility to standardize newly optimal UAV-ship approaches for which operational limits can be established. Moreover, the ship needs to manoeuvre to obtain optimal wind conditions for an approaching helicopter, which is not desired for UAVs. This means that UAVs should be able to approach and land on the ship in any wind condition.

This study investigated the effect of wind on optimized UAV-ship approaches, which can be used to aid and standardize maritime UAV-ship approaches. For this objective, a trajectory optimization framework was created that combined helicopter dynamics and performance, a ship, three wind models of increasing levels of accuracy and a solver to find optimal wind-affected approaches. Trajectories were optimized to be smooth and fast because this is most important for operational purposes. Experiments involved several wind directions, wind speeds and helicopter starting positions, affected by three wind models. This work shows that the created framework functions properly and can be used in a variety of situations.

The optimized trajectories were evaluated by the Longest Common SubSequence (LCSS) similarity measure to investigate the effect of both wind direction, speed and model fidelity. With an output between 0 and 1, the LCSS algorithm provided intuitive results and clear trends. A conclusion is that the helicopter wants to exploit the wind as much as possible. It diverts its path to acquire a higher ground speed at the start and a stronger headwind to decelerate at the end of the approach. When introducing a wind gradient, it was observed that the helicopter adjusted its vertical manoeuvre with the same objective. In some wind cases, constraint limits were reached or violated, marking preliminary operational limits.

Results were also interpreted with a different perspective to find the best starting positions for the helicopter to approach the vessel in a certain wind condition. These results showed a variety of optimal starting locations, based on the total objective function value, total energy consumption and by distance normalized quantities. Wind model fidelity did not influence this outcome significantly, but it showed that it is important to estimate performance parameters with higher-fidelity models for increased wind speeds. This could also be seen from the downdraft behind the hangar; while the optimized approaches did not deviate geometrically, performance indicators such as the power required were affected significantly.

Contents

$\tilde{\mu}$

Nomenclature

List of Abbreviations

ABL	Atmospheric Boundary Layer
CFD	Computational Fluid Dynamics
DARPA	Defence Advanced Research Projects Agency
DLR	German Aerospace Centre
DOF	Degree of freedom
EPSRC	Engineering and Physical Sciences Research Council
FDO	Flight Deck Officer
GPS	Global Positioning System
IGE	In Ground Effect
ISA	International Standard Atmosphere
JAPCC	Joint Air Power Competence Centre
LCSS	Longest Common SubSequence
LSED	Lock-Step Euclidean Distance
LSEDN	Lock-Step Euclidean Distance Normalized
MARIN	Maritime Research Institute Netherlands
MSA	Minimum Safe Altitude
NATO	North Atlantic Treaty Organization
NEREUS	Naval long Endurance Robothelicopter Equipped for Unmanned Surveillance
NLDA	Netherlands Defence Academy
NLP	Nonlinear Programming
NLR	Netherlands Aerospace Centre
OEI	One Engine Inoperative
OGE	Out of Ground Effect
PRR	Power Reserve Ratio
RNLN	Royal Netherlands Navy
SAR	Seach And Rescue
SHOL	Ship-Heliocopter Operating Limit
SPEEDOPS	ShiP-deck Environment and Efficient Drone Operations
SQP	Sequential Quadratic Programming
SUOL	Ship-UAV Operating Limit
TPP	Tip Path Plane
UAV	Unmanned Aerial Vehicle
VERTREP	Vertical Replenishment
VTOL	Vertical Take-Off and Landing
WO	Watch Officer
WOD	Wind Over Deck

List of Symbols

α_D	Disc angle of attack
β	Thrust vector conversion angle
χ	Heading angle
γ	Flight path angle
μ	Bank angle
Ω	Rotational speed
$\overline{U}_c$	Normalized velocity perpendicular to TPP
$\overline{U}_t$	Normalized velocity parallel to TPP
$\overline{v}_i$	Normalized induced velocity
ϕ	Mayer term / Roll angle
ψ	Yaw angle
ρ	Air density
σ	Solidity main rotor
θ	Pitch angle
θ_w	Angle between rotor wake and vertical reference line
$\tilde{\mu}$	Advance ratio

$\underline{u}$	Control vector
$\underline{x}$	State vector
$\underline{X}$,$\underline{Y}$,$\underline{Z}$	Axes directions
$\{\underline{E}\}$	Coordinate system
c	Mean chord
c_d	Mean profile drag coefficient
C_W	Weight coefficient
C_x,C_y,C_z,C_T	Thrust coefficients
$C_{P_{req}}$	Required power coefficient
D	Drag
f_e	Equivalent flat plate area
f_G	Ground effect factor
g	Gravitational acceleration ($9.80665\,\mathrm{m/s^2}$)
h	Altitude
H_R	Height from ground to main rotor hub
J	Objective function
K_{ind}	Induced power factor (1.15)
K_{t_f}	Weighting factor
L	Lagrange Term
M	Figure of Merit
m	Mass
N_b	Number of blades
P_a	Available power
P_{req}	Required power
R	Radius
T	Thrust
t	time
u,v,w	Forward, sideways and vertical velocities
U_∞	Free stream flow velocity
V	Total speed
v_{hov}	Induced velocity in hover
W	Weight
x,y,z	Forward, sideways and vertical positions

Subscripts

0	Initial
a	Air-Path axis system
b	Body Axis system
e	Moving Earth axis system
endur	Endurance
f	Final
fus	Fuselage
g	Ground axis system / ground
lat	Lateral
long	Longitudinal
max	Maximum
mr	Marin-Rotor axis system
NE	Never-Exceed
range	Range
ref	Reference
sea	Sealevel
TAS	True airspeed
w	Wind
xy	Horizontal

List of Figures

List of Tables

1

Introduction

1.1. Helicopters in maritime operations

A rotary-wing aircraft, commonly referred to as a helicopter, is extremely useful for maritime operations. A helicopter is essential for small-deck ships because of its Vertical Take-Off and Landing (VTOL) capabilities. Moreover, helicopters for maritime operations are built as flexible multi-role vehicles capable of performing a wide range of missions such as Search And Rescue (SAR), counter-drugs, humanitarian support, patrol and reconnaissance, anti-submarine and anti-surface warfare[B]. Therefore, the Royal Netherlands Navy (RNLN) utilizes the increased airpower for its missions.

In the last decade, Unmanned Aerial Vehicles (UAVs) have soared in the supply-and-demand chain and have been proven to be superior to manned helicopters for certain operations, especially since they are cheaper, expendable, require less fuel and can be deployed around the clock since no sleep-required flight crew is needed. UAVs are capable of taking over certain missions from crewed helicopters to increase mission effectiveness and reduce both safety risks for pilots and fuel consumption. For example, unmanned systems can execute situational awareness operations more economically and securely. In addition, UAVs are smaller and weigh less, which allows for more aerial vehicles to be taken onto the ship. In this way, more than one helicopter can be airborne at the same time to keep an eye on a larger area, which increases mission effectiveness even further. The Royal Netherlands Navy wishes to deploy UAVs from Navy ships because of these advantages[CD] [1]. The RNLN is even considering building new ships equipped with both crewed helicopters and UAV's[E].

A maritime helicopter or UAV mission plan is categorized into three main phases; launch, mission, and recovery, as depicted in Figure 1.1. Maritime aerial vehicles regularly operate in challenging environments, which increases the difficulty levels of all three phases. However, the most complex manoeuvre is the recovery operation, which involves retrieving the vehicle and having it land safely on the helicopter deck. The recovery can therefore be divided into two phases: the approach and landing. The approach starts at a certain distance from the ship where the helicopter flies to the ship in a specific manner and ends when the aircraft is in a steady hover above the landing deck. The subsequent landing phase involves the helicopter's descent until it is secured onto the deck. During these phases, the ship is in full service of the helicopter. This means that the vessel is obliged to alter its course and speed to obtain optimal wind conditions for the aircraft. Since both recovery phases have their difficulties, research has been conducted to assess the risks of shipboard helicopter operations and establish limits to ensure safe operations. These studies have provided greater insight into the interaction between helicopters and ships.

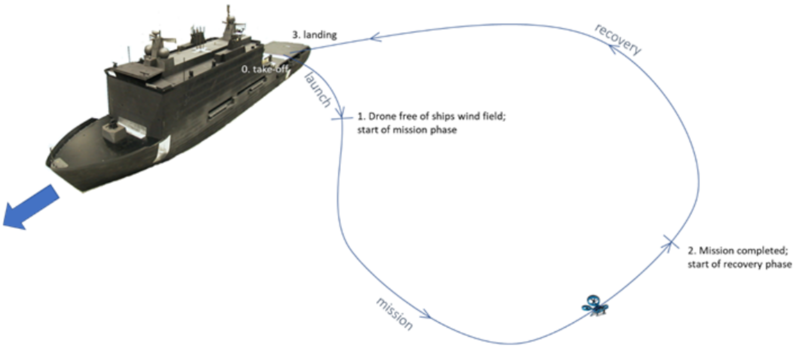

Figure 1.1: Mission cycle of a maritime helicopter or UAV. The three phases are launch, mission, and recovery [2]

1.2. Thesis contributions

To reduce the safety risks of recovery operations, operational flight envelopes are established for crewed helicopters by performing extensive flight tests in many weather conditions. These flight tests depend on many factors, including a specific standardized approach manoeuvre. However, approach trajectories for unmanned helicopters are not yet set in stone, complicating the determination of operational limits for UAVs, but opening the possibility to investigate optimal UAV manoeuvres for which operational limits can be determined.

Previous research has already revealed much insight into the reduction of (the risks of) flight tests for both manned and unmanned ship-helicopter operations and operational limits, the ship airwake and its effects on the helicopter, helicopter-ship landings and helicopter trajectory optimization. However, more knowledge can be acquired by studying optimal UAV-ship approaches. For crewed helicopters, prescribed ship approaches and their limitations are merged into standardized procedures to carry out the recovery as safely as possible. Nonetheless, UAV recoveries are still free to be determined, creating the possibility to assess the applicability of current helicopter approaches for UAV deployment and to optimize the recovery phase. Moreover, research into helicopter trajectory optimization has never involved a helicopter interacting with a ship, making this research contribute to the subject. Because ship-helicopter approaches are complicated even more due to the presence of wind, the study can also be broadened by studying optimal shipboard helicopter approaches in wind, for various wind models, directions, and severity levels.

Besides academic improvement, this research is also fundamental from a military standpoint, since optimized UAV-ship approaches will aid future maritime UAV operations for both the Navy and Coastguard. The standardized approaches for crewed helicopters require full cooperation from the ship, which is not desirable for unmanned systems. At present, UAVs need to be controlled by an operator on the vessel, but this becomes impossible when multiple drones need to be recovered at once. Creating the opportunity for the ship to not alter its course and speed for the UAV to land would be highly beneficial for future maritime operations. This involves the helicopter being able to approach the ship and land in all relative wind conditions possible, within a generalized flight envelope. Moreover, a different approach than the prescribed crewed helicopter approaches could enlarge the UAV's flight envelope and operational limits to more extreme weather conditions. This study investigates the opportunity to find optimal approach trajectories of UAV-ship approaches in windy environments. By studying the effect of wind on these optimal paths, new approach manoeuvres can be standardized for various wind severity levels. Therefore, it is beneficial to automate UAV-ship approaches and optimized approaches for a certain wind field can aid as guidelines.

1.3. Research Objectives

The main objective of this research is to assess the impact of both wind direction and speed on optimal UAV-ship approaches. By assessing the effect of wind on optimized approaches, new guidelines can be established without needing actual flight tests. For this objective, a trajectory optimization framework is created which can also be used to determine preliminary limits. This framework combines the interaction of UAV dynamics in a certain wind field with a sailing vessel. The optimal approaches of the studied UAV are assumed to also comply with comparable aircraft, allowing newly purchased UAVs to be deployed quickly. High wind severity levels for different relative wind angles constrain optimized trajectories because of certain UAV capabilities, such as the power required from the engine. In these cases, limits can be defined for a UAV because it flies an impractical approach to the ship while adhering to only performance constraints, not operational ones. Furthermore, the optimal approach manoeuvres from this study can aid as guidelines for new UAV approach manoeuvres, helping both the trajectory optimization research and future maritime UAV operations conducted by the RNLN or Coastguard. Another functionality of the framework is to do sensitivity analyses; testing the effect of another wind model on optimized trajectories. In this way, one may quickly assess whether a high-fidelity wind model is necessary for the preliminary flight plan design phase or if a rough estimation does well.

This study aims to answer the following research question:

How does wind affect an optimal approach trajectory of an unmanned helicopter to the landing deck of a sailing small-deck Naval vessel?

The question has been broken down into the following sub-questions:

- To what extent do wind-affected optimized trajectories resemble optimal paths without the presence of wind?
- How much does an optimal approach trajectory vary with changing wind direction and speed?
- What effect has a higher-fidelity wind model on optimized approaches?
- What is the influence of downdraft behind the ship's hangar on the optimal trajectory?
- What should be the optimal starting position of the helicopter to commence an approach for a given wind field?

1.4. Hypotheses

The main hypothesis is that the helicopter flies the path of minimum resistance to obtain the most optimal approach manoeuvre. For a uniform wind field, it is expected that the helicopter flies in a straight or constantly curved line as much as possible, which reduces power fluctuations and control effort. Next to this, it is expected that the helicopter changes its heading in order to use a tailwind to gain extra ground speed or avoid a headwind. In this case, constraints need to be imposed to prevent the helicopter from crashing into the ship. For a wind model including a wind gradient, it is expected that the optimal trajectory will be similar to the uniform wind case but deviate in vertical path, depending on which direction the wind change is in. The helicopter should fly its trajectory where it benefits most from the wind. That is, fly more in high tailwind and low headwind areas and vice versa for a lower flying time. For strong headwinds, the UAV could decide to fly as low as possible, since the wind velocity is lowest at low altitude. This means that extra bounds need to be set for a minimum safe altitude. It is also expected that optimized approaches in a downwash require more power due to the induced climb performance.

1.5. Project outcome

The outcome of this thesis is a generic model that needs information about the helicopter parameters and wind field and outputs an optimized trajectory, together with the helicopter's states, controls, and performance parameters. The model includes several wind types, such as no wind, uniform wind, boundary layer wind and a form of downdraft behind the ship's hangar. The program can be extended by including other types of wind models, which may be of higher fidelity. The model could also be broadened by a specific ship model that describes the ship's behaviour in a certain sea state, which could be complemented with the landing phase. Another extension of this project could be to incorporate other-than-conventional types of helicopters or to validate trajectories using higher fidelity models in combination with space mapping.

1.6. Thesis outline

This thesis report is outlined as follows. First, a literature review is presented which describes state-of-the-art helicopter procedures and highlights previous research into ship-helicopter interactions and the establishment of operational limits. Present-day projects are also highlighted as the focus is shifted from real flight tests to simulations, involving trajectory optimization of aerial vehicles. Chapter 4 details the created framework, including the assumptions made, helicopter and ship models and the optimal control problem. The experiments conducted to answer the research questions are outlined in Chapter 5. This chapter includes an explanation of the three wind models, a sensitivity analysis for the objective function's weighting factor and a procedure to post-process geometrical trajectories. After this, the key results are outlined and the main report finalises with the overall conclusions drawn and recommendations for future research. Every chapter ends with a summary and the main conclusions drawn from that chapter.

2

Shipboard Operations

This section zooms in on current crewed helicopter take-off and recovery procedures to better understand shipboard operations' difficulties. The information presented originates from official NATO and RNLN documents [3, 4, 5] as well as from open literature. Firstly, the state-of-the-art helicopter procedure cues that are used on naval vessels are described, including currently researched UAV procedure cues. Subsequently, a section is dedicated to current crewed helicopter take-off and landing procedures in which the most used approach trajectory is illustrated. Additionally, this section describes an experimental UAV recovery procedure. The chapter continues with ship-helicopter operation limitations, including helicopter performance, ship airwake characteristics and the Beaufort wind scale. The next chapter outlines previous and present research into maritime operation simulations and provides insight into both the model fidelity that should be used in this study and the definition of trajectory optimization with its accompanied challenges.

2.1. Helicopter procedure cues

Several markings, signals, and sensors have been installed on the helicopter deck to assist helicopter-ship approaches and landings. During the approach and landing phases, there is also extensive communication between the pilot, flight deck officer on the helicopter deck, and watch officer on the bridge in order to conduct the operation as safely and efficiently as possible. This subsection covers the most important markings and communication lines for crewed helicopters, as well as UAV procedure cues that could be implemented on the RNLN ships in the future.

2.1.1. Deck Markings

A Navy ship's helicopter deck contains multiple visual aids for approaching helicopters, as indicated in Figure 2.1. The glide path indicator (1) provides a glide path from 2 nmi behind the vessel, which is mostly used for straight-in emergency approaches. The horizon bar (2) consists of an array of lights above the hangar to create an artificial horizon for the pilot. Deck markings, such as the athwartship lineup line (3), touchdown circle (4) and landing lineup line (5) serve as a landing strip on the helicopter deck to assist a specific approach or take-off procedure. The Stop and Go lights (6) are two lights coloured red and green, respectively. These lights are controlled from the bridge to give visual approval for a helicopter take-off or landing. Floodlights (7&8) are used as work lighting and are switched off during helicopter operations. The vertical replenishment (VERTREP) lineup line is designed for in-air refuelling and hoisting operations.

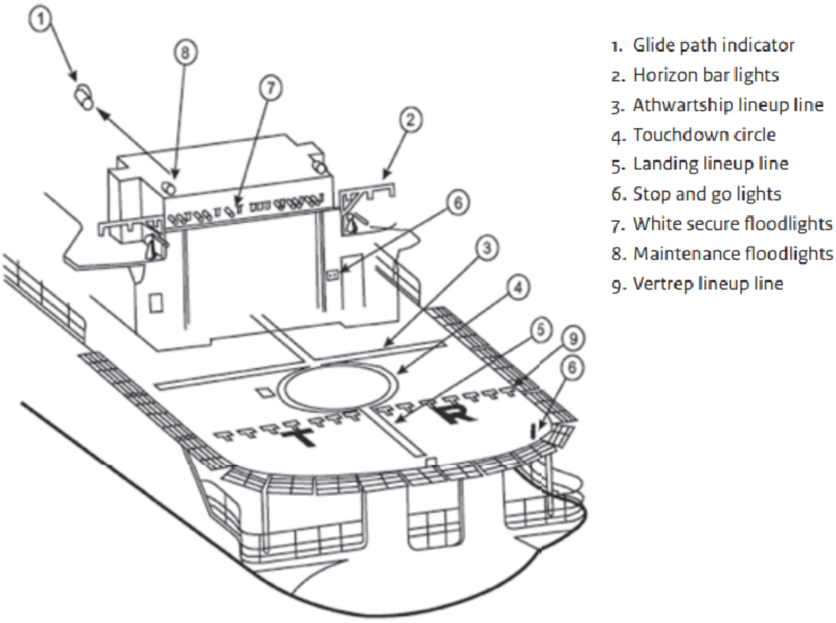

Figure 2.1: Helicopter aid deck markings on a RNLN vessel [4]

2.1.2. Flight Deck Officer

During helicopter operations, the pilot flying is not only supported by deck lights and markings, but also by the Flight Deck Officer (FDO). The FDO is placed under the bridge's command and is located on the helicopter deck, as depicted in Figure 2.2. The FDO is responsible for controlling the helicopter during the take-off, approach, and landing phases by giving hand gestures. In Figure 2.2 the Stop and Go lights are also visible and coloured green, meaning that the landing is authorized.

Figure 2.2: A Flight Deck Officer assists a helicopter landing[1]

---

[1] Photograph of a Flight Deck Officer aiding a NH-90 landing onto a Naval vessel, taken on 25 Feb 2020, Caribbean Sea. Photographer: D. Zilver

2.1.3. Bridge

The Watch Officer (WO) acts on behalf of the commanding officer and is in charge of the navigation and safety of the entire ship and crew. Therefore, the WO, assisted by command centre personnel, is also in charge of helicopter operations. The WO is responsible for considering operational limits and adjusting the ship's heading and speed in compliance with helicopter protocols. The bridge must approve every phase of helicopter take-off and recovery through communication and by the Stop and Go lights.

2.1.4. UAV procedure cues

Autonomous UAVs do not require visual aids to take off, approach or land. However, other indicators are needed to ensure safe UAV operations on maritime vessels. A UAV needs information about where to go, what path to take and where to land. This information can be obtained through various methods. One strategy for the approach phase is to install additional lights around the landing spot. With the help of a camera, it can be made possible for the UAV to navigate towards the lights [6]. Similarly, radio beacons on the landing deck could provide information regarding the location of the vessel [7]. Another method is to transmit the ship's position directly to the UAV and allow the aerial vehicle to navigate autonomously. The flight planning can be executed by crew members, providing coordinates and waypoints, or by the UAV itself, computing an optimized trajectory towards the landing deck.

Furthermore, there are several options for the landing phase. For instance, an ultrasonic altimeter on the UAV can be utilized to compute the altitude above the deck and to estimate the ship's movements due to the sea. Another possibility is to implement a landing controller [8], including a wave prediction algorithm, similar to that already installed in offshore gangway systems from Ampelmann[F]. This procedure requires a sensor or marking on the landing spot that can be recognized by the UAV. Other start-ups are also investigating the possibility of using QR codes on and around the ship to aid the landing phase of a UAV.

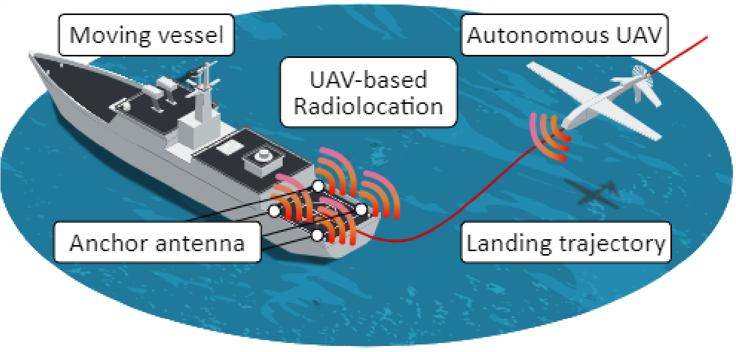

Figure 2.3: Autonomous UAV-ship approach using radio beacons [7]

2.2. Helicopter Take-off and Landing Procedures

In general, helicopter take-offs and landings are typically executed with a headwind, similar to fixed-wing aircraft. Nonetheless, this is practically impossible on Naval vessels due to the ship's superstructure and hangar situated on the helicopter deck, other obstacles around the ship and operational requirements. Additionally, there may be navigational hazards that need to be taken into account. Hence, different helicopter procedures for take-off and landing are employed aboard RNLN ships. NATO has multiple protocols for standard conditions and emergencies [3] and the RNLN has implemented four of them, among which one is an emergency procedure [4]. Table 2.1 displays all formulated NATO procedures and those that the RNLN has implemented, which are detailed in Appendix C. For all procedures, it is important to note that the ship positions itself optimally to receive the helicopter and maintains its speed and heading during the helicopter approach; the ship is in full service of the helicopter. After the helicopter crew has secured the helicopter either lashed on deck or stored in the hangar, the ship can resume its freedom of movement [5].

Table 2.1: NATO formulated and RNLN's implemented procedures

NATO Procedure	**RNLN**
Straight-in	✓(emergency)
Oblique (port to starboard or starboard to port)	✓
Lateral (port or starboard)	✓
45° (port or starboard)	✗
Athwartships (port to starboard or starboard to port)	✓

The port lateral procedure (Figure 2.4) is most frequently executed during current helicopter operations. This procedure involves the helicopter decelerating towards hover perpendicular to the landing spot. Subsequently, the helicopter performs a so-called 'sidestep manoeuvre' where it flies laterally relative to the ship and stops at hover above the desired landing position. Ultimately, the helicopter descends until touchdown during a quiescent wave period to minimize the landing impact. For this protocol, the ship positions itself such that the helicopter experiences a relative headwind from approximately 20° of port side. In this way, the helicopter is least affected by soiled air containing turbulence.

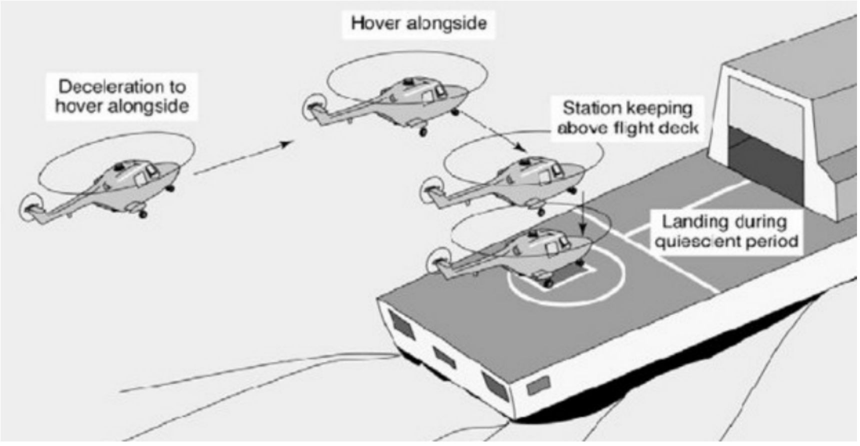

Figure 2.4: Lateral port landing manoeuvre [9]

In contrast to crewed helicopters, procedures for unmanned helicopter take-off and recoveries have not yet been established. Currently, an operator on the ship actively controls the UAV during the take-off and recovery phases, which are usually executed by a straight-in method. However, this approach is not practical for future operations where multiple UAVs or even swarms are active at once and a continuous flow of take-offs and landings is required. For such complete autonomous UAV operations, no explicit protocols have yet been formulated. Open literature solely suggests ways to communicate between the ship and UAV, or only describes methods applicable to the landing phase. An example of such a recovery phase is depicted in Figure 2.5, where several phases are highlighted including UAV tracking, high hover, low hover and final descent. Abujoub, McPhee, and Irani simulated UAV landings on a moving helicopter deck in sea states 2-6 (wave heights 0.1 m to 6 m) for different low hover heights [10]. Based on ship movement predictions, they assessed whether the UAV could safely land within roll and pitch limits. It was discovered that a low hover height of 2.5 m resulted in a higher number of failed landings compared to a low hover height of 5.0 m. The optimal low hover height has not yet been found.

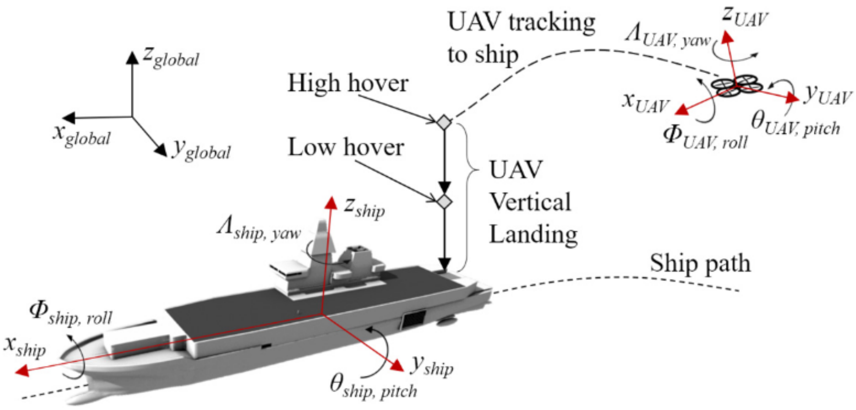

Figure 2.5: An example of a UAV recovery phase: tracking, high hover, low hover and descent [10]

2.3. Limitations to ship-helicopter operations

Flying a helicopter and successfully landing one on a moving vessel is a challenging task. Nevertheless, each platform has its own inherent limitations, and combining two results in even more complex boundaries. The main limitations of ship-helicopter operations can be divided into three factors, which are all dependent on atmospheric conditions such as air density and temperature [11]. The interaction and interdependence between these factors lead to the boundaries of the operational flight envelopes [12]. The three primary factors are:

- Helicopter flight characteristics
- Ship motion and marine effects
- Human factors

2.3.1. Helicopter flight characteristics

Helicopter flight characteristics and limitations depend on helicopter characteristics, design, flight condition and environmental parameters. Therefore, it is crucial to take these aspects into account during maritime operations. The five most important aspects influencing shipboard operations are the helicopter's weight, engine power and environmental effects, ground effect and control margins.

First of all, the weight of a helicopter is of great importance during maritime operations. A lighter vehicle is more susceptible to external disturbances such as airflows than heavier vehicles, which requires more control effort and can even lead to reaching limits under less severe weather conditions. This means that the operational flight envelope is reduced. On the other hand, a lighter helicopter is more agile and might be better capable of rejecting wind disturbances. Next to wind effects, a heavier aircraft requires more thrust due to its enhanced weight, resulting in more power required. This either demands a greater motor, more fuel consumption or a lower power surplus.

Furthermore, the engine power needed to operate a helicopter is a function of the total airspeed. This becomes particularly important when the relative wind speed is low, as it demands a significant amount of power. As can be seen from Figure 2.6, the power required increases with both low and high velocities, resulting in the infamous "bucket shape" of the power curve. The optimal range speed can be computed by determining the intersection point between the power curve and the line through the origin with the lowest tangent. Note that ground speeds may differ from this optimal airspeed due to wind effects. Next to this, the power required will increase if the helicopter is in the downdraft area on the leeward side of the ship, which will be elaborated on in the next section.

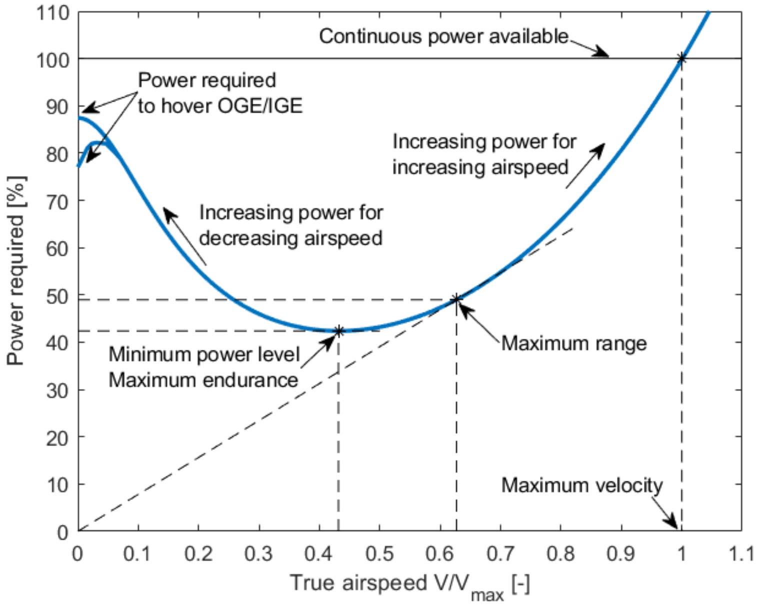

Figure 2.6: Power required and power available curves for a helicopter as a function of true airspeed (modified from [13, 14])

In addition, environmental effects play a role in the difference between the power available and the power required, which is also known as the power surplus. The power surplus is a measure of both the maximum rate of climb and helicopter responsiveness and is crucial in One-Engine-Inoperative (OEI) conditions. The power surplus decreases as the power required increases and the power available decreases due to reduced air density and/or increased ambient temperature, making it harder to operate in "hot and high" conditions [15].

Another aspect is the ground effect, which causes an increase in lift and thus a decrease in power required when a helicopter flies above ground or a stable ship deck, thereby alleviating helicopter operations. When flying near a flat surface, the helicopter's main rotor induced flow interferes with the ground, reducing the induced airflow velocity and tip vortices. The interference causes the airflow direction to change, as can be seen from 2.7. Near the ground, the downward airflow meets the ground before it is fully developed and has to divert. This leads to slower induced airflow, which results in less induced drag, more lift and thus overall better performance. By altering the downward flow, the flow upstream is also impacted. This tends to restrict rotor tip vortex generation, which also leads to increased performance. Despite this, ground effect power reductions are less significant with high airspeeds and are diminished when the helicopter passes over the deck edge. This is because the ground effect is more pronounced above a hard surface or ground than above the sea[GH].

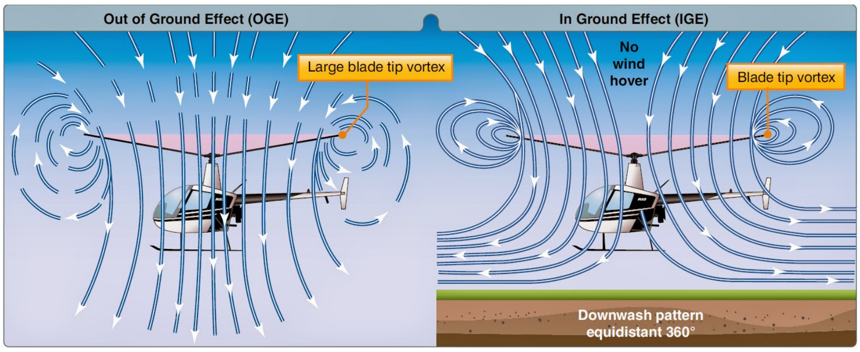

Figure 2.7: Airflow patterns of a helicopter Out of Ground Effect (OGE) and In Ground Effect (IGE)[I]

Moreover, control limits play a role during helicopter operations. Collective inputs drive the helicopter's vertical movement, making use of the power surplus. Hence, when the maximum collective input is required, the power surplus becomes zero. Pedals are important to compensate for torque effects generated by the main rotor. Due to the main rotor's direction of rotation, there is a difference between right and left pedal margins and thus the rate of heading change between left and right. The cyclic manages the helicopter's attitude and horizontal velocity. Lateral cyclic is margined due to bank angle limits, which impact, among other things, loads on the airframe and controllability. Aft cyclic margins are particularly important during tailwind conditions. In this scenario, the helicopter may be flying backwards relative to the air, which may lead to high nose-up attitudes, reducing visual reference and tail clearance with the flight deck.

2.3.2. Ship motion and marine effects

Apart from limitations posed by helicopter characteristics, an additional vessel complicates maritime operations even more. As opposed to land-based helicopter operations, the helicopter needs to land on a moving platform, which increases the difficulty tremendously. Not only does the ship sail at a certain speed, but the landing deck also pitches, rolls, yaws and heaves, which becomes more intense with increasing sea state. This may cause safety hazards during landings, especially when the deck moves violently in bad weather conditions. Moreover, the moving flight deck has limited dimensions, which requires precise helicopter control during the landing phase. Additionally, sea sprays caused by the helicopter's induced velocity and ship bow deteriorate rust formation on the helicopter's fuselage and visual reference with the flight deck. In low wind speed conditions, sea sprays result from the helicopter's main rotor downwash, whereas in high wind speed conditions, sea sprays originate at the ship's bow in high sea states [12].

Figure 2.8: Sea spray originating from the main rotor downwash [12]

The marine environment surrounding a ship poses major limitations to naval operations, particularly during helicopter-shipboard take-off and landings, performed in winds from any direction relative to the helicopter. It is therefore necessary to understand the airflow characteristics in the ship's vicinity, also known as the ship's airwake. These characteristics vary not only with the ship's superstructure, but also with the helideck's dimensions and the possibility to have more than one landing position, as depicted in Figure 2.9. For a given vessel, the ship's airwake depends on the vector sum of the true wind and ship velocity, known as the relative wind or Wind Over Deck (WOD) where the direction ranges from 0° to 180° on both ship sides; port (red) and starboard (green). Relative winds can be manipulated by the ship's velocity and heading up to a certain degree as long as the area of operations permits. For instance, it may be impossible to obtain a satisfactory relative wind speed if the absolute wind is too strong. Besides, heading adjustments to achieve favourable relative wind conditions may exceed the pitch and roll limits due to the sea state or may steer the ship towards land.

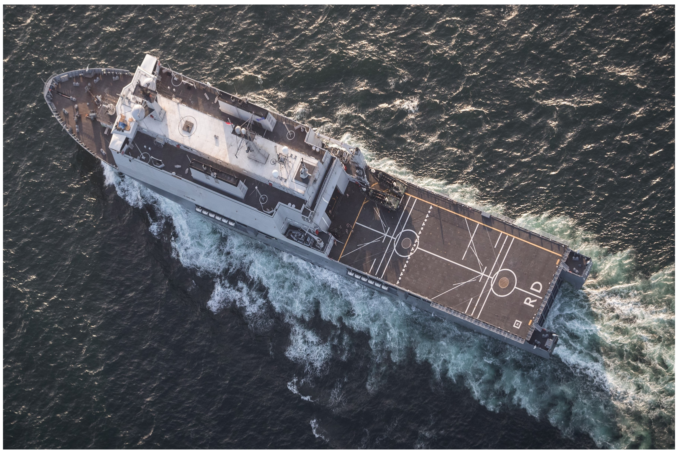

Figure 2.9: An example of two helicopter landing places on board of Zr.Ms. Rotterdam (RNLN) [2]

---

[2] Photographer: Sjoerd Hilckmann (Operation Atalanta; Coast of Somalia, Indian Ocean, 29 September 2017). Copyright: Mediacentrum Defensie (MCD)

Helicopters are required to navigate through the ship's airwake chaotic flow regime during the approach and landing. This region is characterized by high turbulence, shear layers and recirculation zones [16]. The ship's superstructure greatly influences the airwake, which causes a recirculation zone behind the hanger, also known as the "bubble effect" [11]. The effects of airflow and turbulence around the ship's superstructure are influenced by the dimensions of the ship and the relative wind vector. Moreover, obstacles such as cranes introduce more turbulence, negatively impacting the airwake. The ship's airwake characteristics can be divided into four groups based on the relative wind directions [11]:

- Headwinds ± (0° to 30°)
- Quartering winds ± (30° to 60°)
- Beam winds ± (60° to 120°)
- Aft quartering winds and tailwinds ± (120° to 180°)

Headwinds ± (0° to 30°)

With headwinds, the air over the flight deck is strongly influenced by the dimensions of the ship's superstructure and hangar, as illustrated in Figure 2.10. The hangar produces a closed wake bubble over the flight deck in which turbulent airflow with low speeds or even a reversed flow region may be present. An increase in hangar height or relative wind speed enhances the bubble effect, resulting in more power required from the helicopter. When entering this bubble, the helicopter may lose height and move forward due to sudden loss of wind speed combined with reversed flow [12]. Flight operations conducted from the aft landing spot, situated furthest away from the hanger, are usually less hindered. Thus, flight operations from the aft spot can be conducted at higher wind speeds than the forward spot.

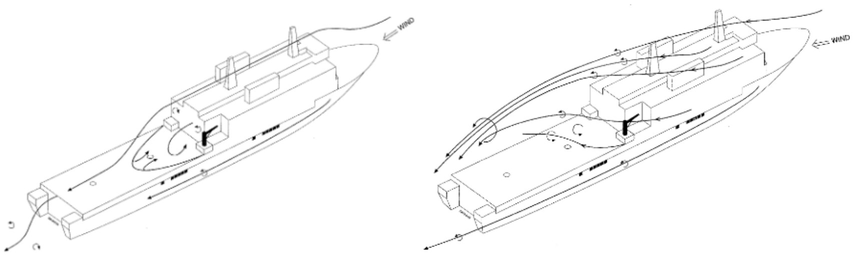

Figure 2.10: Main vortices for headwinds (WOD = 0° and WOD = 30°) [17]

Quartering winds ± (30° to 60°)

For winds in this sector, the ship's superstructure and sharp hangar edges generate a dominant vortex which rolls over the flight deck, as demonstrated in Figure 2.11. Again, flight operations to the aft landing spot are generally less hindered by the vortices and could therefore be possible at higher wind speeds than the forward spot [12]. In this WOD condition, a significant down flow, also referred to as "downdraft", can be observed at the leeward side of the vessel, which may exceed $400\,\mathrm{ft/min}$ ($\approx 2\,\mathrm{m/s}$) depending on the superstructure's height and type [18].

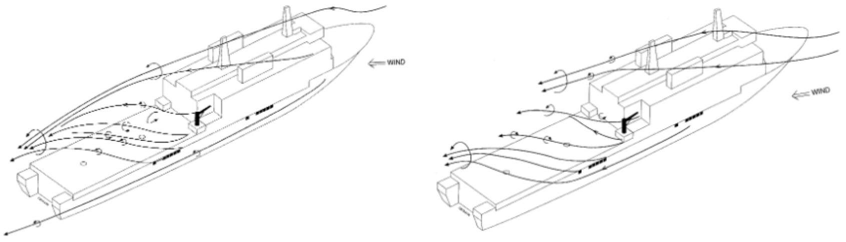

Figure 2.11: Main vortices for quartering winds (WOD = 45° and WOD = 60°) [17]

Beam winds ± (60° to 120°)

From beam winds and further, the ship's superstructure and hanger dimensions do not affect the flow patterns on the helicopter deck as much as described above. However, beam winds could result in relatively strong up-flow and down-flow on respectively the windward and leeward sides close to the ship, as illustrated in Figure 2.12. The sharp flight deck edges can create a vortex that could stretch the entire length of the deck. This vortex is noticeable in the helicopter when approaching the ship, causing large torque fluctuations [12].

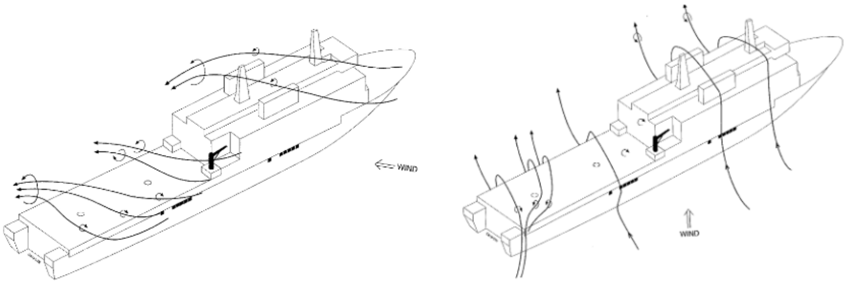

Figure 2.12: Main vortices for beam winds (WOD = 75° and WOD = 120°) [17]

Aft quartering winds and tailwinds ± (120° to 180°)

Aft quartering winds and tailwinds can create a relatively strong vortex from the rear of the ship, as shown in Figure 2.13. This vortex increases in strength with increasing height of the flight deck above sea level and relative wind speed. In most cases, the front landing spot is less affected by the vortex, allowing for a slightly larger flight envelope than the aft landing spot. However, this effect is less experienced due to operational helicopter flight envelopes for tailwinds, which usually include lower wind speeds [12].

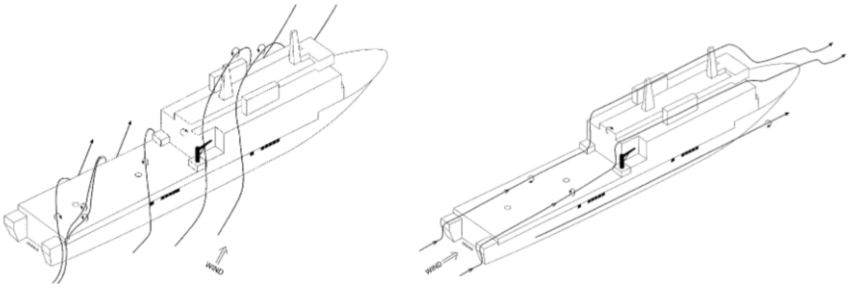

Figure 2.13: Main vortices for aft quartering winds and tailwinds (WOD = 150° and WOD = 180°) [17]

Complexity ship airwake

The ship's airwake is complex, chaotic, and difficult to predict using Computational Fluid Dynamics (CFD) simulations. For example, the complexity of the ship airwake is illustrated in Figure 2.14. In this figure, results from CFD simulations show the streamlines of instantaneous velocity magnitudes around the ship for a headwind. The airflow separates from the sharp edges of the superstructure and flight deck, leading to typical bluff-body wakes such as shear layers and large-scale vortices [19]. These flow structures break down into smaller-scale flow structures due to smaller ship features such as masts, weapon systems and radars. The result is a highly unsteady airflow with complex aerodynamic conditions around the flight deck.

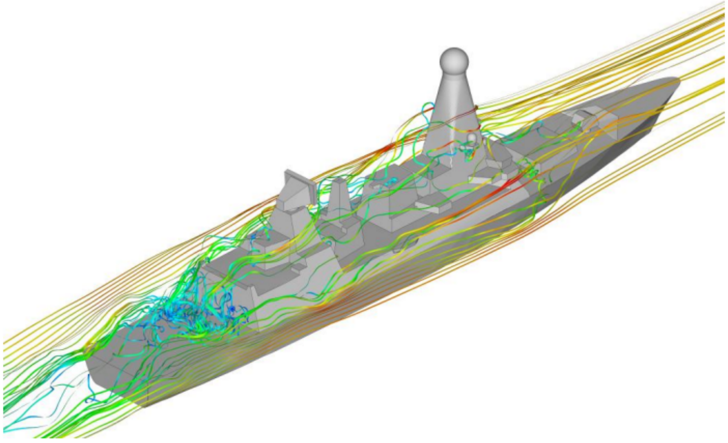

Figure 2.14: Streamlines of instantaneous velocity magnitudes over a Royal Navy Type 45 Destroyer in a headwind derived from CFD simulations [19]

Extensive wind tunnel tests and CFD simulations have been done in this field to better understand and predict the ship's airwake under certain WOD angles and velocities. This research shows that turbulence levels associated with the ship's airwake increase in intensity with increasing relative wind speed and vice versa [12]. Moreover, the amount of turbulence in the ship's airwake is related to the relative wind direction because of obstacles on deck. An example of the interaction between turbulence intensity and relative winds is shown in Figure 2.15. Areas containing increased turbulence levels may cause helicopter torque spikes, increased yaw instability and substantial pitch and roll motions for the helicopter. This is accompanied by a higher workload for the pilot, which results in more control actions.

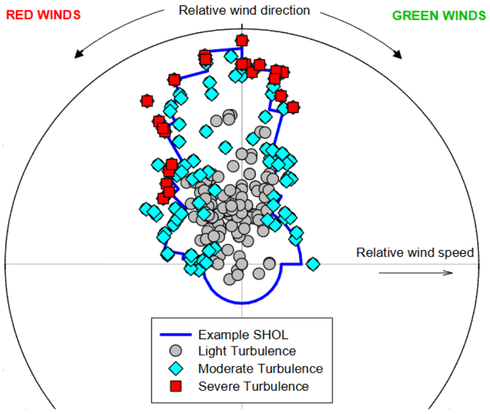

Figure 2.15: Example turbulence levels due to ship airwake [12]

Beaufort Wind Scale

True winds are categorized on the Beaufort Wind Scale, which was created in 1805 by Britain's Admiral Sir Francis Beaufort (1774-1857)[J]. The scale relates true wind speed to observed conditions on land or at sea and ranges from 0 (no wind) to 12 (approaching hurricane phenomena). For wind speeds that exceed this scale's highest rating, the Saffir-Simpson Hurricane Scale was defined to capture phenomena that occur in those conditions[K]. Appendix E provides the Beaufort Wind Scale and its specifications for each wind speed.

2.3.3. Human factors

Both helicopter and ship limitations contribute to the pilot's workload and become more prominent during bad weather conditions. When absolute wind speeds are high, relative wind speeds on the flight deck also increase, leading to greater turbulence levels near the landing area. The ship's motion also becomes more violent with increasing sea state, enhancing the pilot's control effort and thus workload. Furthermore, bad weather increases the chances of sea sprays, blocking visual reference with the FDO and flight deck. Additionally, sea sprays and violent deck movements could limit the ability of the FDO and helicopter crew to secure the helicopter onto the deck due to higher risks of falling overboard.

2.3.4. Limitations autonomous UAV

The limitations that apply to manned helicopters also largely apply to autonomous UAVs. Autonomous helicopters also suffer from performance losses and higher control efforts in bad weather situations. Due to being smaller and lighter, UAVs are more susceptible to wind disturbances, but also more agile. Although autonomous UAVs are less hindered by losing visual reference to the flight deck, other issues such as UAV hijacking, GPS spoofing/jamming, encryption of communication lines and the need for additional deck sensors arise [20, 21].

The Joint Air Power Competence Centre (JAPCC) presented a journal in 2018 that dedicated several chapters to both future helicopter operations and UAVs to conduct anti-submarine warfare, missile defence and UAV miniaturization [22]. In light of this, NATO extended research groups to explore unmanned operations. In 2023, a NATO study group partnered with commercial helicopter and UAV companies to sift through the challenges of using UAVs for maritime operations [23]. Several aspects are mentioned in this report, such as communication, installations, command and control, but also weather conditions and recovery operations. They stress the creation of models and the use of simulations to assess the capabilities and constraints of UAVs for mission management. In addition, the report also acknowledges that UAVs are a relatively new field that differs from crewed helicopters, therefore indicating other procedures could be followed. A review article by Mohsan et al. studied the applications, challenges and future trends of UAVs in which they clearly describe the state of the art of UAV technology [24].

2.4. Operational Limits

As discussed in the previous sections, shipboard-helicopter operations involve many risks, which is why operational limits have been established. These limits are known as Ship-Helicopter Operating Limits (SHOLs) for manned aircraft, or Ship-UAV Operating Limits (SUOLs) for unmanned aircraft; an example of a typical SHOL/SUOL is illustrated in Figure 2.16. In this figure, the “RED” and “GREEN” halves of the SHOL depict relative wind directions from port and starboard side, respectively, with “0” indicating the ship’s head. The radial distance displays the relative wind speed, here ranging from 0 kts to 50 kts. The black bold line indicates the boundary of the operational envelope. In a typical SHOL, both the approach and landing phases are combined. The approach phase is constrained by relative wind direction and speed, as indicated by the black bold line, whereas the landing phase is mostly bounded by deck motions such as pitch, roll, and heave. Operating outside these boundaries is generally not permitted, except for extreme circumstances [25].

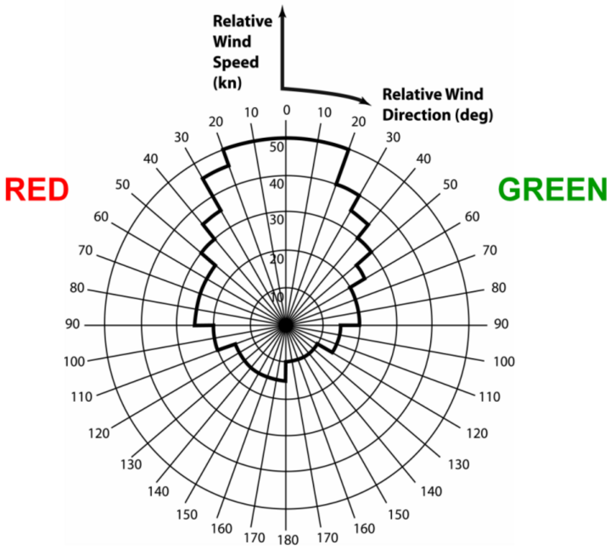

Figure 2.16: An example of a SHOL/SUOL [19]

Determining these boundaries is a time-consuming and expensive task [26]. A SHOL is established through multiple weeks of intensive flight trials for a single ship-helicopter pair and is solely valid for this particular combination and procedure executed. A SHOL is determined by combining limits encountered from relative wind directions and velocities, deck motions and helicopter controls [27]. SHOL testing proceeds by increasing the severity of the test conditions until one of the limits is reached; the first limit reached defines the capability limit. Flight tests with crewed helicopters are commonly performed with only a handful of standardized approach manoeuvres, as discussed in Section 2.2, which is why SHOLs do not apply to every situation. There are different SHOLs for different approach manoeuvres and even for various deck operations, which also differ from day to night [5].

This page is intentionally left blank.

3

From flight tests to simulations

Flight trials are labour and resource-intensive and have high safety concerns. In addition, despite several weeks of intensive testing, not all weather conditions can be evaluated, resulting in incomplete SHOLs. To overcome these issues, simulation models have been developed to establish operational limits, leaving only a few validation flights to test pilots. Reducing flight trials to a handful of validation flights via simulations reduces costs, minimises risks and vehicle failures and maximizes its lifespan. Furthermore, simulation models enable vehicles to be assessed in all weather situations and to be deployed quickly after purchase. Therefore, this chapter dives into past and present developments of simulation environments for helicopter-ship interaction modelling. Because this study examines the effects of wind on optimized trajectories, this chapter also elaborates on which model fidelity to use and how trajectory optimization works.

3.1. Helicopter recovery operations

Figure 3.1 illustrates a rough weather scenario in which a helicopter still needs to be able to take off and land safely to accomplish its mission. Since flight trials in these conditions may be dangerous, research has been conducted to create simulation environments in which operational limits of helicopters can be determined [28, 29, 30, 31]. This research began in the 90's and was extended from 2000 by the University of Liverpool, which created helicopter simulators that utilize FLIGHTLAB or Matlab (Simulink) models to determine SHOLs [30]. Meanwhile, other studies were developing SholSim, an offline simulation routine to estimate SHOLs based on pilot model predictions [32]. These studies have led to a better understanding of ship-helicopter interactions.

Figure 3.1: Helicopter operations on board of a ship in rough weather [33]

The advent of UAVs and their capabilities has opened new research fields, including ship-UAV recovery operations [34, 35, 36, 37]. The Netherlands Defence Academy (NLDA) collaborated with the Netherlands Aerospace Centre (NLR) and Maritime Research Institute Netherlands (MARIN) to launch the NOTUS project[L]. This project aimed to create a simulation environment where UAVs can land autonomously to determine operational limits in adverse weather situations. One of the outcomes is a landing strategy algorithm that incorporates predicted future deck motions, coupled with a flight controller capable of landing the studied UAV [8].

Recently the NLDA, NLR and German Aerospace Center (DLR) launched the SpeedOps (ShiP-deck Environment and Efficient Drone Operations) project, which aims to automate launch and recovery operations of drones and evaluate wind climates around the landing deck [2]. Next to this, another project called NEREUS (Naval long Endurance Robothelicopter Equipped for Unmanned Surveillance), initiated in 2018 by Delft Dynamics, Damen Navel Shipyards and NLR, researched innovative technology for operating maritime unmanned helicopter operations from Navy or Coastguard ships in a safe, efficient and cost-effective manner[M]. Although these are just a few examples of Dutch projects, many more international projects are going on, such as TERN (Tactically Exploited Reconnaissance Node) by the Defence Advanced Research Projects Agency (DARPA)[N], a research project done by the UK's Loughborough University and funded by the Engineering and Physical Sciences Research Council (EPSRC)[O], PROTEUS by the Royal Navy[P] and other international and commercial projects[QRST].

3.2. Helicopter operations in the ship airwake

Wind greatly affects ship-helicopter operations partly due to its chaotic nature. Research has been conducted to evaluate wind effects on shipboard-helicopter operations and to develop CFD models that accurately describe turbulence, such as using detached-eddy simulations [38]. Some studies have used wind tunnel tests to investigate the effects of helicopters on ships [39], while others have examined flow properties obtained from CFD simulations together with actual flight tests [19]. The University of Liverpool has created models for the ship, helicopter, and wind fields to develop a flight simulator capable of estimating operational limits [40].

The effects of both static and dynamic ground effects on helicopter approach and landing in wind were investigated by Sharma et al. [41]. They discovered that rotor power consumption could decrease up to 10%, which was validated by experiments on a stationary deck [42]. In addition, the dynamic ground effect due to the heaving motion of the ship could provide an additional 7.5%. They also investigated the effects on the helicopter when tracking a pre-determined path for landing on a ship's deck in wind using a specifically designed optimal controller [41]. This study concluded that relative winds differ from starboard and port side due to the asymmetry of the ship, which requires consideration of winds from all directions in establishing SHOLs.

Another conclusion was that relative winds also affect other helicopter components, leading to higher control efforts and a sharp reduction in power required due to the ground effect. Lee et al. took this research a step further and studied the helicopter launch and recovery in air wakes with a disturbance rejection controller that resembled a human pilot to assess the effects on pilot workload due to the unsteadiness of the ship airwake [43]. Another study by Siccama analysed the response of a helicopter in 3D turbulent flow around high-rise buildings [44]. This study included 3D CFD simulations for turbulent flow, as well as a controlled helicopter flying near buildings in this turbulent flow field.

3.3. Simulation model fidelity

A simulation tool is only able to estimate real-world effects. The fidelity of the model underlying the simulation tool refers to how closely a model represents reality and involves the level of detail included in the model[U]. Simulation models can be divided into two main categories: high and low-fidelity models. Generally speaking, the higher the model fidelity, the more equations, subroutines, data, and parameters are involved and the higher the computational effort. This also means that the outcome is more accurate and closer to reality. Optimal helicopter approaches are examined in this study, which is why one should know what model fidelity should be utilized.

An example of a high-fidelity model related to the subject is a six Degrees of Freedom (6DOF) helicopter model, in which translational and rotational movements in three directions can be simulated. High-fidelity models may appear realistic and provide greater insight into the overall characteristics of the studied model than low-fidelity models. However, high-fidelity models require more time to create, debug and operate and are more computationally expensive than low-fidelity models. Furthermore, high-fidelity models are more complex and require more inputs, which could negatively impact the outcome if uncertain. Additionally, control actions and axes outputs might be coupled, making it harder to grasp the fundamentals in early-stage studies.

On the other hand, a low-fidelity model is a simplified model which, for instance, represents a 3DOF helicopter model that only simulates three translational movements along three uncoupled axes. This kind of model is easier and less expensive to construct, implement and operate than a high-fidelity model. However, it is less realistic and might oversimplify complex issues. A low-fidelity model is mostly used to learn the problem's fundamentals and to assess high-level trends between inputs and outputs. Another functionality of a low-fidelity model is that control laws can be tuned more easily than on a high-fidelity model. Users need to know the key assumptions on which the model has been built to assess whether the model works adequately enough for their problem.

Both high and low-fidelity models have their advantages and disadvantages and are broadly used in many fields of research, such as clinical nursing [45], biomechanics [46] and optimization [47, 48]. In trajectory optimization problems, low-fidelity models are commonly used for their reduced complexity and computational costs. The level of model function evaluations and iterations is high, resulting in a high computational duration if done with a high-fidelity model. Moreover, a high-fidelity model could be too complex for the optimizer if constraints are also added. In this case, a low-fidelity model has a higher chance of convergence while keeping the computational effort relatively low. The fundamentals of the optimized results can be assessed better and validated with higher fidelity models to assess more real-world mechanics. Another option is to use space mapping; optimizing with a low-fidelity model and validating in the loop with a high-fidelity model [49]. A low-fidelity 3DOF helicopter model was selected for this study in combination with a trajectory optimization framework.

3.4. Trajectory optimization of aerial vehicles

The goal of a dynamic optimization problem is to find a control history that satisfies control and state constraints over the entire time interval $[t_0, t_f]$ while minimizing an objective function [50]. A trajectory that satisfies these criteria is called an *admissible trajectory* and the control history that makes this possible is called an *admissible control*. Such a dynamic system is described by a set of differential equations, also known as *hodograph constraints*, of the form $\dot{\underline{x}} = \underline{f}[\underline{x}(t), \underline{u}(t), t]$, where $\underline{x}$, $\underline{u}$ and t are the system's states, controls and time, respectively. Without these constraints, it is possible to obtain a mathematically correct solution, but this will be physically unrealizable and thereby impractical for real-world systems [51]. The system state bounds and equality/inequality constraints are similar to design optimization problems. A typical optimal control objective function is defined as the following Bolza problem, which consists of an end-cost Mayer (ϕ) term and a time-dependent Lagrange (L) part:

$$J = \phi\left[\underline{x}(t_f), t_f\right] + \int_{t_0}^{t_f} L\left[\underline{x}(t), \underline{u}(t), t\right] dt \tag{3.1}$$

Where the final time t_f can be fixed or free. Such an expression is called a *functional* which implies that J is not just a function of the system state and control variables, but also takes into account their integrated form, which implies that it is a function of a function [50]. Optimal control problems can be categorized in two forms, namely *open-loop* and *closed-loop* (or feedback) form; which is indicated in Figure 3.2. In trajectory optimization, a solver creates an optimal control law: a sequence of controls that minimize the objective while adhering to all constraints. The open-loop form is only optimal for a specific initial state, whereas the closed-loop or feedback control law is valid for any initial state. Since closed-loop control solutions require more attention and are not required in offline simulation studies, open-loop problems are more frequently formulated.

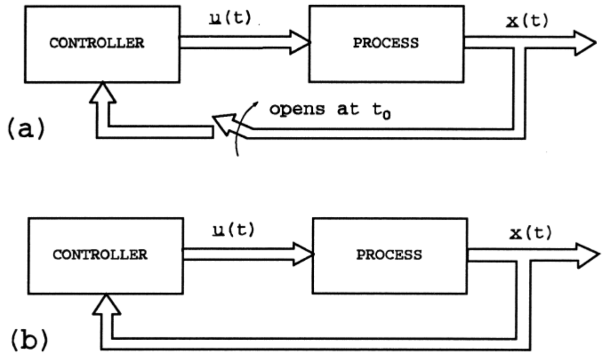

Figure 3.2: (a) Open-loop optimal control, (b) Closed-loop optimal control [50]

Solving an optimal control problem is not straightforward and requires multiple steps, as depicted in Figure 3.3. First, the optimization problem needs to be formulated, involving an objective function, equality/inequality constraints and system bounds, which are all similar to design optimization problems. However, it is also necessary to define boundary constraints and differential equations that describe the vehicle's motion as a function of time. Subsequently, the optimal control problem should be converted to a Nonlinear Programming (NLP) problem, which a NLP technique can solve. This process, also known as 'transcription', can be carried out through a variety of methods [52]. Section 4.4 describes the transcription method used in this study. Furthermore, an initial guess for all states and controls is necessary, at least for the first and final time steps, but ideally for all mesh points. An NLP optimizer solves the NLP problem and outputs the optimal trajectory. Some trajectory optimization toolboxes offer mesh refinement options if certain error thresholds are violated. In that case, the old solution is fed back for the next iteration until the termination criteria are met.

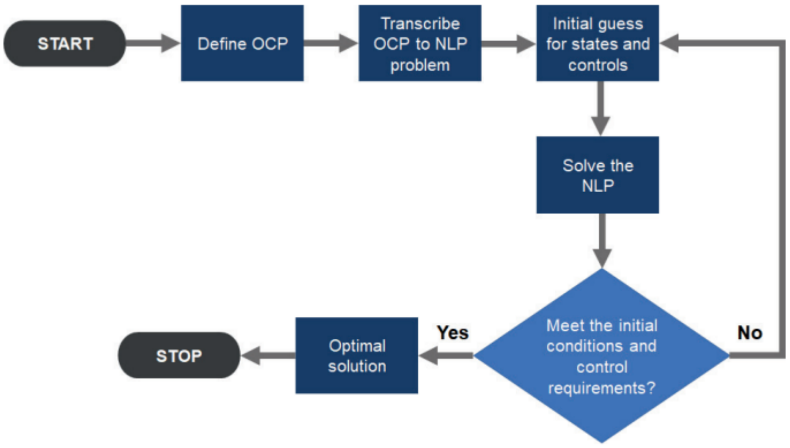

Figure 3.3: Flowchart of an optimal control problem [53]

The field of trajectory optimization for aerial vehicles has seen significant research in the last few decades, covering fixed-wing aircraft, helicopters and quad-copters. Studies on quadcopters mainly focused on trajectory optimization for obstacle avoidance [54]. Once a trajectory was computed, wind disturbances enter the playing field to build a disturbance rejection path tracking controller. Studies for fixed-wing aircraft do not only involve optimizing flight phases, but also developing optimal control methods. For example, decoupling the complex optimization problem into a path and velocity problem turned out to be more computationally effective while reducing the overall problem [55].

In his dissertation, Hartjes studied the trajectory optimization of a helicopter to reduce noise and emissions using a full-scale 6DOF helicopter model and stationary horizontal winds [56]. Due to the computational expense of such a detailed model, many other studies used 3DOF point-mass models of a helicopter for their optimal control problems. Some studies focused on one-engine-inoperative (EOI) conditions to optimize vertical take-off and landing [57] or balanced field lengths [58], using low-fidelity helicopter models. In addition, these studies used trajectories consisting of multiple phases, each phase could include different optimization constraints, variable bounds or even equations of motion. Furthermore, MSc students at Delft University of Technology optimized trajectories for helicopter arrivals and departures to reduce noise and emission abatement using a 3DOF point-mass helicopter model [59, 60].

Tsuchiya et al. attempted to obtain optimal landing approaches for helicopters to reduce ground noise impact but did not succeed due to unforeseen disturbances [61]. These external disturbances were analysed and algorithms for practical real-time optimization were improved, resulting in a new method that divided the path-to-go into multiple non-equidistant stages that can be optimized in real-time [62]. This numerical study concluded that the optimized trajectories differ from conventional landing approaches and was expanded further with real flight tests to improve real-time trajectory optimization.

3.5. Summary

Previous research has already revealed much insight into the reduction of (the risks of) flight tests for both manned and unmanned ship-helicopter operations and operational limits, the ship airwake and its effects on the helicopter, helicopter-ship landings and helicopter trajectory optimization. These studies were conducted to assess operational limits with procedural manoeuvres and to automate ship landings by adhering to certain landing performance criteria. However, no former study optimized trajectories for helicopters affected by wind; instead, it used wind as a mere disturbance that had to be rejected. In addition, no records were found on the trajectory optimization of an aircraft relative to a ship. This research gap is filled in this study.

Unlike crewed helicopters, approach procedures for UAVs are not yet set in stone, making it possible to find optimal trajectories. Suboptimal standardized approaches require full cooperation of the ship, which is not desirable for unmanned systems. Future maritime operations would benefit from creating the opportunity that the vessel does not have to alter its course and speed for the UAV to approach and land. This involves the helicopter being able to fly in all relative wind conditions possible, within a generalized SUOL. Moreover, the possibility of approaching the ship along unprescribed trajectories could enlarge the flight envelope to more extreme weather conditions. For this objective, a trajectory optimization framework was created and exposed to several experiments and wind models, as described in the following chapters. By studying the effect of wind on these optimal paths, new approach manoeuvres can be standardized for various wind severity levels and UAVs can be deployed quickly after purchase to aid in maritime operations.

4

Simulation model

This chapter elaborates on the experimental framework used. This study's research questions will be answered through an optimization framework based on simulations. This chapter commences with a general overview of the entire framework. After that, the main assumptions behind the several models are described. Subsequently, the helicopter model is described which includes dynamics, performance, and the selected UAV. Afterwards, the ship model and its parameters are covered, followed by the definition of the optimal control problem and the process to solve it. This chapter concludes with a summary of the trajectory optimization problem and a detailed overview of the entire framework.

Figure 4.1 presents a high-level overview of the created optimization framework. The framework is composed of four blocks consisting of several models. The first model simulates the helicopter dynamics and performance parameters. The former is based on equations of motion of a point-mass model, while the latter involves the induced velocity through the main rotor, ground effect and required engine power. Next to this, the ship's dynamics are modelled in a separate block. Although the vessel sails at a constant velocity and heading in this study, the ship model is added for completeness. The third block consists of three wind models with increasing levels of accuracy. The helicopter should fly in these wind models while the optimizer finds the best approach manoeuvre to the ship's landing deck. This is encompassed in the trajectory optimization block.

The optimization problem involves several aspects. In trajectory optimization, the objective to be minimized is known as a Bolza problem. Both during the approach and at the initial and final time steps, constraints are also imposed on the helicopter's behaviour to restrict the optimizer and to find a feasible solution. Lastly, helicopter positions, velocities, and controls should comply with certain bounds, both during the manoeuvre and at the initial and final time steps. This problem definition is the first step since the trajectory algorithm also includes an optimal control transcription method and solver.

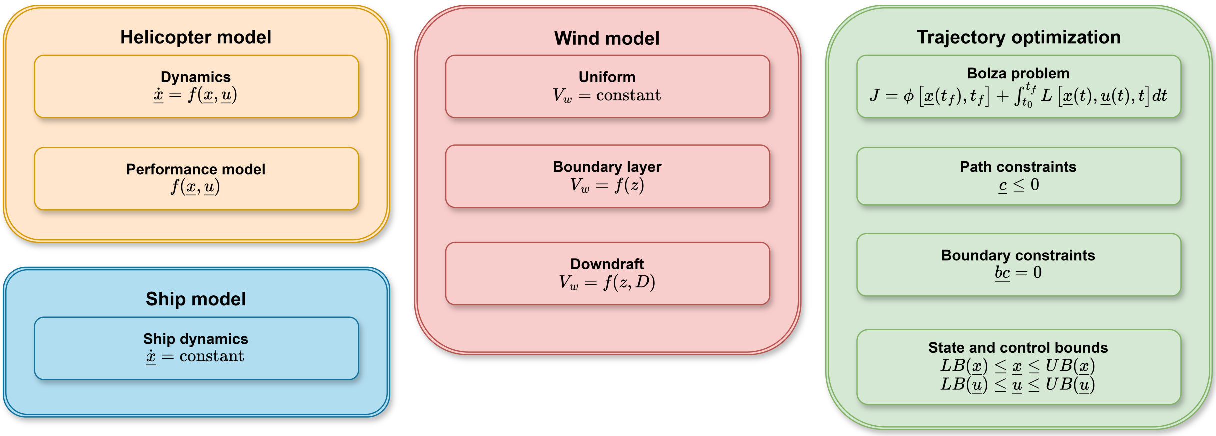

Figure 4.1: High level overview of the entire simulation model

4.1. Assumptions

This section elaborates on the assumptions on which the models are based. The descriptions include both their impact on model complexity and the possible reduction in accuracy and feasibility of the solution.

4.1.1. Environment

The environment in which the ship and helicopter are moving is modelled as closely to reality as possible, without overcomplicating the problem. Therefore, only two assumptions are made for the environmental effects. Firstly, the air density is a function of the helicopter's altitude ($\rho = \rho(z)$) and is computed according to International Standard Atmosphere (ISA) standards [63]. Although high altitude (and thus density) changes are not considered during this study, the effect of density on height is taken into account to improve accuracy compared to using a constant value. Secondly, other environmental effects, such as temperature variations, humidity, or rain are not modelled. Although these parameters could impact the helicopter's power required negatively, it is considered that these effects do not heavily impact the optimized trajectories since a margin in the helicopter's available engine power is used. This means that in reality, the helicopter should have more power available than in the simulation environment to overcome these non-modelled negative environmental effects.

4.1.2. Helicopter

The helicopter model is based on several assumptions to decrease model complexity, improve convergence success rate and reduce computation time. These assumptions are common in optimal control since optimization problems typically involve many design variables and constraints. The first assumption is that the aircraft's motion is simplified to a point mass with three Degrees Of Freedom (3DOF). This low-fidelity model of the helicopter is essential for optimization studies, as high-fidelity helicopter models are too complex and often fail to converge. A consequence of this assumption is the neglect of cross-coupling effects, which are non-desirable secondary control effects of a flying helicopter. While this is a limitation of the model, it is considered that actual control inputs such as collective, cyclic, and pedals are embedded in thrust coefficients, minimizing the impact on optimized trajectories. Additionally, the assumption of decoupled axes leads to higher convergence rates and facilitates result interpretation.

Another assumption is that the Earth is flat, non-rotating, and the gravitational acceleration is constant ($g = 9.80665\,\mathrm{m/s^2}$). These assumptions are justified when the helicopter covers a small distance and does not climb to high altitudes, which is true in the approach phase. The model also assumes that the aircraft mass remains constant throughout the trajectory, which is reasonable for short periods of time and entirely true for electrically driven helicopters. Lastly, the helicopter tail and miscellaneous components are negligible. Although these components could consume around 15% of engine power, it is accepted as a margin is embedded in the power available.

4.1.3. Ship

The main assumptions for the ship involve four items. Firstly, the ship is modelled as a point-mass, with the helicopter landing spot as its center. The finite dimensions of the ship are involved in the No-Go-Zone of the helicopter for collision avoidance. Secondly, the vessel sails in water with sea state 0, meaning that it does not experience any disturbance from the sea. This is because this study focuses on helicopter approaches only, not on deck landings. If deck landings were included, the ship's motions due to the sea should also be incorporated. The third assumption is that the ship sails in a straight line to the North at a constant speed, without changes in heading, speed or acceleration. Lastly, wind effects do not impact the ship's movements. This assumption is also justified by the ship's ability to alter its course and speed through water (without current and wind effects) to match its course and speed over ground, as specified in Section 4.3.

4.2. Helicopter model

The following section provides an overview of the implemented helicopter model. The helicopter dynamics are described by a generic 3DOF point-mass model, which is based on 2D models [57, 58] and expanded to 3D [59, 60]. In this study, the model is further elaborated to include wind effects. A low-fidelity 3D point-mass model is utilised to reduce both model and optimization problem complexities, lower computational time and improve the optimizer's convergence success rates. This section begins with the equations of motion governing the dynamics of a point-mass helicopter. The derivation of the helicopter dynamics and the descriptions of the various coordinate systems are detailed in Appendix A. Subsequently, the helicopter performance model, including thrust and power coefficients, induced velocity, advance ratio and ground effect is highlighted. After that, the test case helicopter and its relevant parameters are presented.

4.2.1. Equations of Motion

Wind is an important factor for helicopter flight paths since this external disturbance has consequences for both the helicopter's air and ground velocities. This means that even in a steady wind field without time or position dependency and constant direction and velocity, the effective motion of the helicopter will vary over time. Wind directly affects the helicopter's drag, as this force depends on air speed rather than ground speed. Therefore, these dependencies are incorporated in the acceleration terms of the helicopter's augmented equations of motion, as defined in Equation 4.1. Future experiments might include wind velocity gradients to model gusts, but they are not considered in this study. Similar to the helicopter velocities, the wind velocity components u_w, v_w and w_w are defined in the Earth reference frame. The acceleration terms resulting from the force equations depend on air speeds, while the position derivatives depend on ground speeds. It is important to note that all quantities are defined in the Moving Earth reference frame, which means that all velocity and position derivatives are relative to the ground, resulting in ground speeds and actual positions when integrated. Three force equations combined with three kinematic equations create a solvable system and result in the following differential equations as illustrated in Equation 4.1.

$$\begin{aligned}
\dot{u} &= \frac{1}{m}\left(C_x \rho (\Omega R)^2 \pi R^2 - f_e \frac{1}{2}\rho (u - u_w) V_{TAS}\right) \\
\dot{v} &= \frac{1}{m}\left(C_y \rho (\Omega R)^2 \pi R^2 - f_e \frac{1}{2}\rho (v - v_w) V_{TAS}\right) \\
\dot{w} &= \frac{1}{m}\left(C_z \rho (\Omega R)^2 \pi R^2 - f_e \frac{1}{2}\rho (w - w_w) V_{TAS} - mg\right) \\
\dot{x} &= u \\
\dot{y} &= v \\
\dot{z} &= \dot{h} = w
\end{aligned} \tag{4.1}$$

In which f_e is the equivalent flat plate area and C_x, C_y and C_z are the thrust coefficients and also the controls of the helicopter in X, Y and Z directions, respectively. The total thrust coefficient is computed as follows:

$$C_T = \sqrt{C_x^2 + C_y^2 + C_z^2} \tag{4.2}$$

In the acceleration terms, V_{TAS} is the true airspeed, which combines the total helicopter ground and wind speeds. The relation between the three velocities is expressed below [64]:

$$\underline{V}_{vehicle/ground} = \underline{V}_{vehicle/air} + \underline{V}_{air/ground} \tag{4.3}$$

This relation states that the velocity of a vehicle relative to the ground is the vectorial sum of the vehicle's airspeed and the wind speed. The equation can be rearranged to find the Total Airspeed V_{TAS}:

$$V_{TAS} = \left|\underline{V}_g - \underline{V}_w\right| = \sqrt{(u - u_w)^2 + (v - v_w)^2 + (w - w_w)^2} \tag{4.4}$$

4.2.2. Performance model

This section elaborates on the performance model of the helicopter, which encompasses the required engine power, induced velocity, advance ratio and ground effect. Note that all velocities mentioned in this section are air speeds.

Required engine power

The engine power required to fly needs to be computed to both measure the helicopter's performance and impose constraints on the optimization. The required power coefficient $C_{P_{req}}$ is computed in a similar approach as [59, 60, 65] and is defined as:

$$C_{P_{req}} = C_T\sqrt{\frac{1}{2}C_W}(K_{ind}f_G\overline{v}_i + \overline{U}_c) + \frac{1}{8}\sigma c_d(1 + 4.65\tilde{\mu}^2) \tag{4.5}$$

With

$$C_W = \frac{W}{\rho(\Omega R)^2\pi R^2} \tag{4.6}$$

This definition of the required power incorporates the thrust coefficient C_T, induced power factor accounting for non-uniform flow K_{ind}, ground effect factor f_G, normalized induced velocity $\overline{v}_i$, normalized velocity perpendicular to the tip-path-plane (TPP) $\overline{U}_c$, solidity of the rotor σ, mean profile drag coefficient of the rotor blades c_d and rotor advance ratio $\tilde{\mu}$. In this way, the induced power, power to climb and profile power are all included. Secondary effects such as tail rotor power and additional installation losses are neglected. The typical value of the induced power factor K_{ind} = 1.15 is used [66]. The solidity of the rotor is defined as:

$$\sigma = \frac{N_b c}{\pi R} \tag{4.7}$$

With N_b the number of blades and c the mean chord of a main rotor blade. The power required is computed using its definition:

$$P_{req} = C_{P_{req}}\rho(\Omega R)^3\pi R^2 \tag{4.8}$$

Induced velocity

Induced air velocity is caused by an acceleration of airflow through the main rotor, resulting in a thrust force. For a helicopter in hover, the thrust T is equal to the weight W, leading to the following relation for the induced velocity in hover [66]:

$$v_{hov} = \sqrt{\frac{T}{2\rho\pi R^2}} = \sqrt{\frac{W}{2\rho\pi R^2}} = \Omega R\sqrt{\frac{C_W}{2}} \tag{4.9}$$

The normalized induced velocity $\overline{v}_i$ can be calculated using the approach of Zhao, Jhemi, and Chen [57] by distinguishing two conditions; namely inside and outside the vortex ring state. To determine the normalized induced velocity in these conditions, two components of the induced velocity need to be computed first, being the normalized main rotor climb velocity $\overline{U}_c$, the velocity component perpendicular to the TPP and the normalized tangential component $\overline{U}_t$, the velocity component parallel to the TPP [59].

$$\begin{aligned}
\overline{U}_c &= \frac{U_c}{v_{hov}} = \frac{uC_x + vC_y + wC_z}{v_{hov}C_T} \\
\overline{U}_t &= \frac{U_t}{v_{hov}} = \frac{\sqrt{u^2(C_y^2 + C_z^2) + v^2(C_x^2 + C_z^2) + w^2(C_x^2 + C_y^2) - 2uvC_xC_y - 2uwC_xC_z - 2vwC_yC_z}}{v_{hov}C_T}
\end{aligned} \tag{4.10}$$

The normalized induced velocity can now be calculated using [57, 58]. The normalized induced velocity outside the vortex ring state (condition 1) must be solved numerically, inside the vortex ring state (condition 2) can be computed directly.

$$\overline{v}_i = \begin{cases} \overline{v}_i^4 + 2\overline{U}_c\overline{v}_i^3 + (\overline{U}_c^2 + \overline{U}_t^2)\overline{v}_i^2 = 1 & \text{if } (2\overline{U}_c + 3)^2 + \overline{U}_t^2 > 1 \\ \overline{U}_c(0.373\overline{U}_c + 0.598\overline{U}_t - 1.991) & \text{otherwise} \end{cases} \tag{4.11}$$

Advance ratio

The advance ratio $\tilde{\mu}$ is defined as the in-plane forward velocity normalized by the rotor tip speed [67].

$$\tilde{\mu} = \frac{V \cos \alpha_D}{\Omega R} \tag{4.12}$$

Where α_D is the rotor disc angle of attack and can be found geometrically by the force directions in trimmed flight:

$$\sin \alpha_D = \frac{D_{fus} + W \sin \gamma}{T} \tag{4.13}$$

Ground effect

The ground effect has major effects on the lift performance of the main rotor, reducing the power required to fly or hover. Because the helicopter will approach the ship in this study, the aircraft will fly close to the deck at some point in time and thus will be affected by the ground effect. To model the ground effect the relation from Zhao, Jhemi, and Chen [57] is used which uses a source model from Cheeseman and Bennet [68]. Note that the point-mass equations of motions describe the dynamics of the centre of gravity, which is assumed to be located at the centre of the rotor disk. However, the model for the ground effect takes into account the height of the rotor hub above the ground.

$$f_G = 1 - \frac{R^2 \cos^2 \theta_w}{16(h + H_R)^2} \tag{4.14}$$

In this relation, H_R is the height from the ground to the main rotor hub and θ_w is the angle between the rotor wake and a vertical reference line, defined as:

$$\cos^2 \theta_w = \left[1 + \frac{(V_{xy}C_T + \nu C_{xy})^2}{wC_T + \nu C_z^2}\right]^{-1} \tag{4.15}$$

With:

$$\nu = K_{ind} v_{hov} \overline{v}_i f_G \tag{4.16}$$

These three equations need to be solved numerically in a sub-routine of the performance model. Besides, V_{xy} and C_{xy} are the horizontal components of the velocity and thrust coefficient, respectively.

$$V_{xy} = \sqrt{u^2 + v^2} \quad C_{xy} = \sqrt{C_x^2 + C_y^2} \tag{4.17}$$

4.2.3. Selection of helicopter

This study utilizes the PH-1AA Orange Eye helicopter (see Figure 4.2) as a test case. This small, unmanned conventional helicopter has a main rotor diameter of 3.3 m, a weight of 60 kg (empty) up to 100 kg (maximum weight with payload) and is owned by the Netherlands Aerospace Centre (NLR). The original UAV was equipped with a gas turbine, but now the propulsion system is electric. This UAV is primarily used for experimental research and represents the future deployment of other UAVs by the RNLN. This helicopter is used in projects such as NOTUS, which has provided insight into ship-UAV interactions and landings [8]. The helicopter parameters used in this study are listed below. Some parameters were estimated or assumed to complete the helicopter model, as some were either unclearly defined or unknown. This is detailed in Appendix B.

Figure 4.2: PH-1AA Orange Eye helicopter used in this study^{L}

Table 4.1: PH-1AA Orange Eye parameters

Parameter	**Symbol**	**Value**	**Unit**
Mass	m	100	kg
Main rotor rotational speed	Ω	750 (78.5398)	rpm (rad/s)
Main rotor radius	R	1.6652	m
Main rotor blade chord	c	0.11	m
Main rotor blade friction drag coefficient	c_d	0.010 (NACA0012)	-
Equivalent flat plate area	f_e	2 (0.1858)	ft^2 (m^2)
Number of blades	N_b	3	-
Height from ground to main rotor hub	H_R	0.9251	m
Induced power factor	K_{ind}	1.15	-
Power Reserve Ratio	PRR	10	%
Figure of Merit	M	0.6977	-
Power available (sea level)	P_a	10.48	kW
Maximum thrust coefficient	$C_{T_{max}}$	0.0059	-
Maximum endurance velocity	V_{endur}	18.78 (36.50)	m/s (kts)
Maximum range velocity	V_{range}	27.01 (52.50)	m/s (kts)
Maximum velocity	V_{max}	38.56 (74.95)	m/s (kts)
Never-exceed speed	V_{NE}	52.32 (101.69)	m/s (kts)

4.3. Ship model

Similar to the helicopter, the ship's deck is also modelled as a point-mass, but with constant velocity components in the Moving Earth reference frame. The vessel sails North in a calm sea, without being affected by sea state effects or the wind. The model incorporates the ship's dimensions for collision avoidance, effectively treating the vessel as a rigid body. The total ship model is given in Equation 4.18 where the velocity constants are C_u = 16 kts, C_v = 0 kts and C_w = 0 kts, which is suitable for a patrol vessel during standard operations in calm sea conditions.

$$\begin{aligned} \dot{u}_{ship} &= 0 & \dot{x}_{ship} &= u_{ship} = C_u \\ \dot{v}_{ship} &= 0 & \dot{y}_{ship} &= v_{ship} = C_v \\ \dot{w}_{ship} &= 0 & \dot{z}_{ship} &= w_{ship} = C_w \end{aligned} \tag{4.18}$$

4.3.1. Choice of ship

A Holland-Class Ocean-Going Patrol Vessel (OPV)[V] acts as the UAV's mothership, as depicted in Figure 4.3. The four patrol vessels have been actively serving in the RNLN since 2012 and are primarily deployed in low-violence areas, such as counter-drugs operations near the Caribbean coasts. The dimensions of this vessel are stated in Table 4.2.

Figure 4.3: Holland-Class Ocean-Going Patrol Vessel of the RNLN

Table 4.2: Holland-Class Ocean-Going Patrol Vessel (OPV) dimensions

Parameter	Value [m]
Length	108.4
Width	16.0
Height	18
Length helicopter deck	28.13

4.4. Trajectory optimization

This section discusses the trajectory optimization problem. First, the control variables are converted to damp control efforts, smooth the trajectory and increase convergence. Afterwards, the model state and control variables are elaborated and scaled in the optimization framework. The objective function and a thorough explanation of the performance and boundary constraints are considered. Furthermore, the algorithm that solves the optimal control problem is explained. The section concludes with a summary of the trajectory optimization problem and an overview of the simulation model, including all relevant equations.

4.4.1. Control damping

Control inputs can be of fluctuating nature caused by fast-varying response needs. For example, in heavily turbulent areas the helicopter states could oscillate quickly resulting in heavy control fluctuations. This behaviour negatively impacts the convergence of the optimization problem, requiring a significantly larger amount of iterations to converge to an optimal solution [56]. Therefore, new control variables are defined for the optimization problem:

$$u_1 = \dot{C}_x \quad u_2 = \dot{C}_y \quad u_3 = \dot{C}_z \tag{4.19}$$

The control variables are included in the system of differential equations to obtain a smooth time-varying response of the thrust coefficients. This incremental form of control enables lower convergence time and a higher chance of finding an optimal solution. Next to this, state constraints can be imposed on the thrust coefficients, decreasing the number of required constraints and lowering the computational overhead even more.

4.4.2. Model variables

State and control variables need to be defined for the optimal control problem. Because this problem contains two dynamically evolving systems, the state variables should include the helicopter and ship speeds and positions. However, since the ship velocities are fixed, its positions change linearly in time and are not affected by control variables. Therefore, the ship's movements are computed directly and effectively act as a time-dependent constraint on the helicopter. The entire model could be extended by implementing controls into the ship model such that it can manoeuvre in time, but that is not needed for this study. As a result, the ship's equations of motion are implemented by a subroutine, reducing the total amount of design variables to only those of the helicopter. Because of the decision to change the helicopter controls C_x, C_y and C_z to state variables, the total amount of state variables sums up to 9:

$$\underline{x} = \Big[u, v, w, x, y, z, C_x, C_y, C_z\Big]^T \tag{4.20}$$

Due to the control damping, the augmented control variables are:

$$\underline{u} = \left[\tfrac{dC_x}{dt}, \tfrac{dC_y}{dt}, \tfrac{dC_z}{dt}\right]^T \tag{4.21}$$

Which adds three extra differential equations to the total set as denoted in Equation 4.1:

$$\begin{aligned} \dot{C}_x &= u_1 \\ \dot{C}_y &= u_2 \\ \dot{C}_z &= u_3 \end{aligned} \tag{4.22}$$

4.4.3. Variable scaling

Variable scaling is important for a successful convergence of the optimization problem. This process ensures that all states and controls are of similar magnitudes, smoothing the problem and objective function derivatives with respect to all design variables. The scaling process utilizes the approach of [57] by normalizing all distances by $10R$ and time by $100/\Omega$. Consequently, all velocities are normalized by $\Omega R/10$ and accelerations by $1000/\Omega R^2$. In addition, controls are scaled by 10^{-3} [59]. The helicopter's equations of motion are scaled accordingly. The augmented state and control variables are defined as:

$$\begin{aligned} x_1 &= \frac{10u}{\Omega R} & x_2 &= \frac{10v}{\Omega R} & x_3 &= \frac{10w}{\Omega R} \\ x_4 &= \frac{x}{10R} & x_5 &= \frac{y}{10R} & x_6 &= \frac{z}{10R} \\ u_1 &= 10^3\frac{dC_x}{d\tau} & u_2 &= 10^3\frac{dC_y}{d\tau} & u_3 &= 10^3\frac{dC_z}{d\tau} \\ \tau &= \frac{t\Omega}{100} \end{aligned} \tag{4.23}$$

4.4.4. Objective function

The helicopter needs to approach the ship as smoothly and fast as possible, subjected to certain wind conditions, performance, and boundary constraints. A smooth trajectory is characterized by a continuous flight path with little control actions. The trajectory is already smoothened because the thrust coefficients' derivatives are employed as control variables, allowing the thrust coefficients to be continuous, smoother across the entire interval and partially simulating actuator response delays [58]. No constraints are imposed on these pseudo-controls, however, a quadratic control penalty term has been added to the Lagrange term of the objective to avoid unnecessary large control inputs and to smoothen the trajectory solution further. This objective would only result in maximum time trajectories, which is not desired because a quick approach and recovery are preferred from an operational point of view. Therefore, the final time is included in the objective as end-cost or Mayer term. The weighting factor K_{t_f} is added to match the magnitudes of both contributions and tune the importance of time compared to the control effort. Note that non-dimensional quantities are employed in the objective function, meaning that the optimizer minimizes Equation 4.24.

$$J = K_{t_f}\tau_f + \int_{\tau_0}^{\tau_f} \left(u_1^2 + u_2^2 + u_3^2\right) d\tau \tag{4.24}$$

4.4.5. Performance constraints

Helicopter performance constraints must be imposed in order to limit the optimizer. These constraints are active along the entire path and must be satisfied to deem a result feasible. First and foremost, the helicopter's engine restricts the maximum thrust and power that can be produced. The maximum thrust coefficient is constraint by:

$$C_T \leq C_{T_{max}} \frac{\rho_{sea}}{\rho(z)} \tag{4.25}$$

Moreover, the main rotor cannot generate downward thrust, causing a constraint on the vertical thrust coefficient. The negligible tilt angle between the body and Earth reference frames is disregarded in this conversion, making it possible to convert the path constraint into a state lower bound.

$$C_z \geq 0 \tag{4.26}$$

Subsequently, the power required to fly could never exceed the maximum engine's available power:

$$P_a \geq P_{req} = C_{P_{req}} \rho (\Omega R)^3 \pi R^2 \tag{4.27}$$

Where $C_{P_{req}}$ is computed using Equation 4.5.

A helicopter needs to tilt to the side in order to change its heading, which is known as the bank angle. A constraint on the bank angle is imposed to prevent the helicopter from making overly steep turns and from flying upside down. This constraint is necessary because a mathematically correct solution in this case might not be feasible in the real world. This restriction is similar to the approach utilized in a previous study, where the helicopter remains free to turn tightly by adjusting its flight speed [60]. By computing the rate of change of the heading angle χ over time, the following expression is found:

$$\dot{\chi} = \frac{u\dot{v} - \dot{u}v}{u^2 + v^2} \tag{4.28}$$

For a steady turn, the rate of turn can be introduced to obtain a relation between the bank angle μ, heading rate $\dot{\chi}$, flight speed V and gravitational constant g:

$$\mu = \text{atan}\left(\frac{\dot{\chi} V}{g}\right) \tag{4.29}$$

In the Aeronautical Design Standard 33 (ADS-33) [69], the United States Army Aviation and Missile Command states that a bank angle of $\mu_{max} = 30°$ is acceptable for achieving aggressive agility in forward flight. Since the vehicle being studied is a UAV, passenger comfort is not relevant, and aggressive agility is justified. Additionally, this maximum bank angle results in a maximum load factor of about 1.15 in a medium turn, which does not have detrimental effects on flying qualities [70].

Furthermore, it is essential to avoid collisions between the helicopter and ship. Several studies for aircraft trajectory optimization with collision [71] and quadcopter obstacle avoidance [72] have shown methods for this problem. The one which is most compatible for this study is the method from Xiang, Shen, and Li [73]. In this method, the obstacle is parameterized as a three-dimensional cube that is able to move in space as a function of time. The cubic approximation of the ship ("NoGoZone") simplifies the model and creates additional safety zones around the ship. The spatial positions of the obstacle in the Earth reference frame can be donated as $X_1(t)$, $X_2(t)$; $Y_1(t)$, $Y_2(t)$; and $Z_1(t)$, $Z_2(t)$. The size of the moving obstacle along the three axes is:

$$\begin{cases} \Delta X = X_2(t) - X_1(t) \\ \Delta Y = Y_2(t) - Y_1(t) \\ \Delta Z = Z_2(t) - Z_1(t) \end{cases} \tag{4.30}$$

The point of interest, in this case the position of the helicopter in the Earth reference frame, can be denoted as an arbitrary point in space (x, y, z). To obtain information on whether the helicopter is inside or outside the NoGoZone, a new scalar is defined as follows:

$$C = 2|XX\,||YY\,||ZZ\,| + XX\,|YY\,||ZZ\,| + |XX\,|YY\,|ZZ\,| + |XX\,||YY\,|ZZ \tag{4.31}$$

Where

$$XX = \frac{(x - X_1)(x - X_2)}{\Delta X},\ YY = \frac{(y - Y_1)(y - Y_2)}{\Delta Y},\ ZZ = \frac{(z - Z_1)(z - Z_2)}{\Delta Z} \tag{4.32}$$

The value of C is computed to know whether the helicopter and ship have crashed into each other. If the inequality $C \leq 0$ is true, meaning that $XX \leq 0$, $YY \leq 0$ and $ZZ \leq 0$, the helicopter with coordinates (x, y, z) is positioned inside the NoGoZone and has collided with the vessel. On the other hand, if inequality $-C \leq 0$ is true, the helicopter is located outside the NoGoZone.

Although modelled as a point mass, the helicopter is a rigid body with finite dimensions. Therefore, the sizes of the NoGoZone are enlarged to ensure that the optimized flight trajectory does not result in unsafe situations. The enlargement is set to the helicopter's main rotor diameter. The dimensions of the NoGoZone are set to the dimensions of the ship. Figure 4.4 illustrates the helicopter, landing deck and NoGoZone at a certain timestamp. The Hard NoGoZone is defined as the ship's hull minus the flight deck. The Safe NoGoZone is the Hard region enlarged by the rotor diameter and is employed as the constraint standard. In the illustrated situation, the value of $-C$ is negative and thus feasible.

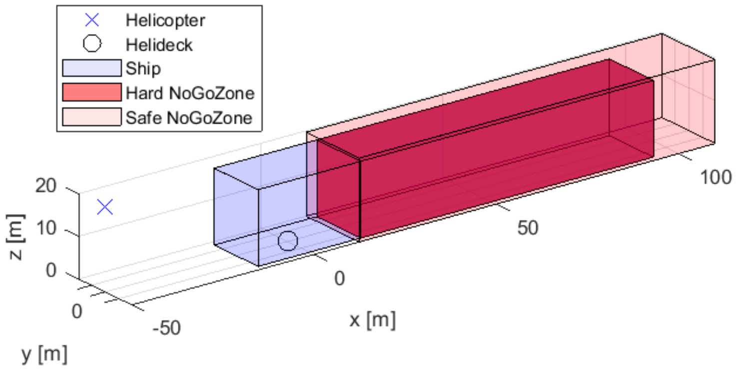

Figure 4.4: Visualization of the NoGoZone utilized as path constraint during the optimization. The Hard NoGoZone is the ship minus the flight deck, while the Safe NoGoZone is the Hard region enlarged with the helicopter's main rotor diameter. Axes lengths are modified to represent actual dimensions.

A couple more constraints need to be introduced. Because the helicopter flies close to the sea surface, it should be restricted to a minimum safe altitude (MSA). Normally a helicopter is restricted to a surface ceiling, but this constraint is omitted as the helicopter will never exceed this altitude during the approach. Lastly, the helicopter needs a constraint on its maximum velocity. In forward flight, the helicopter's retreating blade experiences reversed flow, whereas the advancing blade is limited by compressibility and shock-wave effects [66]. For helicopters with a small tip speed ΩR, the maximum velocity is bounded by the reversed flow from the retreating blade. This Never Exceed Speed (V_{NE}) is reached for an advance ratio of $\tilde{\mu} = 0.4$ [66]. All path constraints are summarized in Table 4.3.

Table 4.3: Summary helicopter path constraints

Path Constraint	**Inequality**
Maximum thrust coefficient	$C_T \leq C_{T_{max}} \frac{\rho_{sea}}{\rho(z)}$
Rotor upward thrust	$C_z \geq 0$
Power constraint	$P_{avail} \geq P_{req}$
Maximum bank angle	$\mu \leq \mu_{max}$
Collision avoidance	$-C \leq 0$
Minimum safe altitude (MSA)	$h > h_{min}$
Never exceed speed	$V_{TAS} \leq V_{NE}$

4.4.6. Boundary conditions

Boundary conditions fix parameters at the initial and final nodes of the mesh and are therefore referred to as initial and final conditions. The simulation starts with the helicopter and ship in fixed positions, imposing boundary conditions on the initial helicopter location. The helicopter is trimmed, meaning that no accelerations act on the vehicle, and flies horizontally at cruise speed. In the last time step of the approach, the helicopter is in a steady hover above the flight deck relative to the ship, meaning that its forward velocity equals the ship's speed and all accelerations are zero. Since the helicopter approaches the ship and stops at a hover position above the landing deck, some final conditions are dynamic, which require relative positions and velocities to impose final boundary conditions. For clarity and without loss of generality, all ship terms have been included in the definition of the relative motions:

$$
\begin{aligned}
dx &= x_{heli} - x_{ship} & d\dot{x} &= du = u_{heli} - u_{ship} & d\ddot{x} &= d\dot{u} = \dot{u}_{heli} - \dot{u}_{ship} \\
dy &= y_{heli} - y_{ship} & d\dot{y} &= dv = v_{heli} - v_{ship} & d\ddot{y} &= d\dot{v} = \dot{v}_{heli} - \dot{v}_{ship} \\
dz &= z_{heli} - z_{ship} & d\dot{z} &= dw = w_{heli} - w_{ship} & d\ddot{z} &= d\dot{w} = \dot{w}_{heli} - \dot{w}_{ship}
\end{aligned} \tag{4.33}
$$

Relative motions in z-direction are not used as boundary constraints because limits for initial and final vertical positions and velocities can be imposed directly on the variables z and w. Initial positions x_0 and y_0 are imposed similarly. However, this is not the case for accelerations and horizontal velocities since accelerations are not state variables and horizontal velocities depend on both magnitude (fixed) and heading angle (free). Boundary constraints on accelerations can be imposed by equalizing the initial and final helicopter's equations of motion to zero. The imposed boundary conditions are summarized in Table 4.4.

Table 4.4: Summary helicopter boundary constraints

Boundary Constraint	**Equality**
Initial position	$x(t_0) = x_0, y(t_0) = y_0, z(t_0) = z_0$
Initial cruise speed	$V(t_0) = V_{cruise}, w(t_0) = 0$
Initial accelerations	$\dot{u}(t_0) = \dot{v}(t_0) = \dot{w}(t_0) = 0$
Final position	$dx(t_f) = dy(t_f) = 0, z(t_f) = z_f$
Final velocity	$du(t_f) = dv(t_f) = 0, w(t_f) = 0$
Final accelerations	$\dot{u}(t_f) = \dot{v}(t_f) = \dot{w}(t_f) = 0$

4.4.7. Solver

The optimal control problem of helicopter-ship approaches is solved using separate transcription and solver methods. First, the optimal control problem is converted into a solvable Nonlinear Programming (NLP) problem, a process called transcription. This procedure is carried out by the direct collocation method in *ICLOCS2* [74], created by the Imperial College London. The algorithm is widely used and validated for many optimal control problems, including multi-phase problems and supports automatic mesh refinement. The direct collocation method is considered one of the most effective direct numerical methods for path-constrained trajectory optimization [58]. This technique converts a continuous optimal control problem into a segmented parameter optimization problem by approximating the state and control trajectories using polynomial splines, with the accuracy and fidelity of the approximation determined by the order of these splines. For example, the Hermite-Simpson method for direct collocation uses quadratic polynomials to approximate control segments and cubic polynomials to approximate states [52]. The polynomials are connected at the grid or knot points. In between these locations, collocation points are defined, where the slope of each approximated spline should match the differential equations of motion. The error between the two is expressed as the defect and is forced to zero for solving the system, which is the key to the collocation method.

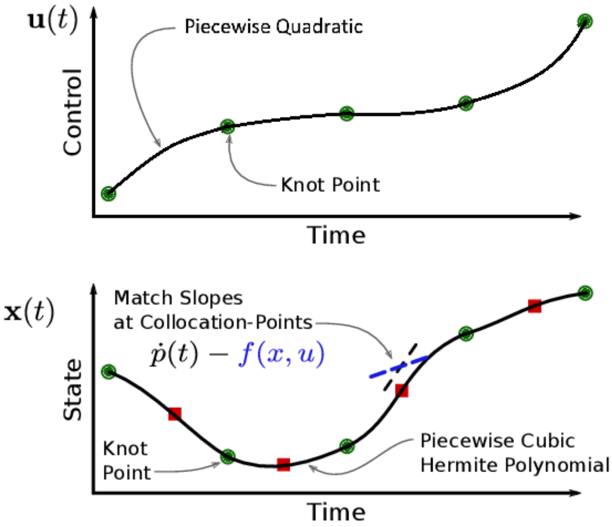

Figure 4.5: Visualization of the Direct collocation method [52]

After the optimal control problem has been transcribed into an NLP problem, a solver using NLP techniques minimizes the objective function while adhering to all constraints. Although not recommended by the developers of *ICLOCS2*, the MATLAB built-in function *fmincon* is used for solving the optimization problem[W]. The recommended solver caused many convergence problems due to large adjustments of the tuneable variables, which are detrimental for the vortex-ring state and ground effect subroutines. Additionally, it was difficult to follow the optimization process adequately in order to spot premature divergences. With the Sequential Quadratic Programming (SQP) technique [75], *fmincon* is computationally faster than the recommended solver, despite requiring more iterations. Moreover, it is tunable, user-friendly, and finds the optimum more smoothly.

4.5. Summary of the Trajectory Optimization Framework

The optimization problem is defined and implemented in the negative null form as shown below. The objective is to minimize the combination of time and control fluctuations, subjected to five path constraints. These constraints limit the optimizer to not exceed the maximum thrust, power, bank angle and velocity, as well as prevent collisions between the helicopter and ship. As long as these constraint values are below zero throughout the entire trajectory, the solution is deemed feasible. In addition to the five inequality constraints, eleven equality constraints are defined. These boundary constraints make sure the helicopter is above the flight deck in trimmed condition in the final time step of the approach and starts at cruise speed while flying trimmed. All states and controls, either in the initial or final time steps or during the approach, must adhere to lower and upper bounds. These bounds can be free or fixed. For example, the initial location is fixed as the helicopter starts from a defined point relative to the ship, but the final location in space is free, as long as the helicopter finalizes the approach by hovering above the landing spot. Another example is that the lower bound of the vertical thrust component is set to zero at every moment of the manoeuvre.

$$
\begin{array}{ll}
\underset{\underline{u}}{\text{minimize}} & J = K_{t_f}\tau_f + \displaystyle\int_{\tau_0}^{\tau_f} \left(u_1^2 + u_2^2 + u_3^2\right) d\tau \\
\text{subject to} & \dfrac{C_T}{C_{T_{max}}}\dfrac{\rho(z)}{\rho_{sea}} - 1 \leq 0, \\
& \dfrac{P_{req}}{P_a} - 1 \leq 0, \\
& \dfrac{|\mu|}{\mu_{max}} - 1 \leq 0, \\
& \dfrac{V_{TAS}}{V_{NE}} - 1 \leq 0, \\
& -C \leq 0, \\
& dx(t_f) = 0, \quad dy(t_f) = 0, \\
& du(t_f) = 0, \quad dv(t_f) = 0, \\
& \dot{u}(t_f) = 0, \quad \dot{v}(t_f) = 0, \quad \dot{w}(t_f) = 0, \\
& \dot{u}(t_0) = 0, \quad \dot{v}(t_0) = 0, \quad \dot{w}(t_0) = 0, \\
& V_{air}(t_0) - V_{cruise} = 0, \\
& LB[\underline{x}(t_0)] \leq \underline{x}(t_0) \leq UB[\underline{x}(t_0)], \quad LB[\underline{u}(t_0)] \leq \underline{u}(t_0) \leq UB[\underline{u}(t_0)], \\
& LB[\underline{x}(t)] \leq \underline{x}(t) \leq UB[\underline{x}(t)], \qquad LB(\underline{u}(t)) \leq \underline{u}(t) \leq UB[\underline{u}(t)], \\
& LB[\underline{x}(t_f)] \leq \underline{x}(t_f) \leq UB[\underline{x}(t_f)], \quad LB(\underline{u}(t_f)) \leq \underline{u}(t_f) \leq UB[\underline{u}(t_f)]
\end{array}
\tag{4.34}
$$

The entire framework is shown in detail in Figure 4.6 on the next page. This visualization includes four major blocks with dependency links between functions. The program starts with an initial guess of the trajectory, which may consist of state and control values for only the initial and final points. If this is the case, the transcription algorithm automatically interpolates the values of the intermediate time stamps. The next step is computing the dynamics of the ship and helicopter, the latter needing information about the wind speed components and are implemented in normalized form. Although non-controllable and constant, the ship model is added for completeness and in the case of future modifications. Based on the selected wind model, the helicopter dynamics are calculated and passed to the constraints block.

Both path and boundary constraints are evaluated in the constraints block, using information about the wind, helicopter dynamics, ship motions and additional functions. These functions involve models for anti-collision and helicopter performance, the latter including the induced velocity, ground effect, and required thrust and power. The needed values are passed to the path constraints. The last block defines the objective function and is divided into a Mayer end-cost term and a Lagrange cost, which is integrated along the trajectory. The sum of the two components defines the total objective and is provided to the optimizer, together with the constraint values. Before the run starts, the user needs to define certain optimization settings and convergence thresholds. The loop is iterated in which the optimizer minimizes the objective function while adhering to all path and boundary constraints. When it has found a feasible converged solution, the outcome is tested by the pre-defined accuracy thresholds. If the level of accuracy is insufficient, the mesh is refined and the inaccurate solution is used as a new starting point to trigger the next optimization run. The entire process is finished if a converged solution complies with the pre-defined accuracy thresholds.

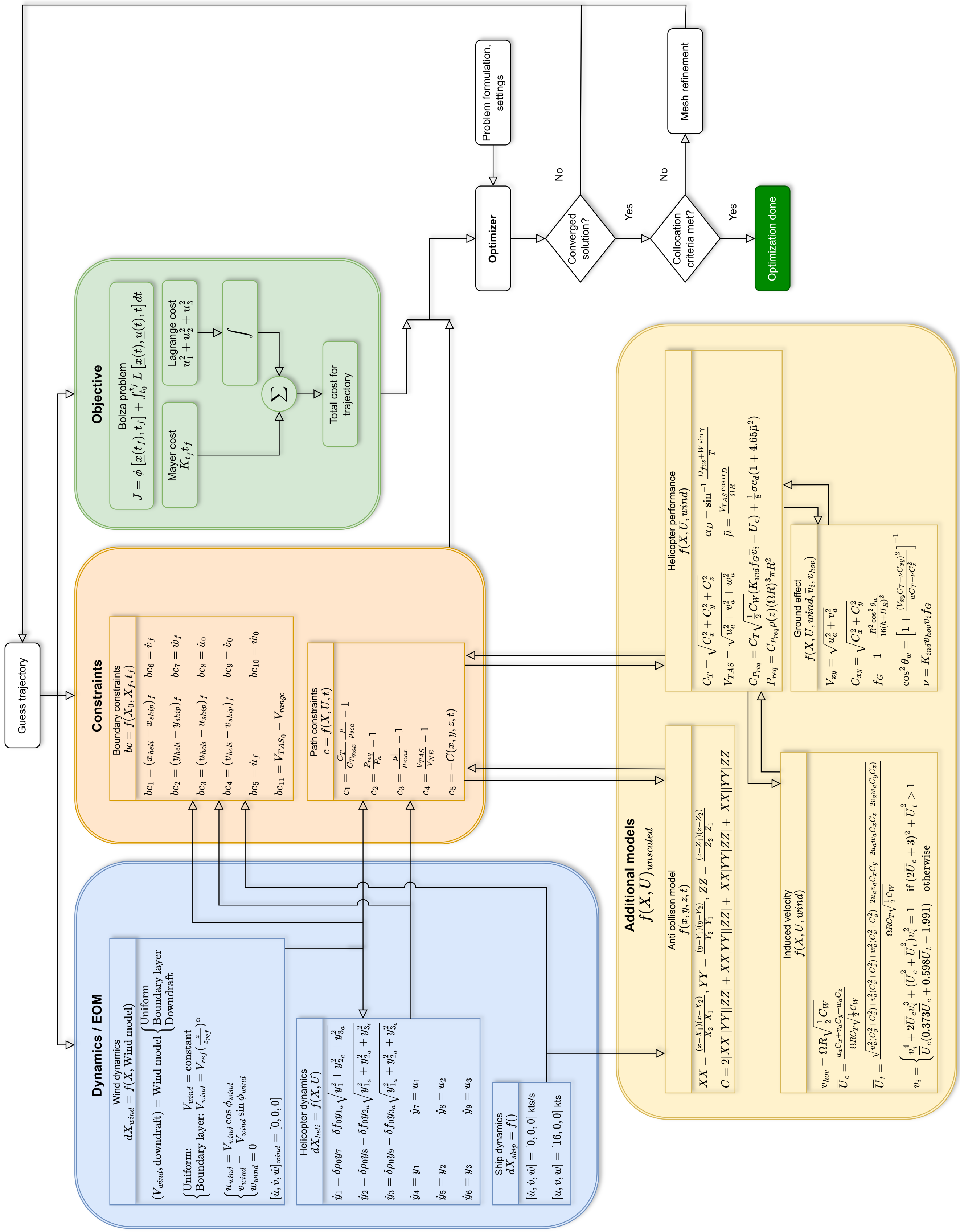

Figure 4.6: Overview of the entire simulation model

5

Experiments

This chapter elaborates on the performed experiments with the proposed method to answer the research questions. Firstly, the experiment setup is discussed, involving the helicopter's initial position, ship movement and wind characteristics. After this, all wind models used in the experiments are discussed, followed by a sensitivity analysis to determine the weighting factor K_{t_f} of the objective function. A baseline scenario is optimized to find a suitable value for this parameter and is verified by one wind condition. Afterwards, the objective function is fixed and is used in all experiments. This chapter concludes with the method of post-processing the experimental simulation data.

5.1. Experiment setup

All experiments follow a similar setup as displayed in Figure 5.1. The simulation's origin is the initial location of the helicopter's landing spot. As time progresses, both the helicopter and ship positions are described relative to this point. However, their positions can also be related to each other to simplify the result analysis. The helicopter starts at different locations to assess the influence of the starting position. Because of symmetry, only four locations around the ship are considered, which reduces the amount of optimization runs significantly. The helicopter starts at a distance of 1 km from the ship in relative angles $000°$, $045°$, $090°$ and $135°$, meaning that the helicopter sees the landing spot in these heading angles. The position in front of the ship ($180°$) is not taken into account, since an approach from this location is assumed impractical and not operationally feasible. At the initial time step, the helicopter is trimmed and flies at cruise speed. The approach ends when the helicopter is in a steady hover relative to the vessel, 5 m above the flight deck. The ship sails in calm waters at a constant speed of 16 kts to the North without any heading changes and wind comes from all points of the compass, with speeds varying from 0 kts to 40 kts.

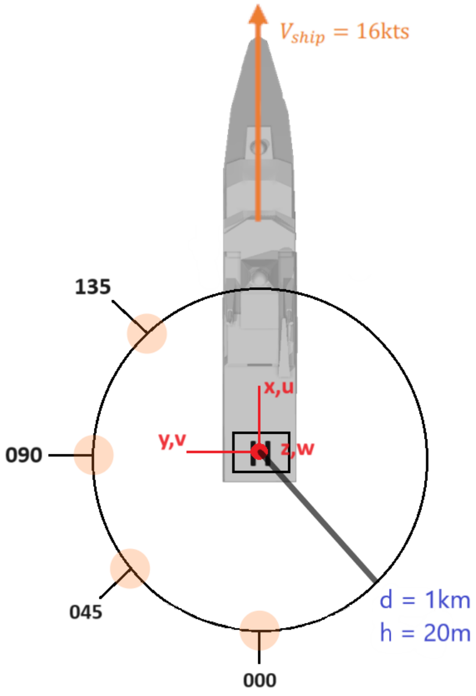

Figure 5.1: Initial conditions for all experiments

The experiment setup is used in three different wind models. Table 5.1 shows the conducted experiments for each of the three employed wind models with their purposes. Both uniform and boundary layer wind models are used for all described initial positions, wind directions, and speeds to assess the effects of wind on optimal approaches and perform a sensitivity analysis of wind model fidelity. The downdraft model combines the boundary layer wind with a realistic large-scale effect behind the ship's hangar. This effect is strongest for the ship's relative headwinds, which is why only Northerly and Southerly winds of several speeds are considered. The outcomes are assumed to be similar for every initial helicopter location, so only position 000° is used to decrease computational effort. Similarly, computational costs are minimized by assessing wind directions with intervals of 45° and wind speeds of 10 kts.

Table 5.1: Summary conducted experiments of the utilized wind models with their entailed conditions and purposes

Wind model	Initial position	Wind direction	Wind speed	Purpose
Uniform	000° to 135°	000° to 315°	0 kts to 40 kts	Simple model to assess the effects of wind on optimal trajectories
Boundary layer	000° to 135°	000° to 315°	0 kts to 40 kts	More realistic wind model including wind gradient; sensitivity analysis on wind model fidelity
Downdraft	000°	000° and 180°	0 kts to 30 kts and 10 kts	Large scale effect around flight deck; initial assessment of operational limits

5.2. Wind models

Three progressively more realistic wind models are utilized in this study and are all compared to the baseline no-wind condition. The three models include two major vector fields: a uniform and boundary layer wind field, and a minor field to describe the downdraft near the helicopter deck. All winds are defined in the Earth reference frame. This means that WOD speeds will be different in reality, but they can be easily computed due to the linear movement of the ship. Because of this definition, the wind direction in the simulation environment is expressed as "going-to" instead of "coming-from". The results chapter maintains the general convention by flipping all wind directions.

5.2.1. Uniform wind field

The first model consists of a uniform wind field that neither depends on position nor altitude. This wind field provides a preliminary perspective of how wind affects optimal helicopter-ship approaches. Two horizontal speed components, which are constant throughout the entire domain, characterize this wind field depending on the wind velocity and direction. Wind angles ranging from 000° to 315°, at intervals of 45° are used with wind speeds ranging from 0 kts to 40 kts, at intervals of 10 kts. A wind speed of 40 kts is equivalent to wind force 8 on Beaufort's scale. Even though the RNLN requires UAV deployment in winds up to 7Bf, it is important to assess whether higher wind speeds are executable or if the helicopter approaches its limits as weather conditions can change rapidly. Due to symmetry, winds from the right half plane (to directions 225° to 315°) are omitted for the 000° starting position to minimize computational efforts. Instead, results are mirrored for this initial position.

The total wind speed V_w and azimuth angle ϕ_w are converted to u_w and v_w components in the Earth Reference frame by the equations below, which is why wind is defined as "going-to". Since only horizontal winds are examined, the vertical component $w_w = 0$.

$$
\begin{aligned}
u_w &= V_w \cos \phi_w \\
v_w &= -V_w \sin \phi_w
\end{aligned}
\tag{5.1}
$$

5.2.2. Boundary layer wind field

A more realistic wind model is a boundary layer profile. Due to surface roughness, the horizontal wind velocity magnitude tends to be lower near the surface than at high altitudes, introducing shear layers as a function of distance from the ground. This phenomenon is also known as the Atmospheric Boundary Layer (ABL) and its shape depends on atmospheric parameters such as temperature, humidity, and stability [76, 77]. A common method to model the boundary layer wind profile is by using the power law, as depicted in Equation 5.2. This equation is frequently used in engineering for its simplicity and ability to provide accurate results, which have been validated by more advanced models [78]. The model becomes more accurate by incorporating the effect of shear and velocity deficit near the surface, but it does not consider the impact of wind direction with altitude. While this is a limitation of the model, it is not expected to significantly affect the results, as the effect is considered minimal above the sea.

$$\frac{V}{V_{ref}} = \left(\frac{z}{z_{ref}}\right)^{\alpha} \tag{5.2}$$

The power law computes the wind speed V as a function of altitude z when the velocity V_{ref} at a reference height z_{ref} is known. This reference velocity can be found based on real-time measurements from buoys^{X} or from the ship's own wind measurement system. The expression utilizes the exponent α, which dictates the shape of the velocity curve. This parameter takes on different values for wind over a city than over a flat sea, as it depends on surface roughness and atmospheric stability. It has been shown that $\alpha = 0.11$ is applicable for a wind profile under near-neutral stability conditions at sea [79]. Therefore, this value is used for the boundary layer wind model.

For the experiments, the reference altitude is $z_{ref} = 20\,\text{m}$, which is consistent with the uniform wind experiments being the initial altitude of the helicopter. The curve of the boundary layer wind field is shown in Figure 5.2. The reference wind velocities and azimuth angles are similar to the previous experiment, respectively ranging from 0 kts to 40 kts, at intervals of 10 kts and 000° to 315° (or 000° to 180° for the 000° starting position), at intervals of 45°. Similarly, the conversion from wind speed and azimuth angle to wind components in the Earth axes system is carried out by Equation 5.1.

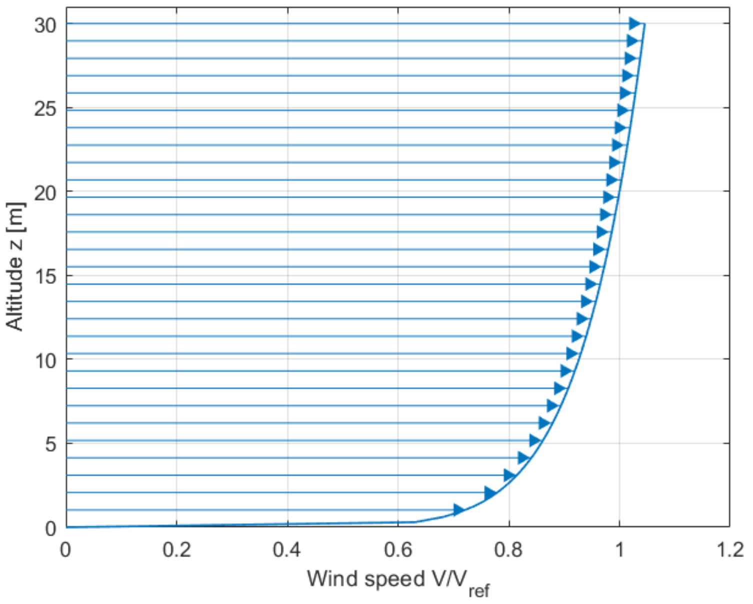

Figure 5.2: Boundary Layer Wind Profile

5.2.3. Downdraft behind the hangar

Next to free stream airflow effects, a more detailed model around the helicopter deck can be employed. In this way, the effects on the helicopter near the landing spot can be examined. Free stream airflow interacts with a bluff body such as a ship's superstructure, which results in a circulation zone behind the body. This means that the helicopter experiences a downdraft near the landing spot, effectively increasing the workload and power required. This large scale effect can be modelled with the understanding of CFD simulations. Previous research found that the mean induced vertical airflow velocity has a value of around $-0.1 \leq \frac{w}{U_\infty} \leq -0.2$, with U_∞ being the undisturbed relative airflow perceived at the top of the hangar, as can be seen from Figure 5.3a [19]. Another effect of the superstructure is a velocity deficit in the ship airwake (Figure 5.3b), which could result in a total airflow speed of 60-70% of the undisturbed flow.

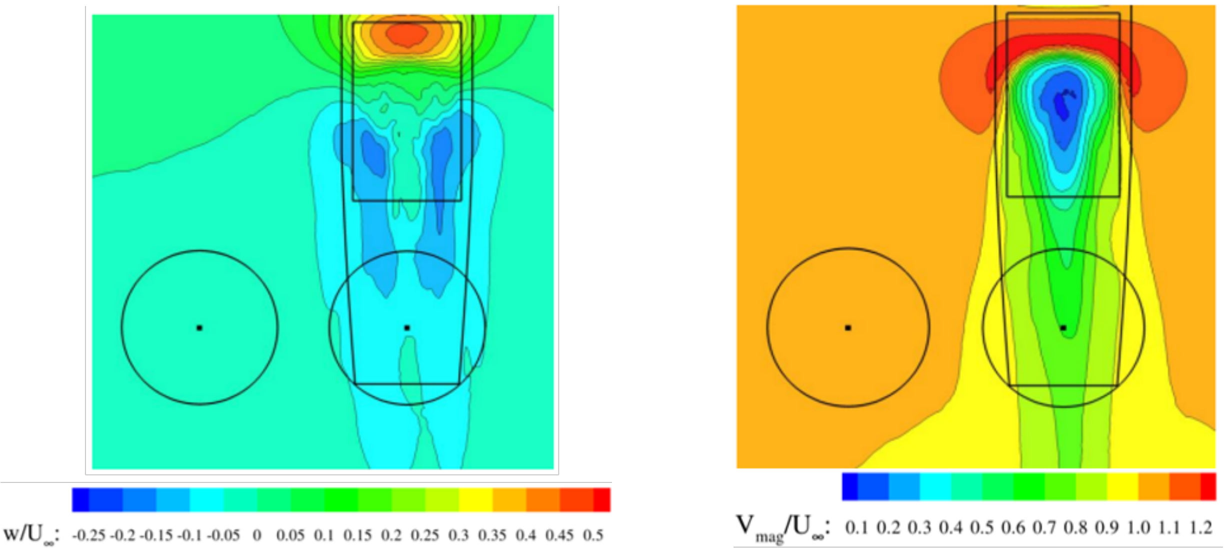

(a) Normalized mean vertical velocity

(b) Normalized mean velocity magnitude

Figure 5.3: Normalized velocity contours for a headwind derived from CFD simulations [19]

The circulation zone can be accurately modelled using experimental wind tunnel data. Tominaga and Shirzadi examined the flow around high-rise buildings to improve conditions for pedestrians [80]. This experimental dataset is shown in Figure 5.4a. The data surrounded by the red box can be used to model the flow behind a ship's hangar by manipulating the origin and magnitude of the vortex. The mean vertical velocity was measured by a free stream velocity of $U_\infty = 3.1\,\mathrm{m/s}$. The data is divided by this free stream velocity, multiplied with the desired downdraft strength and relative wind speed on top of the hangar and added to the total wind speed, which results in the airflow pattern as illustrated in Figure 5.4b.

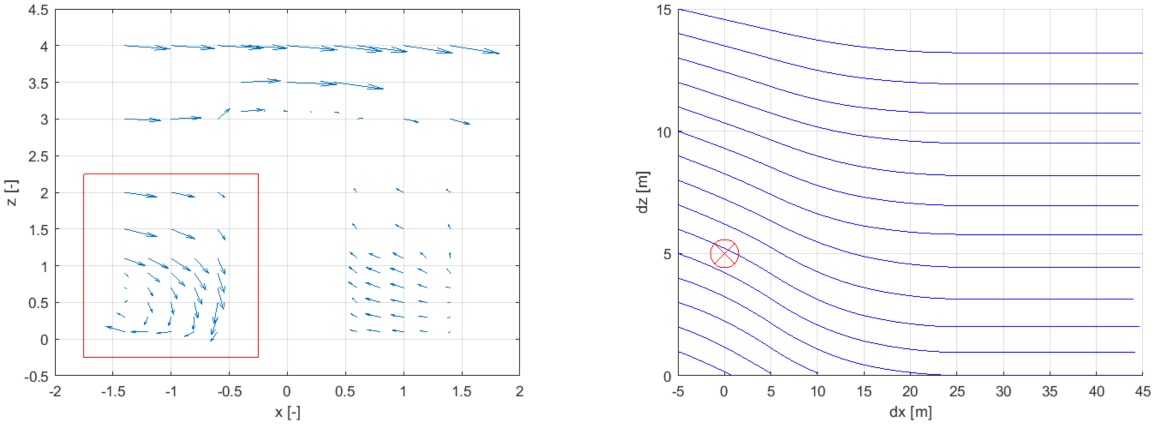

(a) Original experimental data of flow past a high-rise building [80]

(b) Streamlines of airflow at the helicopter deck, including downwash. The red marker indicates the final helicopter position before the landing manoeuver.

Figure 5.4: Original experimental data and modified data used for modelling the downdraft behind the ship's hangar

This downdraft model utilizes the relative airflow perceived at the hangar roof. The boundary layer wind model computes the wind velocity at the hangar height, which is then added to the ship's speed to obtain the relative airflow. After all, even if the wind velocity is 0 kts, the relative airflow is 16 kts (the ship's constant velocity), which already causes downdraft. This effect is mitigated when the relative velocity is zero, that is 16 kts tailwind. This line of experiments involves the wind conditions outlined in Table 5.2 for only the initial position 000°. First, two downdraft strengths (10% and 20% of the relative free stream flow) are assessed. Hereafter, the velocity deficit is added with a downdraft of 20% that starts 20 m behind the ship. In this way, both effects are isolated and can be interpreted separately. The velocity deficit is only applied to the horizontal component of the true wind speed and is modelled by a linear function that increases the deficit from 1 to 0.6 between 20 m to 10 m distance from the ship.

Table 5.2: Absolute and relative winds when the ship is sailing at 16 kts, simulated in the downdraft experiment

Real wind	Relative wind
South - 10 kts	Head - 6 kts
No wind - 0 kts	Head - 16 kts
North - 10 kts	Head - 26 kts
North - 20 kts	Head - 36 kts
North - 30 kts	Head - 46 kts

5.3. Weighting factor K_{t_f}

The final step for optimizing helicopter-ship approach trajectories in various wind conditions is to determine the objective function parameter K_{t_f}. This parameter prioritizes between time and control activity; the higher the parameter, the more important a fast trajectory becomes at the cost of possible higher control effort and vice versa. A sensitivity analysis method is employed to pick a proper value, after which the experiments can be executed. The analysis is first done by simulating helicopter trajectories with starting position 045°, without the presence of wind and with values $K_{t_f} = 10^n$ with $n = 0, -1, ... - 4$. An initial unbiased conclusion can be drawn by including an asymmetric starting position and excluding wind. The objective is to find a value that results in a smooth and predictable trajectory with low changes in thrust coefficient (minimal dC_T/dt).

Figure 5.5 shows both the optimized trajectories and normalized time histories of the thrust coefficient for the starting position 045°, without the presence of wind and for various values of K_{t_f} in the objective function. It can immediately be seen that $K_{t_f} = 10^0$ and $K_{t_f} = 10^{-1}$ provide unexpected behaviour. Instead of gradually descending, the helicopter dives and remains at z = 5 m altitude until its final position. This comes at the price of high control oscillations. The other trajectories are similar, the only difference is in the thrust coefficient; $K_{t_f} = 10^{-2}$ results in slightly more control effort.

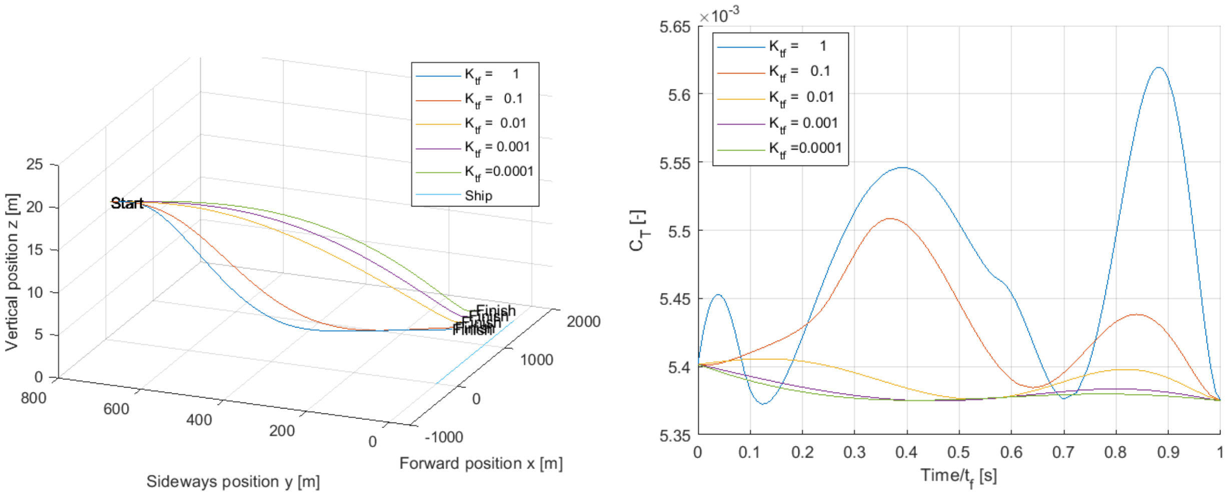

(a) Optimized trajectories

(b) Normalized time history of the total thrust coefficient

Figure 5.5: Optimized trajectory results for various values of K_{t_f}. Starting position 045°, without wind.

After discarding $K_{t_f} = 10^0$ and $K_{t_f} = 10^{-1}$, simulations were repeated with a 10 kts wind from the South (tailwind). The optimizer struggled with $K_{t_f} = 10^{-4}$. The optimized trajectory shows unexpected bumpy behaviour instead of a smooth path. The optimizer should be able to comply with wind conditions, thus this value is also discarded, leaving only $K_{t_f} = 10^{-2}$ and $K_{t_f} = 10^{-3}$. The trajectories and flying times are very similar, the latter differ approximately 20 s as can be seen from Table 5.3. The verdict comes from the thrust coefficient history, which shows higher values and greater derivatives for $K_{t_f} = 10^{-2}$ than $K_{t_f} = 10^{-3}$. This result is expected as control effort becomes more important the lower the weighting factor becomes. Ultimately, the optimizer should be able to handle a variety of wind speeds, directions, and models. It is expected that the power required also behaves smoothly when control efforts are minimised, which lowers the overall energy consumption. Taking this into account and considering the approximate 20 s time penalty, a weighting factor of $K_{t_f} = 10^{-3}$ was selected for the experiments. Intermediate values did not yield significant differences.

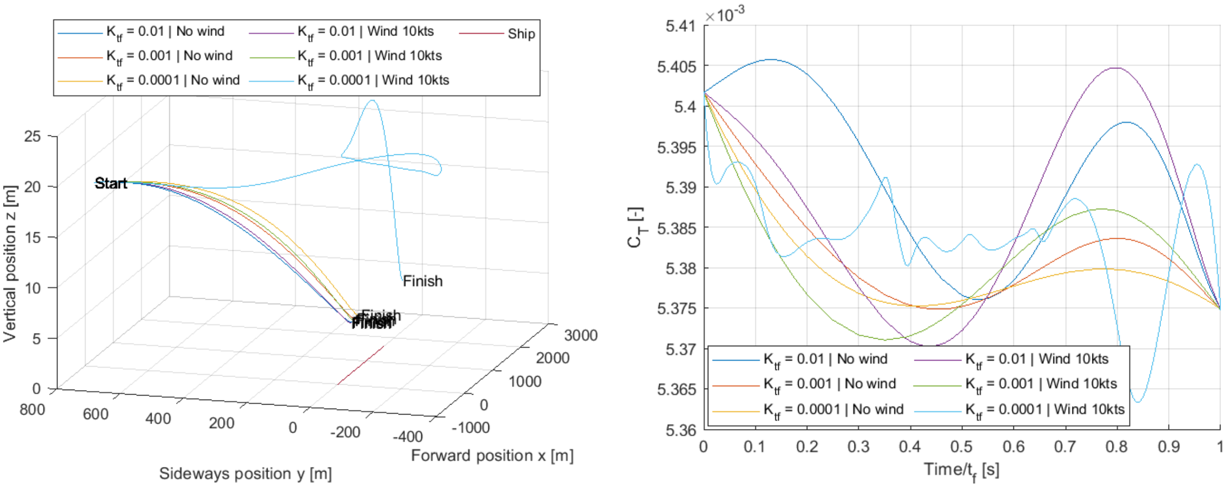

(a) Optimized trajectories **(b)** Normalized time history of the total thrust coefficient

Figure 5.6: Optimized trajectory results for various values of K_{t_f}. Starting position 045°, with a tailwind of 10 kts.

Table 5.3: Helicopter flying times in seconds for various values of K_{t_f}

K_{t_f}	**No wind**	**Tailwind** 10 kts
10^0	39.94	-
10^{-1}	46.21	-
10^{-2}	61.99	58.78
10^{-3}	81.04	74.53
10^{-4}	99.49	282.58

5.4. Post-Process Similarity Analysis

The experiments yield many approach manoeuvres for a range of wind conditions. To evaluate the effects of wind on optimized trajectories, approaches should be represented as a function of both wind direction and speed to instantly spot differences and interpret results at best. This can be achieved by giving each wind-affected trajectory a similarity score based on a reference case and visualizing this score on a polar graph, similar to a SHOL/SUOL. In this way, deviation trends as functions of wind direction and speed can be visualized when the reference cases are known. Regions where the wind does not affect the trajectory much can also be identified. This procedure reduces the amount of figures to a minimum and gives insight into the effects of wind on optimized approaches.

In the post-processing phase, the reference cases are the optimal approaches from all four starting positions without the presence of wind. These optimal approaches are geometrically compared to the wind-affected approaches of the corresponding helicopter starting positions. The approach does not have to be impractical if a wind-affected trajectory deviates from the baseline case, it only means that they are different. However, similarity scores might reveal trends as functions of wind direction and speed. When two trajectories are geometrically identical, the flying time and time histories of required power, thrust coefficient and other performance parameters are also highly similar. Subsequently, time histories of performance parameters differ when two trajectories deviate from each other, which might be due to increased engine demand or hitting a performance constraint. Therefore, the primary post-process method is based on a geometrical similarity analysis.

5.4.1. Definitions

Before diving into the similarity procedure, it is necessary to define some norms and notations. Firstly, the Euclidean distance and infinity norm are defined. Given a point p in three-dimensional space, $x(p)$, $y(p)$ and $z(p)$ can be used to denote the coordinates of this point. For two points p and q, the Euclidean distance D_2 and infinity norm D_∞ are defined as [81]:

$$D_2(p,q) = \sqrt{(x(p)-x(q))^2 + (y(p)-y(q))^2 + (z(p)-z(q))^2} \tag{5.3}$$

$$D_\infty(p,q) = \max\left(\left|(x(p)-x(q)\right|, \left|y(p)-y(q)\right|, \left|z(p)-z(q)\right|\right) \tag{5.4}$$

Next, the notation for constructing two trajectories is expressed as follows. Let A and B be two trajectories, respectively consisting of n and m timestamps. These trajectories can be written as:

$$\begin{aligned} A &= ((t_1, a_1), ..., (t_n, a_n)) \\ B &= ((t_1, b_1), ..., (t_m, b_m)) \end{aligned} \tag{5.5}$$

Where a_i, b_j are three-dimensional positions and t_i^a, t_j^b the corresponding timestamps.

5.4.2. Lock-Step Euclidean Distance (LSED)

A straightforward approach to quantify similarity is the Lock-Step Euclidean Distance (LSED), which measures the total distance between two trajectories by summing the spacing between individual points of the two paths. One limitation of this method is that it requires both trajectories to have the same length ($n = m$), necessitating interpolation between measurement points. The LSED between trajectories A and B is defined as:

$$LSED(A,B) = \sqrt{\sum_{i=1}^{n} D_2^2(a_i, b_i)} \tag{5.6}$$

An average distance between measurement points is used to accurately compare two sets of trajectories with different lengths, called the Lock-Step Euclidean Distance Normalized (LSEDN). This value takes into account the number of measurement points in a normalized form:

$$LSEDN(A,B) = \frac{1}{n}\sum_{i=1}^{n} D_2(a_i, b_i) \tag{5.7}$$

This procedure offers a quantified similarity measure between two trajectories. However, the method has some limitations. As stated above, the two trajectories need to be of equal lengths, which generally requires interpolation between measurement points. Moreover, the expression is most meaningful when sampling times are identical, that is if $t_i^a = t_i^b$ for all $1 \leq i \leq n = m$. If this is not the case, a more elaborate interpolation scheme could be implemented. In the post-process of this study, this is bypassed by normalizing time and only considering trajectories relative to the ship. Another limitation of this method is that the outcome does not provide significant value in directly understanding how much two trajectories resemble each other. Surely, the number and corresponding similarity are inversely proportional, but the value itself does not reveal a ratio of any kind.

5.4.3. Longest Common SubSequence (LCSS)

Another method to quantify the similarity between two trajectories is the Longest Common SubSequence (LCSS) [81]. This method was first employed to find analogies between character strings, but can be manipulated to be applicable for time series. The LCSS method is frequently utilized for noisy signal data and time series with different lengths, as the procedure is robust, can handle outliers and unmatched data points and is less computationally expensive than other similarity techniques [82]. Additionally, the algorithm normalizes the output to be between 0 (no similarity) and 1 (perfect resemblance), which provides a better intuition of the similarity between the two trajectories.

A visual representation of the LCSS method is shown in Figure 5.7, where the similarity is measured between a baseline path x (solid black line) and a route y (red dashed line). The algorithm depends on two tuning parameters ϵ and δ. ϵ defines the minimum bounding envelope; the maximum distance threshold between two trajectory points, and δ represents how far away these points may be within the data set. This last parameter allows for time stretching; positions close in space at different timestamps are considered to be a match if the time instants are also within range. If the algorithm can find points on both trajectories that comply with thresholds ϵ and δ, they are a match and are ultimately summed to the overall similarity.

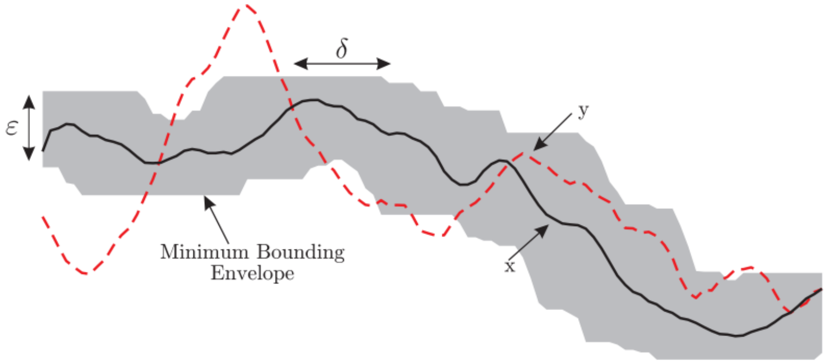

Figure 5.7: Longest Common SubSequence (LCSS) [83]

Although many extensions of this procedure exist, including derivatives or optimization schemes [82, 83], the standard version is implemented in this study. Pseudocode of the algorithm can be found in Appendix D and is based on a Bottom-Up Matrix formulation, as presented below^{Y}. Initially, this matrix has $(n+1) \times (m+1)$ entries with values starting from zero and can only be increased by finding matched points. The score of a path can be found on the diagonal, which is added by one if two points are similar and unchanged when there are not. The diagonal's last entry contains the total amount of matched points between the two trajectories.

$$LCSS(i,j) = \begin{cases} 0 & \text{if } i = 0 \text{ or } j = 0 \\ 1 + LCSS(i-1, j-1) & \text{if } D_\infty(a_i, b_j) \leq \epsilon \text{ and } |i-j| \leq \delta \\ \max(LCSS(i-1,j), LCSS(i,j-1)) & \text{otherwise} \end{cases} \tag{5.8}$$

The similarity function based on LCSS between trajectories A and B outputs a value between $0 \leq S(A,B) \leq 1$ and is defined as:

$$S(A,B) = \frac{LCSS(A,B)}{\min(n,m)} \tag{5.9}$$

The threshold parameters ϵ and δ are essential for the procedure and application dependent. This means that there is no generic method to tune these parameters. The LCSS similarity output was compared to the LSEDN results, and trajectory time histories were plotted to select appropriate values. In this procedure, total trajectories can be compared, but by excluding x, y or z coordinates from the infinity norm, horizontal or vertical paths can be compared as well. This means that the selection for ϵ is twofold, one value for the total and horizontal paths $\epsilon_{xyz} = \epsilon_{xy} = 16\,\mathrm{m}$ (equal to the ship's width) and a value for the vertical manoeuvres $\epsilon_z = 3.3\,\mathrm{m}$ (equal to the helicopter's main rotor diameter). It is believed that two locations closer than these thresholds are a match, considering the total length of the path and safety margins of the flight deck. In the post-process of this study, only geometrical tracks from the ship's perspective are considered. This means that time is normalized and only trajectories relative to the vessel are taken into account to mitigate the effect of flying time. As a result, the value of δ does not include a physical meaning, but it merely gets around unequal lengths and measurement point spacing. Previous research shows that results do not improve significantly when δ is more than 20-30% of the trajectory length [82]. Considering the mean trajectory lengths of this study, a value of $\delta = 30$ was chosen.

5.5. Summary

This chapter described the experiments conducted to answer the research questions, the utilized wind models, the approach of selecting the weighting factor K_{t_f} and the procedure of post-processing the optimized trajectories. In the experiments, the helicopter starts at four different positions in trimmed condition and flies at cruise speed, while the ship maintains 16 kts speed towards the North. The optimizer is then subjected to both a uniform and a boundary layer wind field, where the wind speed ranges from 0 kts to 40 kts with directions 000° to 315°. The last experiment involves a wind model that includes downdraft and a velocity deficit close to the hangar. The objective function weighting factor is selected to be $K_{t_f} = 10^{-3}$ due to path smoothness, predictable behaviour and minimal control effort and is not altered between experiments. The optimized trajectories are compared to each other through a similarity technique. The Longest Common SubSequence (LCSS) algorithm is used for measuring the similarity between two trajectories, for which the Lock-Step Euclidean Distance Normalized (LSEDN) was used to tune the algorithm.

6
Results

This chapter discusses the simulation results of the proposed experiments. First of all, trajectories initiated from four starting positions are optimized as the baseline no-wind scenario. These tracks are important as they form the basis of the similarity measures. Afterwards, results from the LCSS similarity measure are compared to the LSEDN to show the effectiveness of the algorithm. Subsequently, the main results of the uniform wind experiment are outlined, including similarity measures, constraint violations and maximum power levels obtained during the approach. Dissimilarities are investigated and the best starting locations according to the objective, total energy requirement and by distance normalized quantities are presented. The same is repeated for the boundary layer wind results, which contain comparisons with the uniform wind field. Afterwards, the effects of downdraft behind the hangar are illustrated for relative headwinds from position 000°. Every experiment section concludes with a brief summary outlining the main findings. The chapter finishes with a main summary as well.

6.1. Baseline scenario: No wind

The baseline scenario includes all four helicopter starting positions and excludes any form of wind used to compare all following wind-affected results. Figure 6.1 shows these corresponding optimal paths towards the moving ship. As can be seen, all four trajectories are predictably smooth and show gentle descents towards the final hover position above the flight deck. Furthermore, all paths tend to converge during the final approach, which is due to the final boundary constraints. Consequently, the trajectory of the starting position 135° deviates mostly as the helicopter needs to curve away from the ship to ultimately return to the final approach tube.

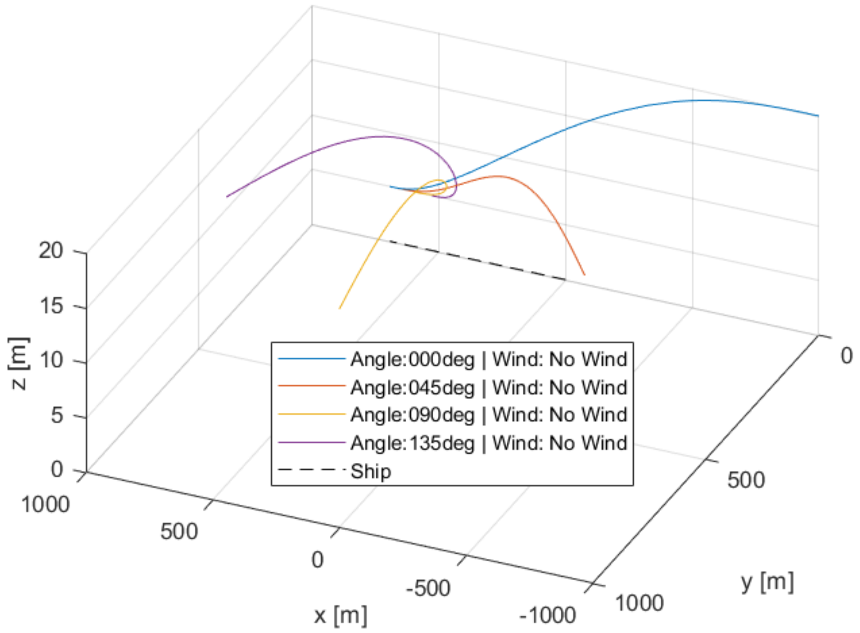

Figure 6.1: Optimized helicopter trajectories for the baseline scenario; all initial angles and without wind

The optimal approaches can also be seen from the ship's perspective, as depicted in Figure 6.2. Time is normalized to objectively assess the geometrical paths, where dx, dy, and dz represent the differences in forward, sideways, and vertical positions between the helicopter and the ship, respectively. These separated graphs are used for the similarity analysis in the preceding sections and can indicate clear trends between wind conditions or starting positions. For example, the pure descent phase is identical for all baseline scenario starting positions.

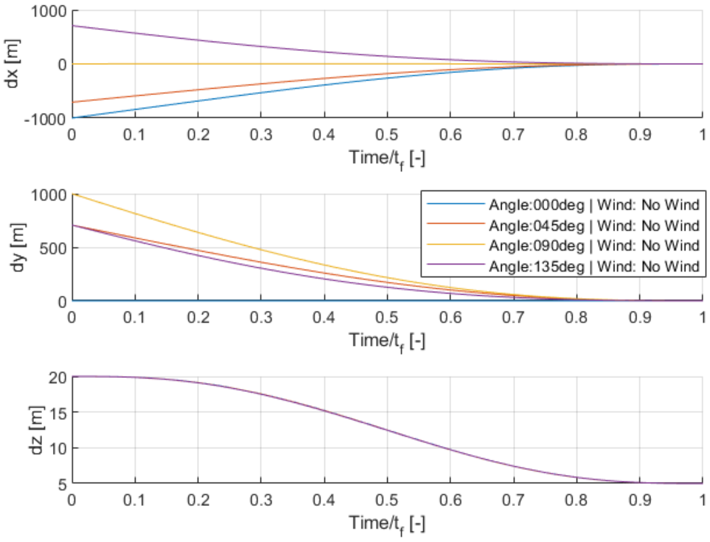

Figure 6.2: Optimized trajectories relative to the ship for the baseline scenario; all initial angles and without wind

Lastly, Figure 6.3 shows further path-related (left) and performance-related (right) parameters evaluated from the optimized baseline scenarios. Due to the lack of wind, the True-Airspeed V_{TAS} equals the ground speed in this case. Even though all starting positions are located at similar distances from the ship's initial location, helicopter starting positions with more negative x-values (behind the ship) are at a disadvantage. This is because they are further away from the final destination due to the vessel moving in the positive x-direction over time. Ultimately, these paths require more time, as indicated in Table 6.1. This effect is observable in the velocity V_{TAS}, flight path angle γ and disc angle of attack α_D graphs. Since the helicopter needs less time for the 135° starting position compared to the 000° location, these parameters change more abruptly. Moreover, the helicopter needs to decelerate faster to match the ship's speed when hovering above the flight deck. This causes some velocity undershoot for the 135° position, leading to more control effort and a higher power demand slightly before the final approach. Thus, while geometrical approaches in non-dimensional time may be similar, it does not imply that other path-related parameters are identical as well.

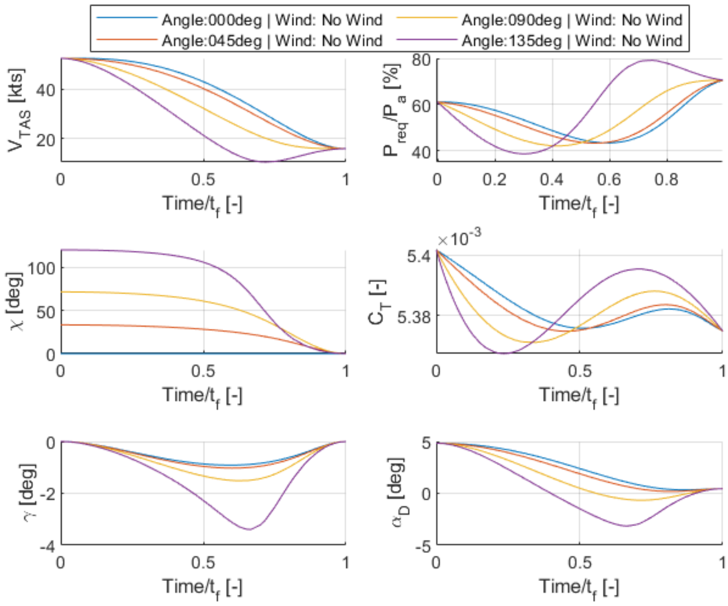

Figure 6.3: Trajectory and performance parameters for the baseline scenario

Table 6.1: Summary Optimization Baseline Scenario

Starting position	**Flying time [s]**	**Total distance [m]**
000°	84.3	1693.8
045°	81.0	1545.5
090°	72.9	1166.4
135°	64.0	730.0

6.2. Similarity measure

First, a geometric path comparison is presented where the Longest Common SubSequence (LCSS) algorithm is evaluated next to the Lock-Step Euclidean Distance Normalized (LSEDN). This correlation is illustrated in Figure 6.4 and provides both insight into the LCSS outcomes and a way to read the charts. The results are given in contour polar charts, where the radial and tangential coordinates represent the direction of where the wind is coming from in degrees (0°, 90°, 180° and 270° are respectively N, E, S and W) and the wind speed in kts, respectively. The graph's white midpoint marks the baseline no wind condition and the background colour indicates the value of the presented measure, as displayed in the colour bar on the right. Intermediate values are interpolated using the closest measurement points. Note that the similarity measures do not necessarily represent unfeasible trajectories, but are merely a means to ease comparisons as the baseline scenario characteristics are known.

Figure 6.4 shows the results from the LSEDN (left) and LCSS algorithm (right) for the first helicopter starting position (000°) in a uniform wind field. To ease comparisons and to maintain similar colours, the LSEDN is given a minus sign. Two areas can be distinguished from the LSEDN: winds from NW/N/NE with speeds higher than 20 kts in green/blue and others in yellow. The latter group contains mean distance values ranging from 0 m to 100 m, which itself also includes sublevels of similarity, but cannot be differentiated due to the high values for strong headwinds. These sublevels can only be separated when distance ranges are small, limiting this similarity measure significantly. The LCSS results are displayed on the right-hand side where multiple regions can be observed: the LSEDN regions mentioned, Easterly and Westerly winds with speeds from 20 kts and winds from the NW/N/NE with slower wind speeds than those identified from the LSEDN results. The LCSS algorithm identifies trajectory similarities better and generates an intuitive similarity number. Therefore, the LCSS algorithm (right) is employed as the geometrical trajectory similarity measure.

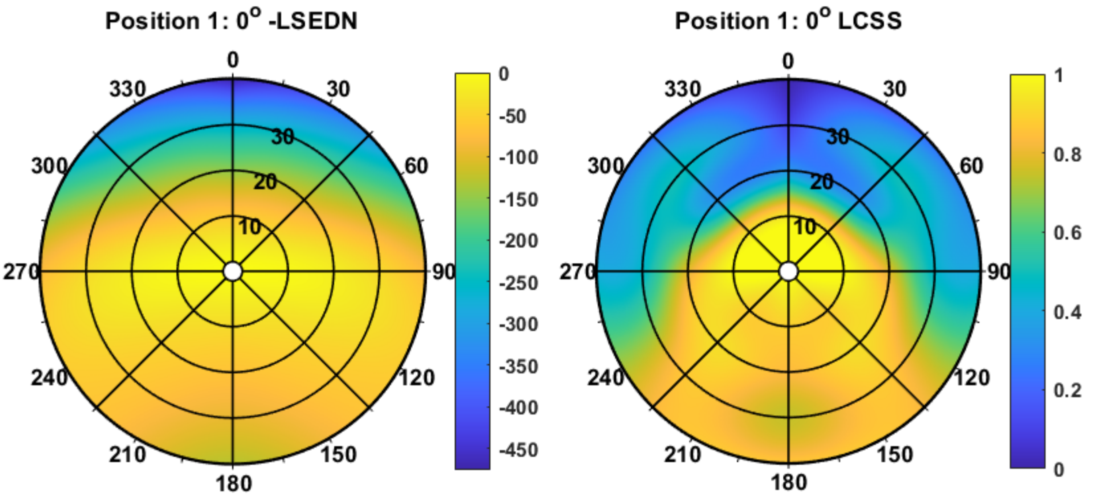
Position 1: 0° -LSEDN

Position 1: 0° LCSS

Figure 6.4: Lock-Step Euclidean Distance Normalized (LSEDN) and Longest Common SubSequence (LCSS) geometric similarity measures of optimized trajectories in a uniform wind field compared to no wind conditions for starting position 000°

Figure 6.5 provides trajectories from three initial locations with high, medium and low similarity compared to the baseline tracks to give an impression of how to interpret the LCSS output. The dashed lines represent the baseline tracks, while the coloured lines represent the optimized trajectories for winds from the South-West with 40 kts. The similarity values of the two tracks are shown at the initial locations and correspond to the values in Figure 6.6. First of all, the path from position one (right) only deviates slightly at the end due to a lower flying time. However, the paths relative to the ship are highly similar and are therefore given a high similarity value. The trajectories from position four (left) have comparable shapes. Still, the distance between the two exceeds the maximum distance provided by the parameter ϵ in the LCSS algorithm, resulting in a moderate similarity value. A low similarity score is given to the tracks from position two (middle) because their shapes and distances do not match at all. The similarity is not zero merely because the initial location is a match.

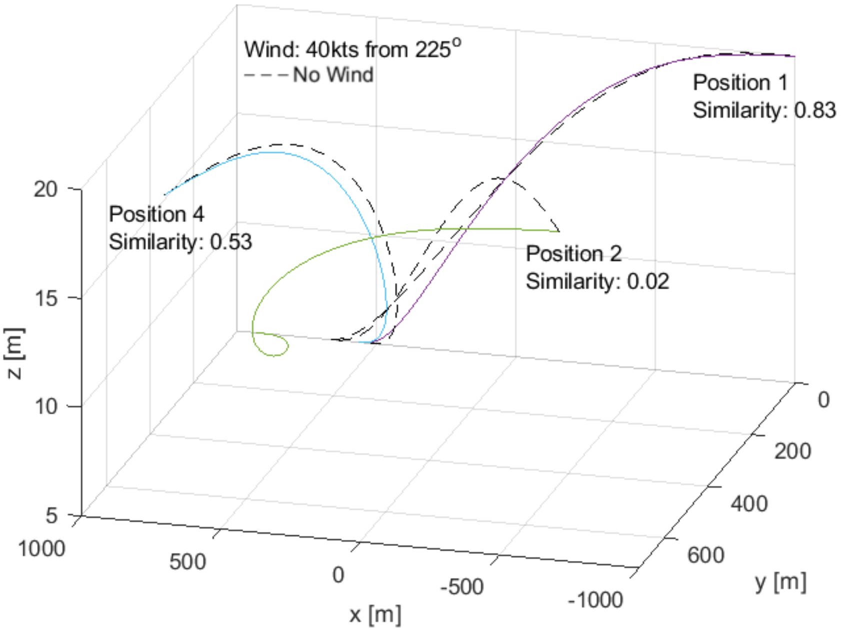

Figure 6.5: Trajectories from initial locations 000° (position 1), 045° (position 2) and 135° (position 4), optimized for no wind and uniform mwind from 225° with 40 kts. Their similarities compared to the baseline no wind track are given for each trajectory.

6.3. Uniform wind

This section discusses the results of optimized helicopter-ship approaches, affected by a uniform wind field. First, a general overview is provided, showing the total similarity to the baseline tracks, constraint violations and indications for the maximum power required during the approach. Afterwards, similarity measures for horizontal and vertical paths are compared to the baseline tracks, where deviations can be observed easily. The most eye-catching discrepancies (maximum power demands, NoGoZone constraint violations, ship's crosswinds and tailwinds during the approach) are investigated on a deeper level. Furthermore, objective function and integrated power values are compared between the four starting locations to find the best initial position to fly the approach in a certain wind scenario. The section ends with a summary, which includes the main conclusions of the uniform wind results.

6.3.1. Main results

Figure 6.6 displays the main similarity of optimized trajectories in uniform wind fields compared to the baseline no wind scenario for all four starting positions. Next to this, coloured markers indicate levels of similar power consumption, active constraints and non-converged solutions. The latter only involves constraint violations as all collocation defects are within the specified limits. A triangle depicts a reached constraint within error bounds, meaning that the constraint is active in at least one point, but the trajectory is still feasible. A red star indicates a constraint violation and thus an infeasible trajectory. The most significant observations are stated below per position. In the next section, geometrical correlation measures are separated between horizontal and vertical paths to identify the key differences between trajectories. Again, trajectories with low similarity scores are not necessarily problematic but give insight into patterns as a function of wind direction and speed.

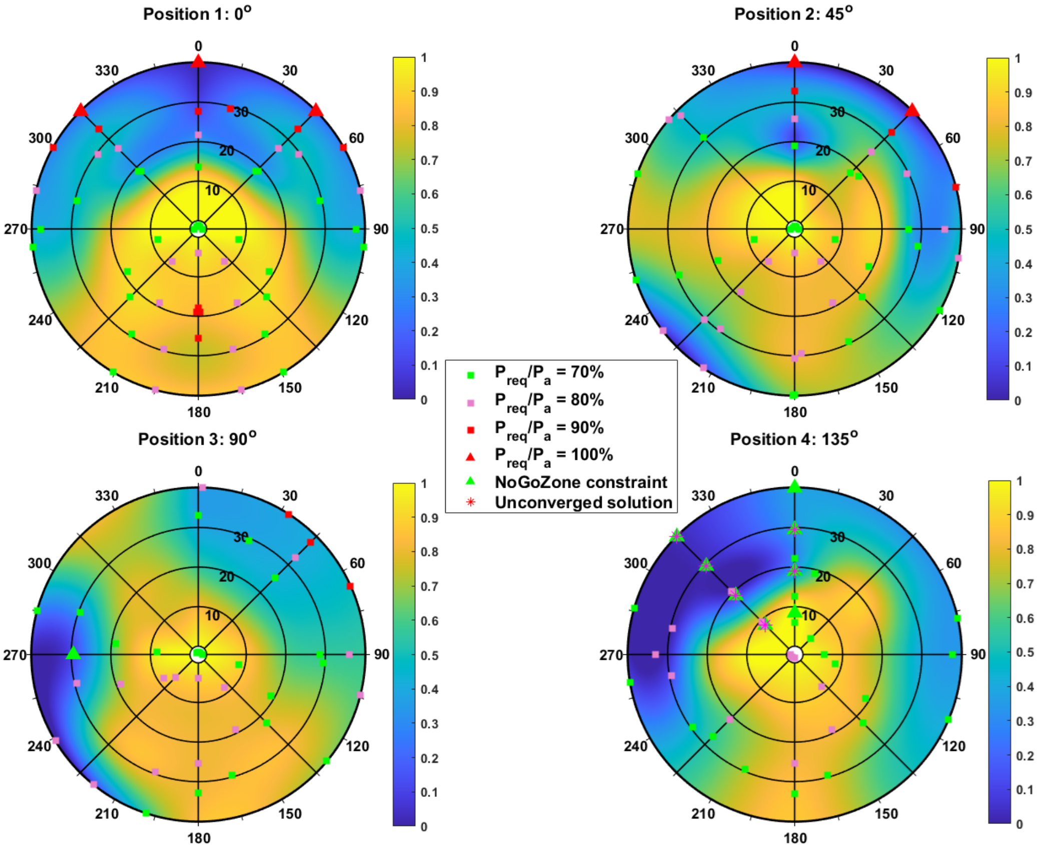

Figure 6.6: LCSS similarity measure of optimized trajectories in uniform wind fields compared to the baseline no wind condition. Several markers indicate power consumption levels, active constraints and unconverged solutions.

Position 1: 000°

Three regions of similarity can be identified for this position; high similarity for low wind speeds (less than 15 kts) and winds from the SW/S/SE (tailwinds); medium similarity for winds from the NW/W and NE/E (side/quarterly winds) with moderate to high wind speeds; and low similarity for winds from the North (headwinds) and NW/NE winds with 40 kts. Power consumption rises for Southerly winds with moderate speeds (20 kts to 30 kts) and winds from the NW/N/NE, ultimately reaching the limit for 40 kts winds from the NW/N/NE. This is due to the bucket shape of the power curve. Furthermore, two regions of interesting behaviour can be identified: a small region (180°,30 kts) of lower similarity and an oscillating pattern in the top part. The first is due to a variance in point density, where mesh points of the windy trajectory are distributed differently than other paths, causing the algorithm to match fewer points. The oscillations originate from numerical approximations. A clear trend can be seen when following the lines of experimental points, but intermediate regions may differ due to interpolation.

Position 2: 045°

The second position's similarity graph is rotated 45°, similar to the rotation of the starting positions, and slightly adjusted compared to the first position. Therefore, similar regions can be distinguished. Most notable are the regions of low similarity for strong winds from the SW (tailwind) and from the N/NE/E, where the first two involve the maximum allowable power consumption. Similar to the first position, a section of lower similarity can be observed (000°,20 kts), which is due to the distribution of mesh points. However, the power consumption does not reach 90% for trajectories in Southerly winds.

Position 3: 090°

Again, the result for the third position can be obtained by rotating the second position's graph and slightly modifying it. Unlike the second figure, three distinct regions are visible: low similarity for strong W/SW winds (tailwinds), medium similarity for medium to strong winds from the N/NE/E (headwinds) and high similarity in between. For the 40 kts winds from the NE, the helicopter requires 90% of its available power during the approach, meaning that the power limit has not been reached. However, the NoGoZone constraint is reached for the wind condition 270°, 30 kts. From in-depth observations, the constraint value is zero for this condition, but close to zero for a 40 kts wind speed from this angle, meaning that this limit is reached as well.

Position 4: 135°

Lastly, the figure for position four shows several oddities. Three similarity regions can be marked: low scores for W/NW winds (tailwinds) with moderate to high speeds, high similarity for winds from the South and low wind speeds, and medium similarity for the remaining directions. Similar to the preceding position, the maximum power does not reach 90%, but the NoGoZone constraint is reached and violated for many conditions. Another notable finding is that the optimizer failed to converge within the specified requirements for most of these NoGoZone violation wind cases.

Commonalities

Transcending the individual positions, several observations can be made regarding low similarity values for all initial positions. Firstly, a strong Northerly wind (ship's headwind) leads to lower correlation values, which might be caused by the power restrictions for the first two positions. Furthermore, initial tailwind directions (180° for position one, 225° for position two, etc) show lower similarity scores. This is true for all positions except the first, where this phenomenon is reflected in the increase in power consumption. Lastly, the ship's crosswinds result in medium similarity values for all positions.

6.3.2. Geometric similarity with baseline

A deeper similarity comparison is made in Figure 6.7, where the similarity measure is split between the horizontal xy-plane and the vertical z-axis, respectively on the left and right for each initial helicopter position. Only triangular markers for the reached constraints and red stars for violations are shown in these graphs. It can be concluded that similarity values for total and horizontal paths are comparable, since the threshold values for these cases are equal. This results in similar observations as above. However, vertical manoeuvres are shorter and have different threshold values, resulting in other patterns. Vertical paths show high similarity for most wind conditions, except for some cases showing medium similarity.

Strong NW/N/NE winds display dissimilarities for the vertical movements of position one, which align with the maximum power demands. The bubble of lower similarity is more pronounced here, which is due to grid density discrepancies. This bubble is also visible for the vertical path of position two for a SW wind of 30 kts. Additionally, lower similarities result from strong N/NE winds, which align with the maximum power demand, and strong SW winds, which are the tailwinds during the approach. Position three only shows an orange region for strong winds from the SW, which has a tailwind contribution during the approach. Similarly, position four displays orange regions for strong approach tailwinds. This NW wind coincides with the NoGoZone constraint violations.

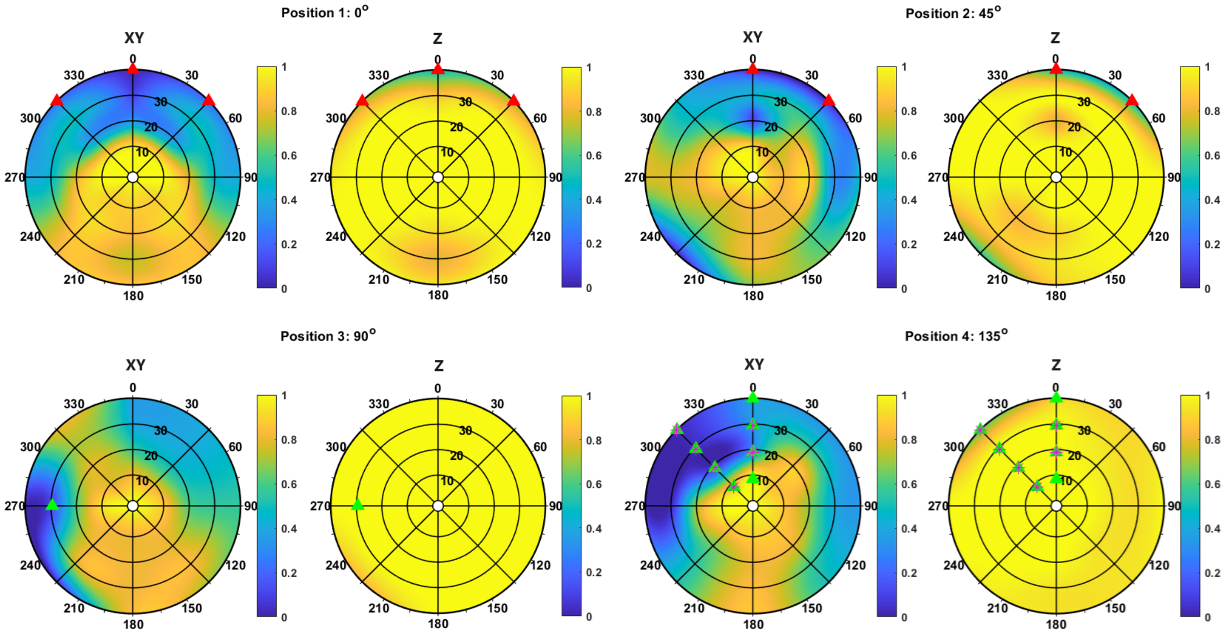

Figure 6.7: LCSS similarity measure of optimized trajectories in uniform wind fields compared to the baseline no wind condition. For each starting position, the similarity in the horizontal xy-plane (left) and vertical z-axis are displayed. Red and green markers indicate maximum power and NoGoZone constraint violations, respectively.

6.3.3. Anomalies

Reaching the maximum power

Geometric dissimilarities are observed from the previous figures, which need to be assessed further. Firstly, the Northern winds of positions 000° and 045° result in the maximum power required during the approach. Figure 6.8 shows both the trajectories relative to the ship and other geometrical and performance parameters resulting from Northerly winds of several strengths when the helicopter starts behind the ship. It can be seen that the maximum power is utilized for a great part of the approach with high wind speed. Since the helicopter starts the approach with the same airspeed as other wind scenarios, its ground speed is the lowest. Therefore, the helicopter needs to accelerate more to peer with the other wind scenarios' fast approaches. When the power limit restricts further acceleration, another way to gain velocity needs to be found. This is acquired by exchanging potential and kinetic energy; the helicopter performs an accelerated climb and uses the altitude in a dive towards the vessel to gain the necessary velocity. As this manoeuvre lowers the flight time, it penalizes the control effort. This behaviour is also applicable to other wind scenarios where the power constraint is reached. The dissimilarities in the horizontal plane result from the ground velocity shortage at the start of the approach. Due to the strong ship's headwind, the ground velocity decreases with wind speed as the initial airspeed is constant. This causes the helicopter to 'lag behind', which becomes worse with headwind strength. The latter applies to all starting positions.

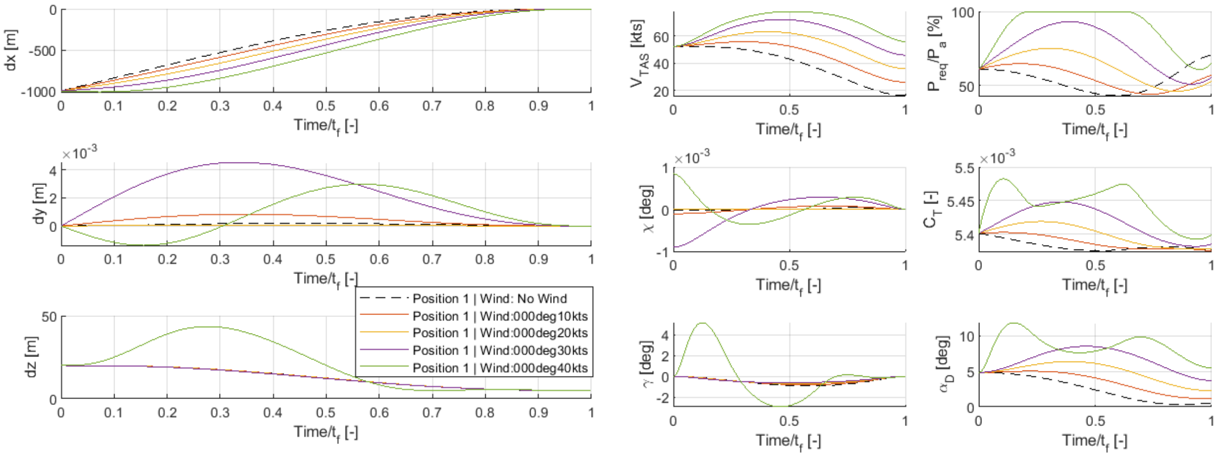

(a) Trajectories relative to the ship

(b) Geometrical and performance parameters

Figure 6.8: Optimized helicopter trajectories for initial position 000°, winds from 000° and wind speeds ranging from 0 kts to 40 kts

NoGoZone constraint violations

Optimized paths for positions three and four result in NoGoZone constraint violations, meaning that the helicopter would collide with the ship during the approach. Figure 6.9 shows a clear trend for Westerly winds up to a wind speed of 20 kts when the aircraft starts the approach from position three (090°). The helicopter uses the tailwind during the approach to limit the total flight time, subsequently lowering the total airspeed and increasing the power consumption. However, the aircraft struggles with higher wind speeds as it is unable to decelerate sufficiently close to the ship, resulting in drastically changed trajectories. The helicopter does not start with a similar heading angle, nor is the approach itself smooth. The approach for 30 kts involves a sharp rearwards manoeuvre to decelerate and a strong downward movement, while the helicopter flies in the opposite direction of the ship for a 40 kts wind. Both paths are impractical to implement in a flight controller and are not expected from the ship's perspective. Furthermore, the disc angle of attack reaches over $-7°$ during the deceleration, which might violate vehicle limits for backwards flying.

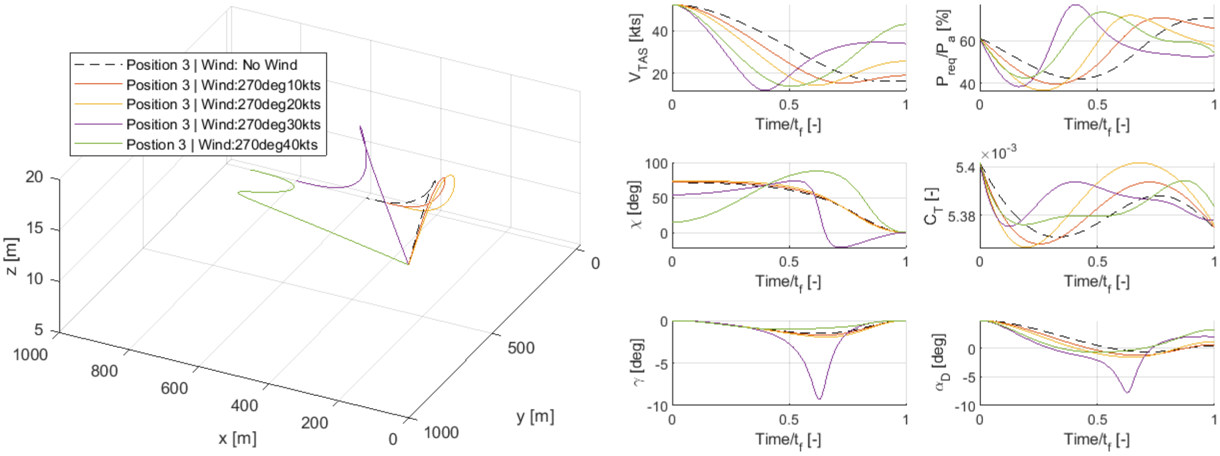

(a) Trajectories relative to the ship

(b) Geometrical and performance parameters

Figure 6.9: Optimized helicopter trajectories for initial position 090°, winds from 270° and wind speeds ranging from 0 kts to 40 kts

Helicopter starting position four (135°) also results in NoGoZone violations and even unconverged optimization runs for winds from the North and North-West. Figure 6.10 depicts these routes, where the paths for a wind speed of 10 kts are comparable to the no wind condition, but all others are not. Again, the main issue is the aircraft's deceleration when it comes close to the ship. Approaches in Northerly winds (left) result in odd behaviour, as the helicopter uses the wind to increase its ground speed but struggles to decelerate close to the vessel. As a result, the aircraft flies away from the ship to come back and approach it again from behind where bank angles rise to 14° to 18° compared to 3.5° for the no wind condition during the tight turn, which are within the permitted limits. The maximum power required for these trajectories is observed for the no wind condition (around 79%), which leaves a higher power surplus for the wind-affected paths. Although these results are unlawful with collocation constraints and more practical ways exist, these tracks could be used as a starting point if a slower approach is granted.

Winds from the North-West for this starting position are unworkable with increasing wind speed (right of Figure 6.10). Similarly, a wind speed of 10 kts is analogous to the no wind condition. However, since the helicopter starts ahead of the ship, it utilizes the wind to gain a higher ground speed, which becomes more problematic for higher wind speeds. The aircraft flies around the ship's front, banks up till 19° and simultaneously descends to the deck. Only when the wind speed is increased to 40 kts, the approach is more gradual and does not involve flying over the ship. The latter might become dangerous in rough weather or during the deployment of weaponry. Thus, it is impractical to utilize these approaches for high wind speeds. All NoGoZone constraint violations could be prevented if minimizing flight time was less important for the helicopter. In that way, the aircraft would have less urge to increase its ground speed, fewer struggles to decelerate and match the ship's velocity and fly a smoother and more practical approach.

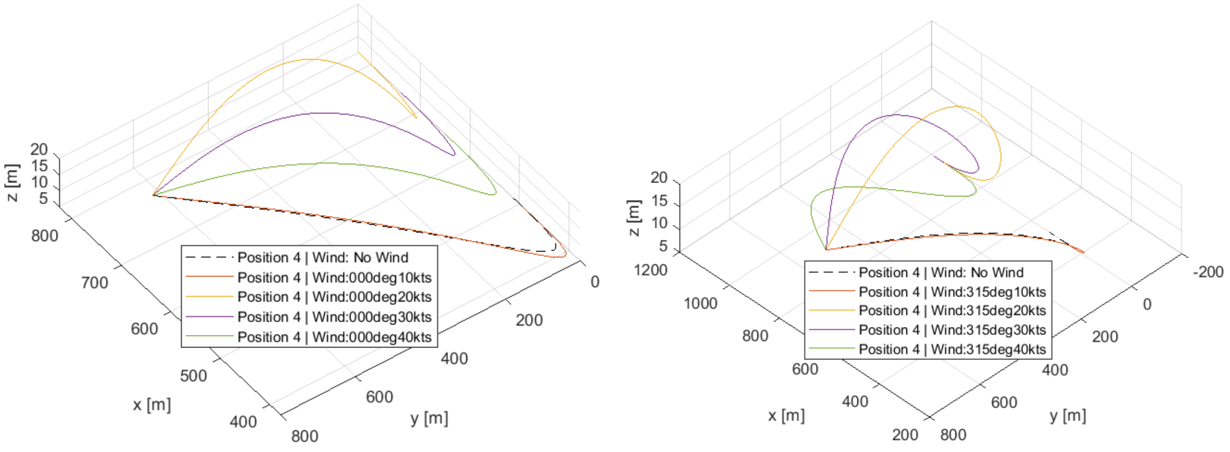

(a) Optimized paths for Northerly winds

(b) Optimized paths for winds from the North-West

Figure 6.10: Optimized helicopter trajectories for initial position 135°, winds from 000° and 315°, and wind speeds ranging from 0 kts to 40 kts

Ship's crosswinds

The ship's crosswinds have regions of lower similarity for all horizontal paths, but do not affect the vertical path much. Therefore, only the horizontal movements resulting from Easterly winds are depicted in Figure 6.11. The wind's influence is observable as the trajectories are moved to the direction the wind is blowing in, so for Easterly winds all paths are shifted to the West. Position one uses the crosswind to initially gain velocity and to decelerate during the final approach. This small penalty in control effort pays off in less flying time. Positions two and three divert the optimal path to the North with increasing wind speed to have a lower headwind component during the approach, lowering the maximum power consumption, total flight time and control effort in the final approach compared to flying the no wind trajectory. Position four benefits from the greater headwind component, as it already suffered from a velocity surplus. The track's heading is more to the East, resulting in a smoother approach and gradual deceleration towards the ship. Although the windy trajectories deviate from the no-wind paths, none are infeasible or impractical. In fact, a greater ship's crosswind allows tracks from position four to be smoother and to facilitate velocity reduction. Note that this is only true for headwinds during the approach.

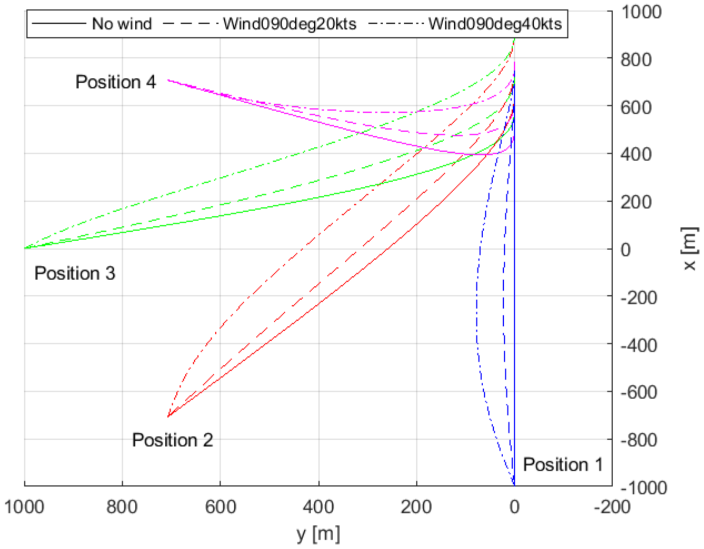

Figure 6.11: Optimized helicopter approaches for all initial positions, subjected to winds from 090°

Tailwinds

As identified from the similarity analysis, tailwinds during the approach result in different optimized paths compared to the scenario with no wind. Figure 6.12 shows the trajectories for all initial positions and their corresponding tailwinds. Although position one showed high similarity, it is included for completeness. The initial tailwinds for positions three and four are discussed earlier due to the NoGoZone violation. However, winds from 225° and 270° for these positions are also tailwinds with low similarity scores compared to the no-wind trajectory during the approach manoeuvre and are therefore added to the comparison. The figure shows significantly different tracks for high wind speeds than for moderate or no wind, except for the first position. The strong wind from behind increases the helicopter's ground speed, aggravating the deceleration in the ship's proximity. This results in a different trajectory where the aircraft uses extra distance to reduce its velocity to match the ship's ground speed. This behaviour is observed for positions two, three and four, where it also affects the vertical motion.

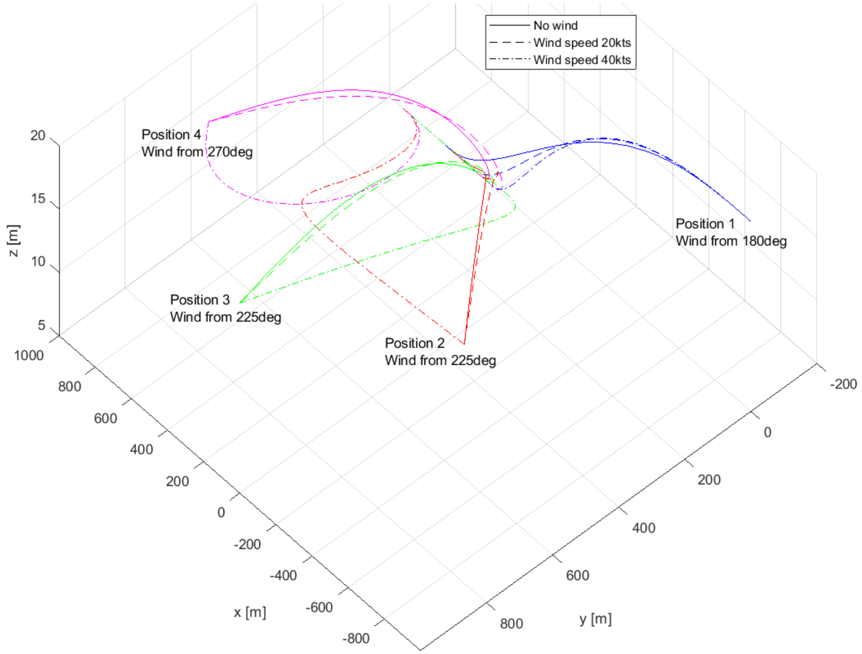

Figure 6.12: Optimized helicopter approaches for all initial positions, subjected to tailwinds during the approach

Another aspect is the decrease in airspeed near the ship. Strong winds from the SW/S/SE cause the airspeed to drop tremendously, resulting in the aircraft effectively flying backwards for tailwinds greater than the ship's speed. Because the airspeed is reduced to zero, the power consumption increases because of the bucket shape of the power curve. The airspeed heading angle, total airspeed and power consumption are depicted in Figure 6.13, where these phenomena are observable. The helicopter flies backwards faster with increased wind speed, which causes the power consumption to spike when the airspeed reaches zero. Although the decrease in power with an increase in airspeed after this moment is numerically correct, this does not represent a practical situation. In addition to the fact that helicopters are not built to fly backwards at such speeds, the tail clearance with the deck could be a limiting factor. In conclusion, strong tailwinds are not advisable, but hard guidelines cannot be determined yet since no limits are known for backward movements.

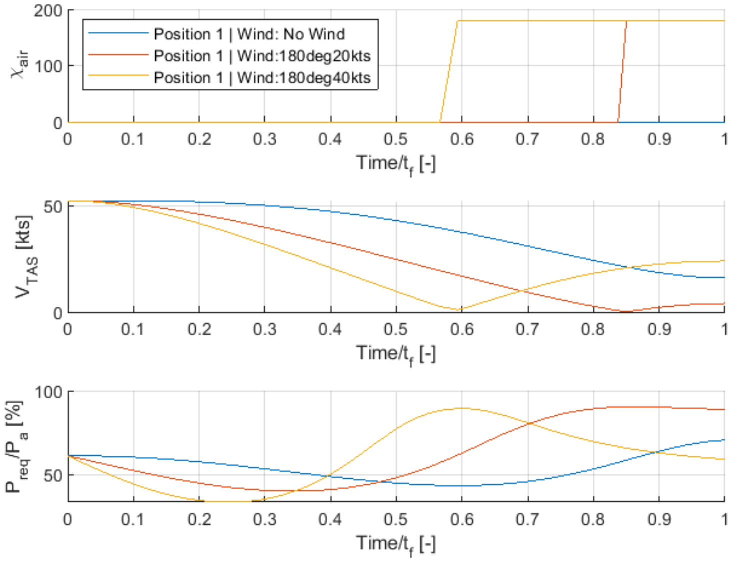

Figure 6.13: Tailwind performance parameters for starting position 000°

6.3.4. Best starting position

The previous sections assessed the practicality of optimized wind-affected trajectories of helicopter-ship approaches per initial position, but examining the problem with an inverse perspective also reveals meaningful insight and provides operational interest. Optimized tracks per helicopter starting position are compared for every wind condition to find the most optimal solution. Multiple definitions are explored because optimality can be defined in many ways depending on the situation. These are the lowest total objective function value, the lowest energy consumption for an approach, and these quantities divided by the total distance flown. The total objective function value incorporates the total flight time, which is generally higher for longer paths, disadvantaging position 000° compared to position 135°. Therefore, the total distance flown is involved to achieve a balanced evaluation. Paths that violate the NoGoZone constraint are excluded from the comparison.

Figure 6.14 shows the best starting positions per wind condition according to the total objective function value (left) and the total energy consumption during the approach (right), which is computed by integrating the power required along the flight path. The left graph shows some variety, which indicates that objective values are similar for multiple starting locations. Firstly, although commencing next to the ship scores best for all paths affected by a wind speed of 10 kts, values for other starting positions are highly similar, which means that the initial location does not matter much. Starting position 090° is preferred for winds from the north/northwest. This preference is not surprising, as these results also show the highest similarity with the no-wind condition. Similarly, winds from the NE/E prefer position 135°, mainly due to the lowest flight time and help in decelerating. A 40 kts Easterly wind shifts from position four to position one, but the difference in objective value is only 0.8 %. Winds from the South and South-West show a range of best initial locations, providing a slightly distorted picture. Objective values for 0 kts to 20 kts Southerly winds deviate less than 5%, but for higher wind speeds 090° is the best initial position. Similarly, location 000° is most consistent for South-Westerly winds and has objectives within 1% of the numerical best locations. Thus for operational purposes, it is best to start from location 135° for Easterly winds, 000° for winds from the South-East and South-West and 090° for Southerly winds.

Integrating the power required results in the total energy needed during the approach, which is relevant for low-running batteries, OEI conditions, emergencies, or rough weather where landings require much power. Figure 6.14 (right) shows the starting locations where the least amount of energy is required for each wind condition. Distinct regions are also noticeable in this graph, with minor shifts for high wind speeds. Location 045° is least favourable as it only scores best for strong Westerly winds. Low wind speeds prefer position 135°, mainly due to the lower flight time which decreases the total energy consumption. Northerly winds would also prefer this position if constraints were not violated. Location 000° beats 135° by merely 1.3% for strong Easterly winds, thus for practicality it is better to maintain location 135° for all wind speeds from this direction. The lowest total energy values for South-Westerly winds fluctuate between the several starting positions. Again for operational purposes, one location should be maintained: either 000° or 135°.

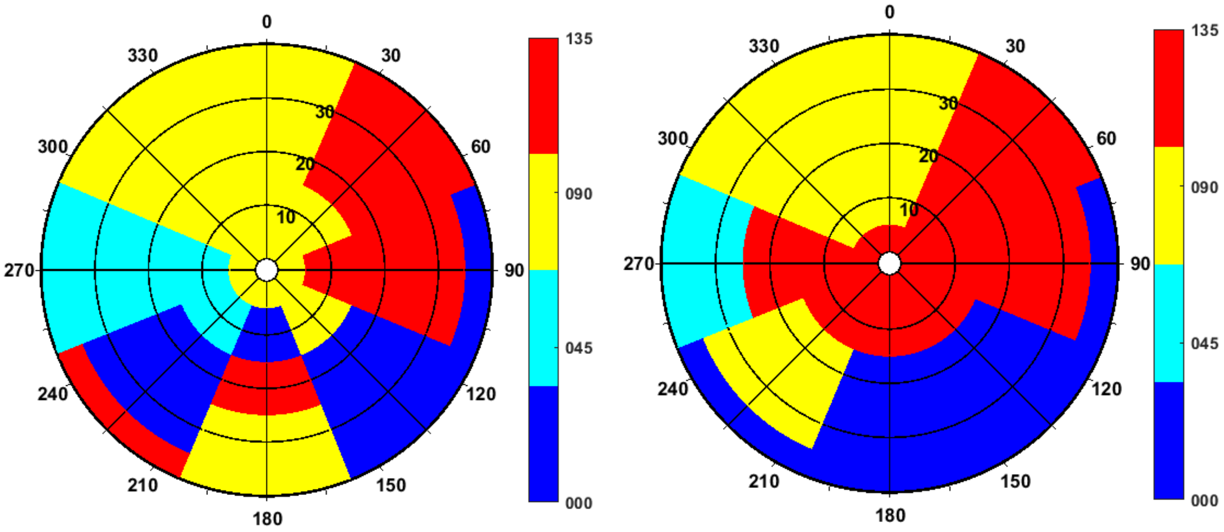

(a) Starting locations with the lowest objective function values **(b)** Starting locations with the lowest energy required

Figure 6.14: Best starting positions for helicopter approach trajectories in uniform winds according to the total objective function and integrated power

Normalizing the figures above with the total distance flown provides another perspective. Dividing the objective by the trajectory length results in the lowest time and control effort per unit distance, equivalent to the highest mean velocity for a smooth path. The integrated power required normalized by the path length equals the lowest energy consumption per unit distance. Most notable of these results depicted in Figure 6.15 is that the 135° location is not present. Generally speaking, positions 000° and 045° are preferable for the lowest objective value and lowest energy consumption per unit distance, respectively. For the lowest normalized objective, the preference for North-Westerly and Southerly winds gradually shifts from 000° to 045° and even 090° for strong winds from the South. From a practical standpoint, it would be best to maintain a single position per wind direction, which would be 045° for these winds.

The graph for the lowest energy per unit distance on the right depicts only three isolated regions. Location 000° is best for most wind directions and velocities. Although location 090° is best for strong Northerly winds, the maximum difference is only 1.1%. Therefore, it is advisable to maintain location 000° for all wind speeds from this direction. This is not the case for North-Easterly and Easterly winds, which deviate up to 30%. 10 kts winds from these directions are interchangeable with the proceeding best locations, but high velocities strongly prefer the indicated positions.

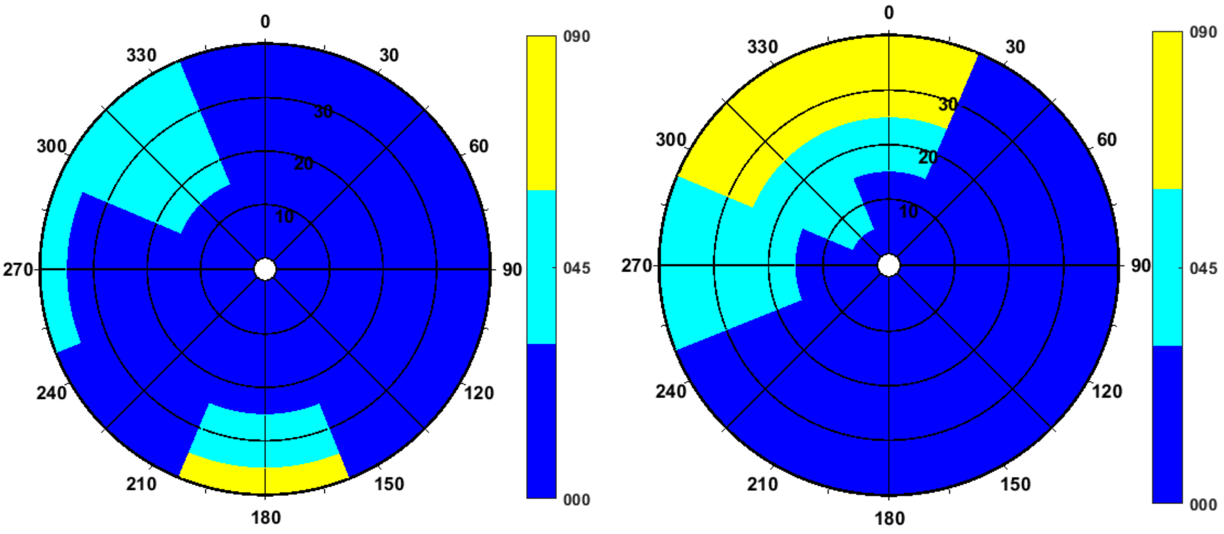

(a) Starting locations with the lowest objective function values divided by trajectory length

(b) Starting locations with the lowest energy required divided by trajectory length

Figure 6.15: Best starting positions for helicopter approach trajectories in uniform winds according to the total objective function and integrated power, normalized by the total distance flown

6.3.5. Summary uniform wind results

The results for optimized ship-helicopter approaches subjected to a uniform wind field with various directions and strengths are assessed in this section, from which some major conclusions can be drawn. Firstly, the baseline no-wind scenario resulted in smooth trajectories which are executable for ship-UAV approaches. All initial positions show maximum power peaks at the end of the trajectory where the airspeed is minimum, except for the 135° starting position. This is due to the relatively low distance to the ship and the high initial helicopter velocity. Furthermore, the similarity measure based on the Longest Common SubSequence (LCSS) is capable of detecting dissimilarities better than the Lock-Step Euclidean Distance Normalized (LSEDN) due to its range from zero to one. The technique can also measure multiple time series with an unequal amount of grid points. Hence, all similarity analyses were performed using the LCSS method.

Moreover, it has been shown that the initial helicopter position affects the optimized trajectories for every wind condition. The similarity graph for another starting location can roughly be found by rotating the 000°-graph by its respected relative degree. Positions one and two suffer most from the ship's headwinds due to reaching the power limit. In these scenarios, the helicopter initially gains altitude to convert the potential energy into kinetic energy in the final approach. The ship's headwind also increases power consumption for position 090°, but not as much. Therefore, it is more beneficial to approach the vessel from the side when dealing with strong Northerly winds. The ship's crosswinds altered the optimized paths in such a way that the aircraft used the extra ground speed for positions 000° and 045°, or was helped by decelerating in positions 090° and 135°. Tailwinds, either during the approach or relative to the ship, can be problematic due to low airspeeds, increased power consumption and tail clearance with the flight deck. For positions 090° and 135°, the NoGoZone constraint was violated because the helicopter did not have enough distance to decelerate properly. Location 135° suffered from many unconverged solutions for winds from the North and North-West.

The results were also examined from an opposite perspective to find the best helicopter starting location per wind condition. This was done by comparing the objective function values and integrated power required for each starting position. Additionally, these quantities were normalized by the total trajectory length to assess these quantities per unit distance. The best starting locations did not show resemblance with the no-wind similarity graphs, meaning that deviations from the baseline paths could gain benefits. Northerly winds demonstrated similarity between best positions according to the objective function and integrated power. However, Southerly winds fluctuate in the preferred initial location, mostly due to numerical deviations. For practical reasons, it is advisable to maintain a consistent starting location per wind direction as wind speeds can fluctuate and might be inaccurate due to measurement errors. The best starting locations based on the by-distance-normalized quantities yielded different perspectives. Both generally prefer approaches from behind, except for some wind directions.

6.4. Boundary layer wind

The higher-fidelity boundary layer wind model is more realistic and provides more insight into vertical manoeuvres in optimized wind-affected trajectories. This section dives into the results of this wind model extension by assessing the similarity measures compared to the baseline no-wind trajectories per starting location. Additionally, the most optimal starting locations per wind conditions are presented and the boundary layer wind results are compared to the uniform wind tracks to quantify the impact of the wind gradient.

6.4.1. Main results

The boundary layer wind field's main results are shown in Figure 6.16, visualizing the similarity between wind-affected trajectories and the baseline tracks for the four initial helicopter locations. Additionally, coloured markers denote maximum power consumption levels during the trajectory, constraint optima and unconverged solutions. The main outcomes show high consistency with the uniform wind results, and graphs for other positions can roughly be found by rotating the 000° results by their relative headings. In contrast, while the general overviews are equivalent, regions of high and low similarity are more distinct as fewer regions of moderate similarity are observed and NoGoZone constraints are violated more. The next sections mainly highlight the deviations from the uniform wind results to avoid repetition.

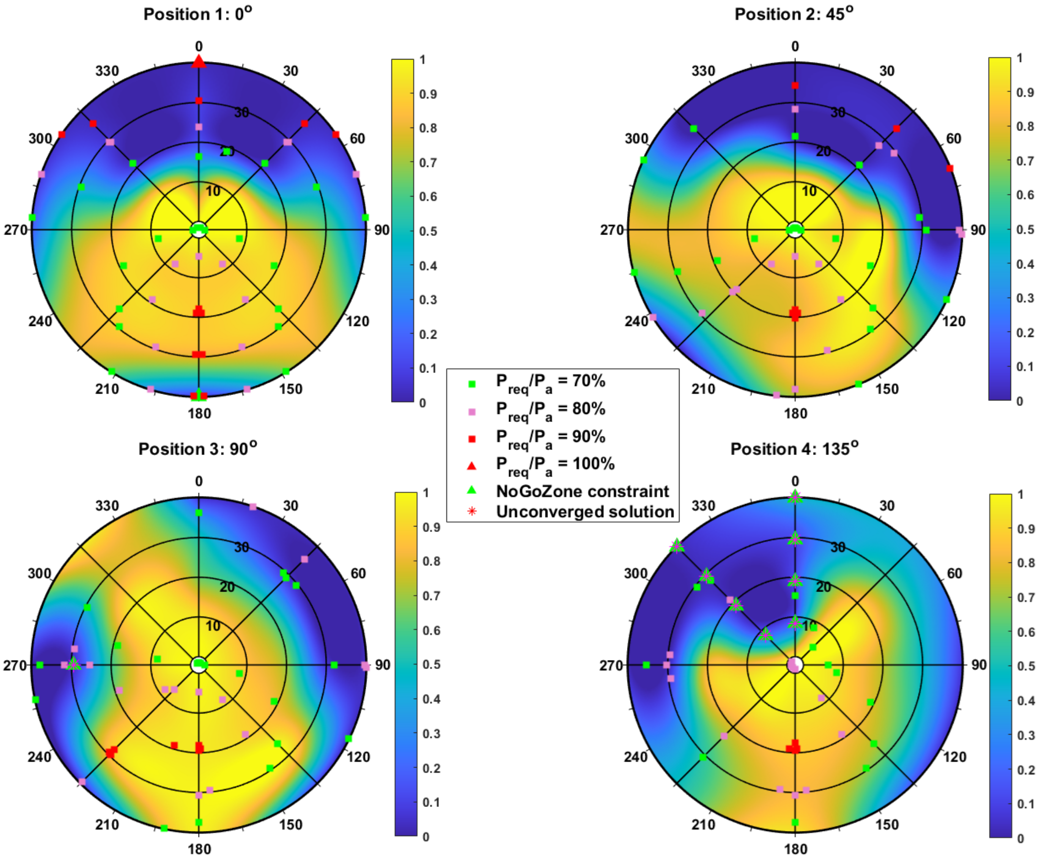

Figure 6.16: LCSS similarity measure of optimized trajectories in boundary layer wind fields compared to the baseline no wind condition. Several markers indicate power consumption levels, active constraints and unconverged solutions.

Position 1: 000°

Next to showing more distinct regions of high and low similarity, the key discrepancies with the uniform wind results are the maximum power required during a path and hitting constraints. For the boundary layer wind field, only the pure headwind with 40 kts speed invokes the maximum power required, while winds from the North-East and North-West demand up to 96% of the maximum power. Next to this, a 40 kts wind from the South violates the NoGoZone constraint, causing the similarity measure to drop from high to low. Lastly, lower wind speeds from the South result in higher power peaks than the uniform wind model.

Position 2: 045°

Two deviations from the uniform wind results can be observed for the 045° starting position. The first involves no power constraint violations for 40 kts winds from the North and North-East. Unfortunately, this is not the correct representation as the power peaks rise to 99.998% of the maximum power available for both wind directions. While the constraint is not violated numerically, it practically has reached the limit. The second deviation is the increase in power peak height for Southerly winds.

Position 3: 090°

The graph for location 090° is also highly comparable to the uniform wind results, except for the more distinct high-low similarity contrasts. Three major discrepancies are identified: a decrease in power peaks for strong North-Easterly winds, which do not reach 90% anymore; an increase in power peaks for mild winds from the South and South-West and a modified trend of the 80% power peak around the NoGoZone constraint violation, which is not only reached but also exceeded. Apparently, this wind condition causes problems for the optimizer as the 40 kts wind speed from this direction is within limits.

Position 4: 135°

The results of position 135° are most comparable with the uniform wind outcomes since this graph also shows moderate similarity with the baseline track for high wind speeds. However, two exceptions are noted, the first being the increase in power peaks for Southerly winds. Secondly, NoGoZone constraints are all violated for winds from the North and North-West with all speeds.

Commonalities

General wind observations can be made that are independent of the helicopter starting position. Firstly, strong headwinds (either the ship's or during the approach) do not require as much power as the uniform wind results dictate, since the helicopter acquires lower wind speeds by descending. This results in more wind conditions to fly with a power surplus. Secondly, tailwinds (either the ship's or during the approach) cause more trouble by elevating the power peak above 90% or increasing the risk of collisions due to constraint violations. Lastly, the ship's crosswinds still cause lower similarity compared to the baseline.

6.4.2. Anomalies

Reaching the maximum power

Figure 6.17 shows optimized trajectories started from position 000° that are affected by Northerly winds of several wind speeds with both the uniform and boundary layer wind models. Both trajectories relative to the ship and corresponding geometrical and performance parameters as functions of normalized time are visualized. Both wind models produce the same horizontal trajectories, but the vertical manoeuvre differs. In the boundary layer wind model, the helicopter acquires the lowest headwind by flying as low as possible and hitting the minimum safe altitude (MSA). This strategy decreases the total airspeed and required power and postpones reaching the upper limit. The helicopter ascends to 8 m near the end of the approach, after which it descends to its hover position. This manoeuvre increases the headwind strength and supports the deceleration of the helicopter to match the ship's speed. The wind gradient allows the helicopter to use its motor power more effectively, which results in a higher power surplus and lower flying times, at the cost of slightly more control effort. This scenario is similar to the strong Northerly winds of position 045°.

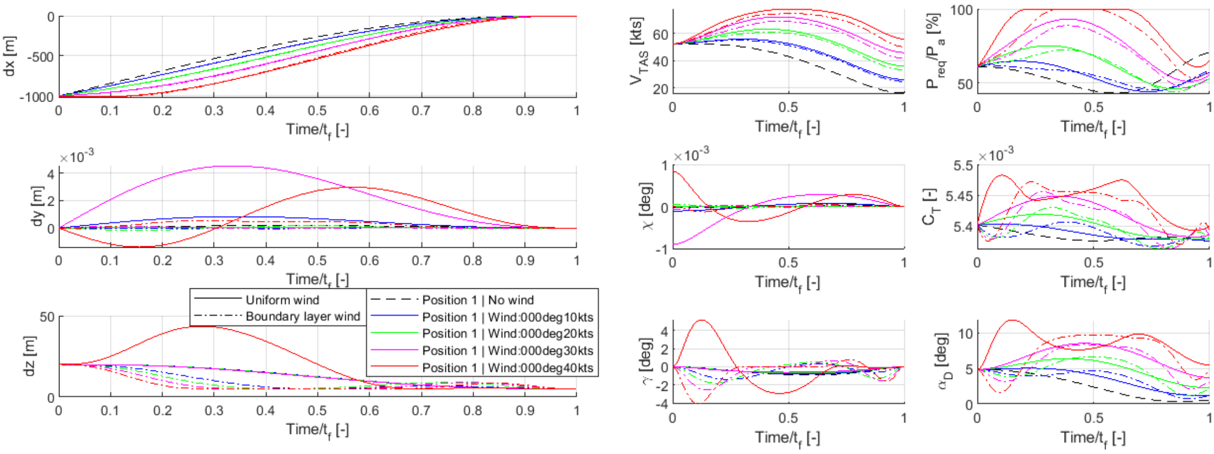

(a) Trajectories relative to the ship **(b)** Geometrical and performance parameters

Figure 6.17: Optimized helicopter trajectories for initial position 000°, winds from 000° and wind speeds ranging from 0 kts to 40 kts in uniform and boundary layer wind fields

NoGoZone constraint violations

Figure 6.18 shows optimized trajectories in uniform and boundary layer wind fields for positions 000° and 090°, affected by winds from the South and West, respectively. The graphs show anomalies between wind speeds and wind models where the NoGoZone constraint is reached. The first position suffers from the constraint of 40 kts Southerly winds, which are also its tailwinds during the approach and landing. The approaches for both wind models and wind speeds show similarities, where the boundary layer wind trajectories descend faster to acquire a lower ground speed. The optimizer experiences difficulties with the higher fidelity wind model due to the NoGoZone constraint as it outputs a trajectory with a substantially longer distance, deviating from the trend.

The right graph of Figure 6.18 shows approaches from location 090° affected by Westerly winds, which are the tailwinds during the approach. The uniform wind field resulted in constraint values of zero for wind speeds 30 and 40 kts. However, the boundary layer model violates the constraint for 30 kts but produces a feasible path for a higher wind speed. Still, the approaches deviate strongly from the lower wind speed paths and excite odd behaviour by initially climbing or flying alongside the ship before approaching it from the side. All in all, these tracks are more distant, require more time and control effort and are not predictable from the vessel's point of view.

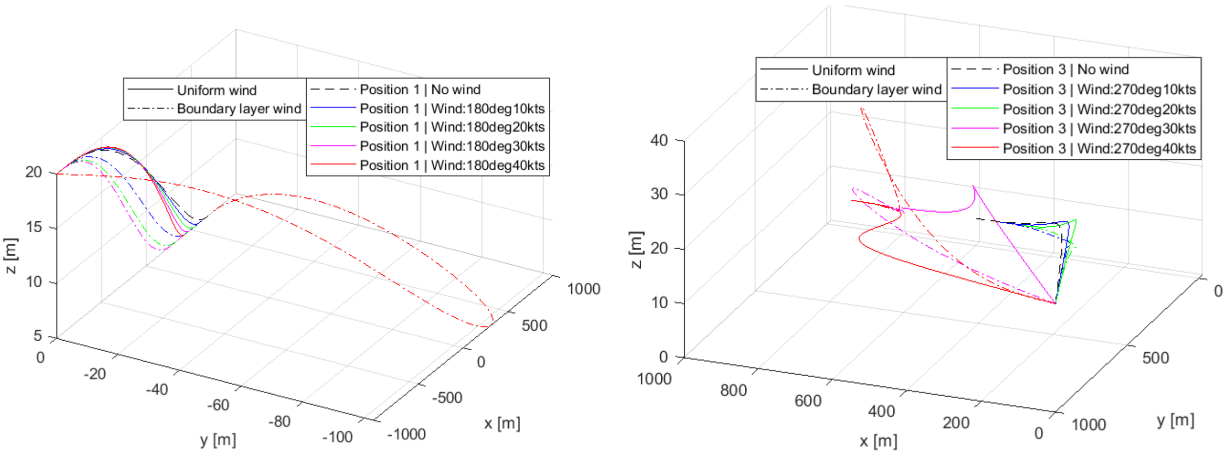

(a) Optimized trajectories from location 000° for Southerly winds **(b)** Optimized trajectories from location 090° for Westerly winds

Figure 6.18: Optimized helicopter trajectories for initial positions 000° and 090°, winds from 180° and 270° and wind speeds ranging from 0 kts to 40 kts in uniform and boundary layer wind fields

Two more scenarios violated the NoGoZone constraint: winds from the North and North-West for paths initiated from location 135°. These wind directions cause complications for both wind models, as depicted in Figure 6.19. The left graph shows results from Northerly winds, which show similar patterns for both wind speeds and wind models. Despite not being able to avoid a collision, the trajectories seem predictable and executable. The bottleneck is the high initial speed of the helicopter in combination with the low distance to the ship and the high tailwind speed. The aircraft cannot decelerate properly and is forced to fly away from the vessel to later approach it from behind.

The right graph of Figure 6.19 illustrates trajectories from position 135° with winds from the North-West, which are the tailwinds during the approach. Analogous to the left graph, all trajectories violate the NoGoZone constraint and are thus numerically infeasible. A low wind speed indicates similar behaviour to the baseline track, but higher wind speeds do not reveal a clear pattern. Moderate wind speeds prefer the helicopter to fly over the ship and approach it from the other side, while a 40 kts wind speed results in a straight-in approach where the boundary layer wind track initially ascents to acquire a lower flight time, despite the constraint violation. Parallel to the Northerly wind case, the main difficulty is the initial helicopter velocity combined with the low distance and high tailwind speed.

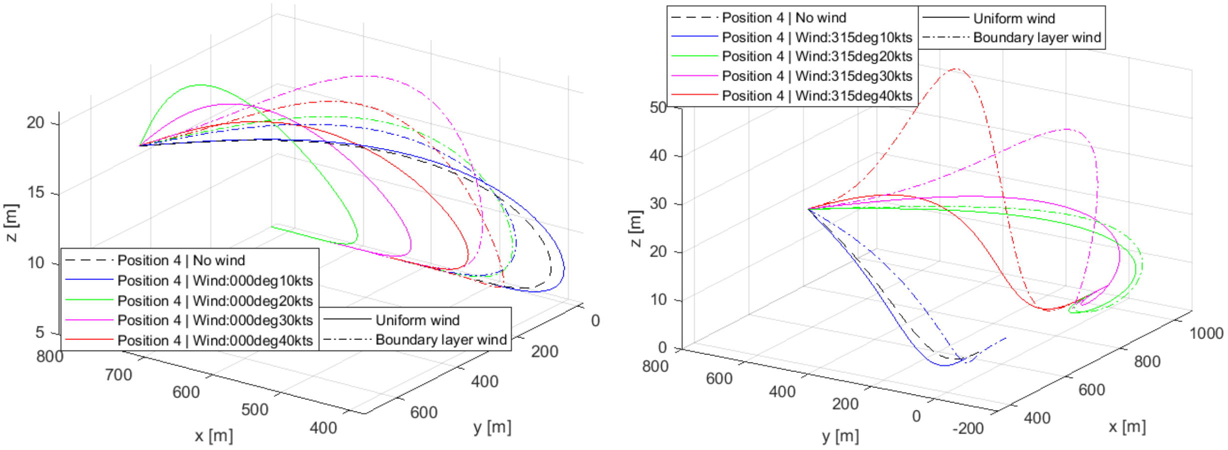

(a) Optimized trajectories for Northerly winds **(b)** Optimized trajectories for winds from the North-West

Figure 6.19: Optimized helicopter trajectories for initial position 135°, winds from 000° and 315° and wind speeds ranging from 0 kts to 40 kts in uniform and boundary layer wind fields

Ship's crosswinds

The ship's crosswinds with the boundary layer wind model result in similar horizontal trajectories as outlined in Figure 6.11. However, vertical paths differ due to the change in wind speed with altitude. An example is illustrated in Figure 6.20, where the ship's crosswind is exploited as a headwind. A low wind speed results in a gradual descent as the helicopter's airspeed decreases due to deceleration and less drag per altitude. In contrast, immediate descents are observed for higher wind speeds, with the helicopter gaining altitude towards the end of the approach. Higher wind speeds in this situation correspond to more headwind, slowing the helicopter down and deteriorating the objective. Instead, the aircraft exploits the wind gradient to have less drag in the initial approach phase, and more drag to decelerate towards the deck. This situation also applies to the other starting positions.

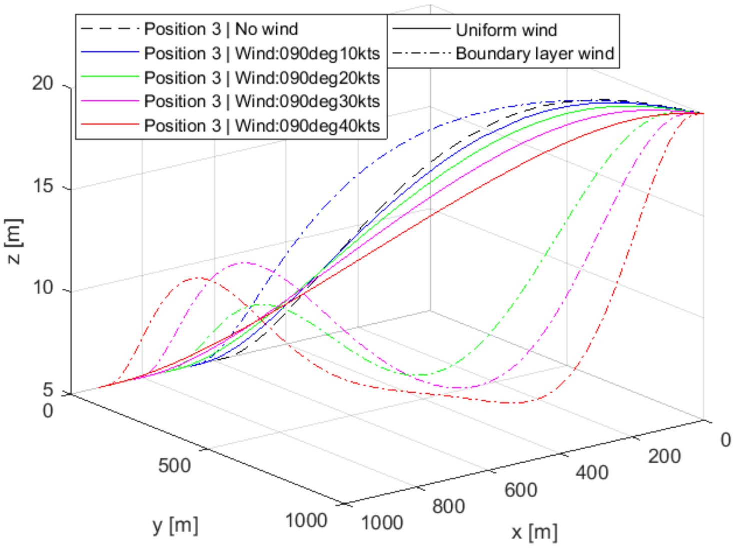

Figure 6.20: Optimized helicopter trajectories for initial position 090°, winds from 090° and wind speeds ranging from 0 kts to 40 kts in uniform and boundary layer wind fields

Tailwinds

Tailwinds during the approach trouble optimal trajectories towards the landing deck due to the increased ground speed. Even though the aircraft is allowed to change altitude to modify the effective wind speed, difficulties arise. This effect manifests itself in two ways: not being able to decelerate in time, thereby drastically changing its approach and/or colliding with the vessel; or increasing the power required drastically due to the low airspeeds and in some cases effectively flying backwards. These effects can already be observed from the similarity measure in Figure 6.16. Trajectories with NoGoZone constraint violations are depicted in Figure 6.18 and Figure 6.19.

The second aspect is the increased power peak during the approach due to a low airspeed. This phenomenon occurs for all initial positions affected by wind speeds of around 20 kts. This wind velocity results in an effective helicopter airspeed of around zero in combination with the ship's forward speed, which demands much power. For starting position 045°, this effect also occurs for a slightly higher 30 kts tailwind (from 225°) due to the cross component. Figure 6.21 illustrates the direction and magnitude of the helicopter's airspeed vector and the power required, expressed as a percentage of the maximum power available, as functions of normalized time. The graphs represent the results of starting location 000° with winds from 180° for both uniform and boundary layer wind fields but the parameters show similar behaviour for the other starting positions. By decelerating towards the ship's deck to match the vessel's speed, the helicopter's airspeed drops to zero and it starts to fly effectively backwards. The point of zero airspeed marks the power peak and moves to the start of the approach as the wind speed increases. Although the maximum power required reaches 90%, the disc angle of attack becomes negative after the point of zero airspeed, endangering backwards flying limits and tail clearance with the flight deck.

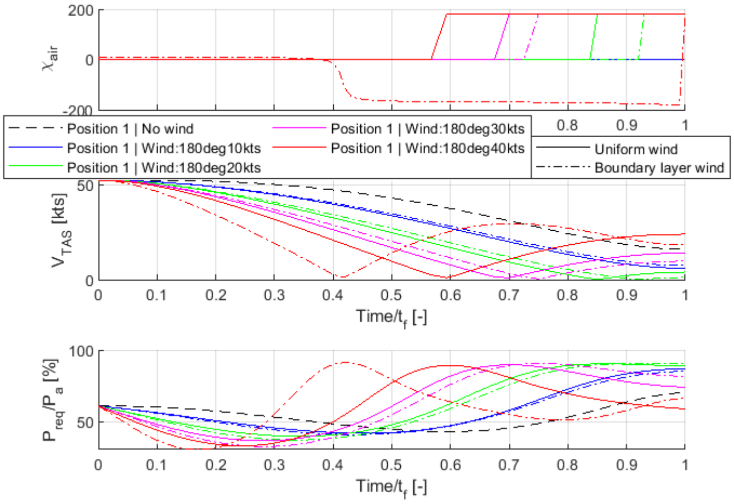

Figure 6.21: Tailwind performance parameters for starting position 000°

6.4.3. Best starting position

The best initial helicopter locations based on the objective function value and integrated power required as functions of wind direction and speed, according to the boundary layer wind model, are shown in Figure 6.22. As expected, the graphs are equivalent to the best starting positions derived from the uniform wind model, with only minor deviations. The optimal starting position based on the total objective function value depicts two differences: a shift from position 000° to 135° for a 40 kts wind from the East; and the switch from location 090° to 000°. These transformations are both in line with the explanation given in the best location section for uniform wind fields. The boundary layer wind results show more consistency with wind directions, despite Southerly winds which should be avoided anyway.

Additionally, optimal starting positions based on the integrated power required also demonstrate low predictability for Southern winds. It is advisable to omit the 090° region on the lower half of the graph and maintain locations 000° and 045° for Southerly and South-Westerly winds, respectively, as the maximum deviation is within 5%. The fluctuating locations indicate that energy levels between starting positions do not vary much. 40 kts Southerly winds shifted from 000° to 045° as the former exhibits the NoGoZone constraint violation that causes the path to curve away from the vessel, thereby increasing its total distance, flying time and thus the energy required.

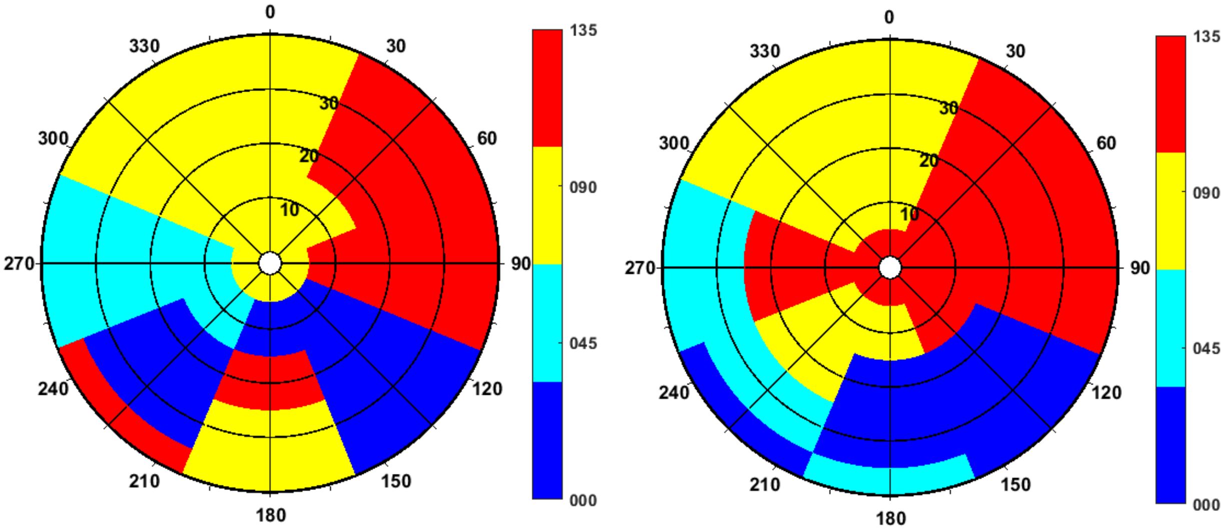

(a) Starting locations with the lowest objective function values

(b) Starting locations with the lowest energy required

Figure 6.22: Best starting positions for helicopter approach trajectories in boundary layer winds according to the total objective function and integrated power

Normalizing the total objective and integrated power results in the best starting locations as presented in Figure 6.23, indicating the lowest flying time and control effort per unit distance or highest mean velocity and lowest energy consumption per unit distance, respectively. The highest mean velocity for a smooth path (left graph) is identical to the uniform wind results. However, the lowest energy consumption per unit distance (right graph) deviates mildly. 40 kts Southerly winds and 10 kts Westerly winds shift from locations 000° to 045°. The former is due to the NoGoZone constraint violation for location 000°, where the extra energy consumption is higher than the extra distance flown. The latter deviates due to numerical approximations (0.07%). In conclusion, the best starting positions according to the lowest energy consumption per unit distance derived from the boundary layer model are also identical to the uniform wind results.

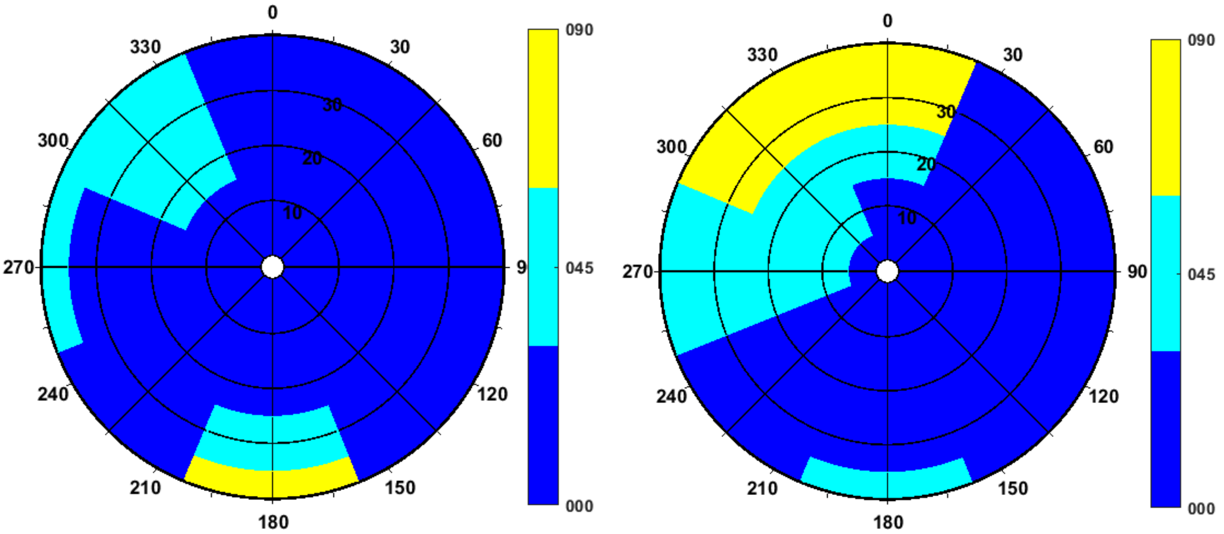

(a) Starting locations with the lowest objective function values divided by trajectory length

(b) Starting locations with the lowest energy required divided by trajectory length

Figure 6.23: Best starting positions for helicopter approach trajectories in boundary layer winds according to the total objective function and integrated power, normalized by the total distance flown

6.4.4. Comparison to uniform wind results

Although this section already addressed results from two wind models in individual cases, a more general comparison is made to assess the effect of wind model on the optimized approaches. Even though trajectories obtained from the two models are dissimilar from the baseline tracks, they can be similar to each other and conclusions can be drawn whether increased wind model fidelity is necessary. Therefore, the LCSS algorithm measured the similarities of optimized wind-affected trajectories of both wind models and its results per starting position are presented in Figure 6.24. A general observation is that all trajectories in low to mild wind velocities are comparable. This means that the geometric trajectories do not deviate significantly, indicating similar trends in performance parameters as well. Secondly, regions of high dissimilarity are observed for wind conditions that violate constraints using one or both wind models during the optimization process. For example, helicopter approaches in a uniform wind that experienced power constraint violations tend to ascent and exchange potential and kinetic energy, while the optimized approach in the boundary layer wind field behaved similarly to the other wind speeds. Furthermore, the optimizer tends to have significant difficulties with NoGoZone constraint violations as trajectories deviate strongly from the main trends and baseline tracks. All other medium or low similarity regions are mostly due to other vertical behaviour in which the helicopter descents smoother or exploits the wind gradient and/or flies an equivalent route, but with more distance than the threshold permits. In conclusion, the simple uniform wind model sketches practical trajectories, but the increased model fidelity is an asset to include the third dimension and gain more insight into helicopter-ship approaches in windy environments.

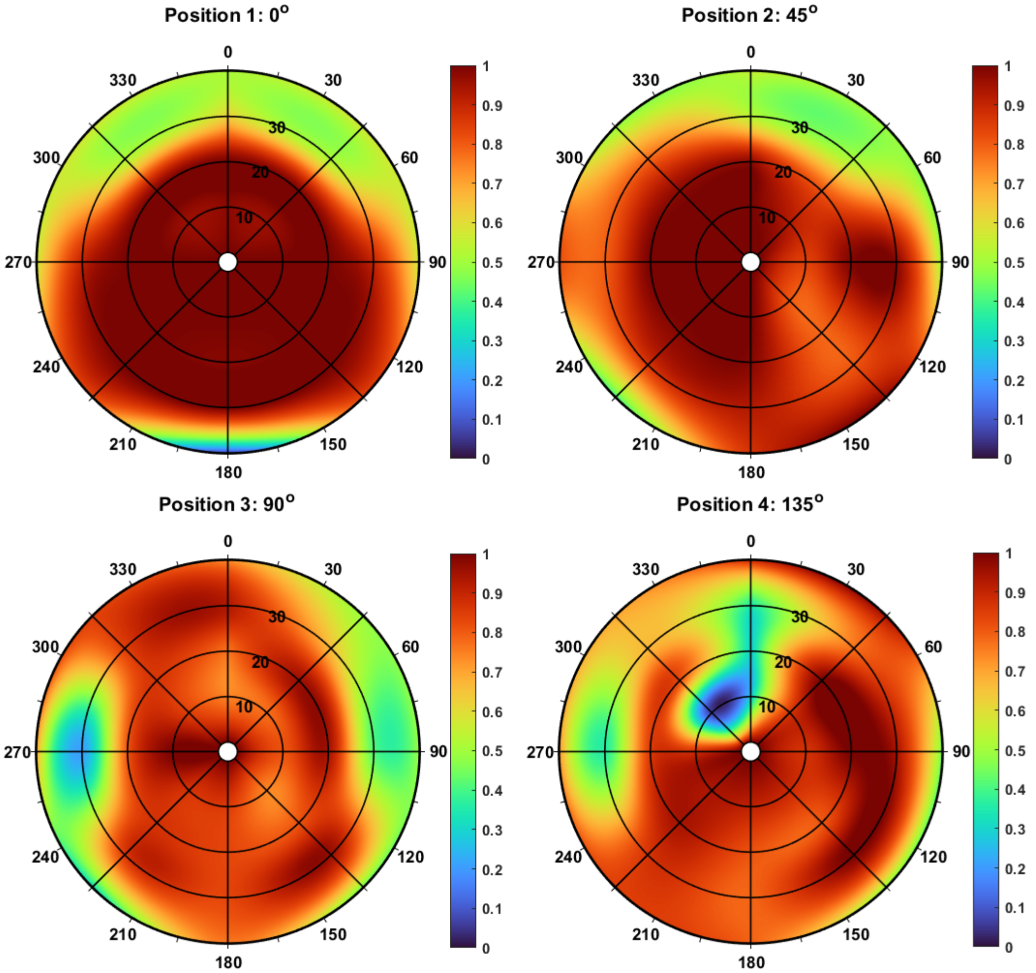

Position 1: 0°

Position 2: 45°

Position 3: 90°

Position 4: 135°

Figure 6.24: LCSS similarity measure of optimized trajectories in boundary layer wind fields compared to the uniform wind field results.

In addition to geometrical deviations, important conclusions can be drawn from performance parameters. This is done by comparing the values of the objective function and integrated power belonging to the best starting positions derived from uniform and boundary layer wind fields. Figure 6.25 shows two polar graphs that indicate the deviations of the best starting position values derived from the boundary layer wind field compared to the uniform wind field in percentages. Note that the colours do not represent similar values, but are merely a means to quantify differences. A positive percentage means a greater value for the uniform wind model compared to the boundary layer model and vice versa. The left graph illustrates insignificant deviations in objective function value, which are between -0.81% and 1.85%. Especially headwinds have higher objective function values for the uniform wind field as the helicopter acquires lower effective headwinds by descending in the boundary layer wind model. On the other hand, tailwinds result in lower objective values in the uniform wind field due to the higher ground speed.

The right graph depicts the integrated power required, or the total energy consumption, belonging to the best starting position. These differences are moderately between -7.57% and 8.26%. Again, low wind speeds expose mild differences between the two wind models, while the greatest deviations result from strong Northerly, Easterly, and Southerly winds. The helicopter exploits the wind gradient in the boundary layer wind model in these wind conditions, leading to lower energy consumption. A strong Southerly wind resulted in a NoGoZone constraint violation for the boundary layer wind model, which is why the uniform wind model obtained a lower total energy.

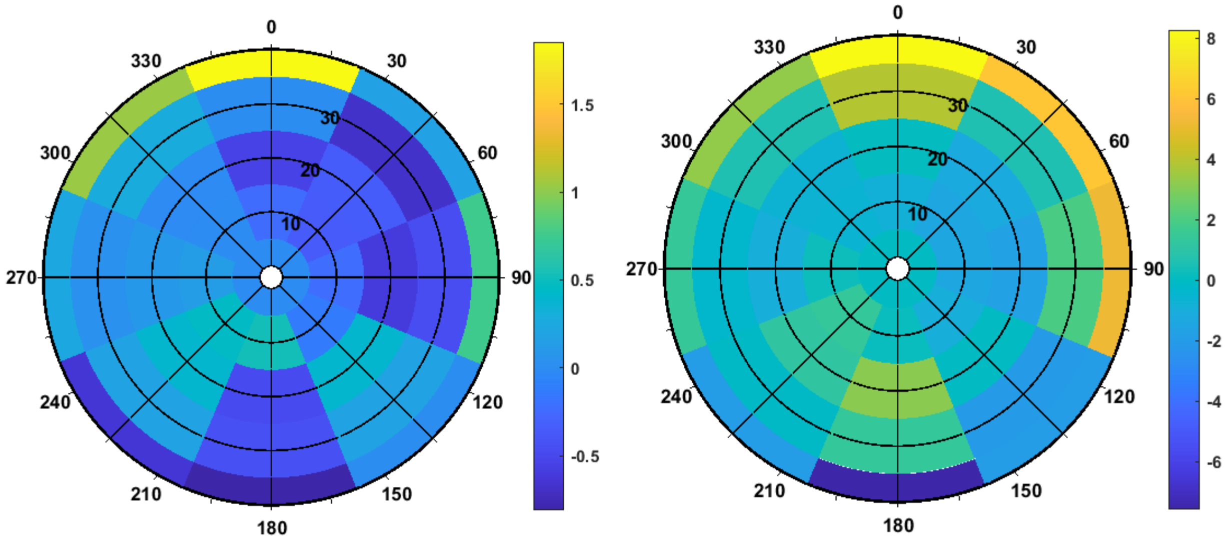

(a) Deviations of objective function values

(b) Deviations of energy consumption values

Figure 6.25: Deviations of values behind best starting locations based on the boundary layer wind field compared to the uniform wind field in percentages

6.4.5. Summary boundary layer wind results

This section described the optimized helicopter-ship approaches affected by the boundary layer wind field for various wind directions and speeds and four initial helicopter positions. The boundary layer results were also compared to the uniform wind results to assess the effect of model fidelity. The main conclusion is that both wind models show consistent results in similarity measures, constraints, and power peak trends as functions of wind conditions. Regions of low similarity are more distinct for the boundary layer results due to the modified vertical behaviour of the helicopter.

Most constraint violations were in line with the uniform wind results. The power constraint was less pronounced in the boundary layer results due to the exploitation of the wind gradient. Even when the power reached 100%, it was for a smaller period compared to the uniform wind trajectory. The NoGoZone violations of position 135° with winds from the North and North-West were observed in both wind models, similar to the violation of position 090° for 30 kts Westerly winds. The difference is that the boundary layer model also resulted in a collision for 40 kts Southerly winds starting from position 000°.

The ship's crosswinds illustrate interesting vertical behaviour in the boundary layer wind field since the helicopter utilizes the wind gradient to obtain a partial headwind to decelerate. Near the end of the approach, the helicopter ascents to produce more drag and match the ship's speed in time, while still approaching the vessel as fast as possible. Tailwinds, either during the approach or from the ship's perspective, may be dangerous as the total airspeed drops to zero and the helicopter effectively needs to fly backwards. This results in negative disc angles of attack, possibly hitting limits for this quantity or the longitudinal cyclic. Another endangering factor is the reduced tail clearance with the flight deck.

The best starting positions according to the objective function, integrated power and by distance normalized quantities show high resemblance with the uniform wind results. This means that rough estimations or initial guesses can be derived from the uniform wind model, while a higher fidelity model can be used to detail the trajectories and better estimate power requirements. Additionally, the objective and total energy values belonging to the best starting locations were compared between the two models. The slight changes in objective were mostly observable for strong Northerly winds, while the moderate changes in total energy were visible for strong winds from the North, East, and South. The main conclusion from these comparisons is that both the best objective and total energy are highly similar between the two wind models for low to moderate wind speeds, but become viable for higher wind velocities. In this situation, the aircraft manoeuvres vertically to use the wind gradient most effectively.

6.5. Downdraft behind the hangar

The last experiment involves the boundary layer wind model in combination with a more complex downdraft model around the flight deck derived from wind tunnel tests. The downdraft strength is manipulated to be 10% and 20% of the free stream airflow above the hangar, which is in line with previous research. Moreover, the ship's superstructure acts as a bluff body resulting in a wind velocity deficit around the flight deck, which only applies to the horizontal component of the wind velocity, not the downdraft strength. This effect is also taken into account separately to isolate their influences. This section highlights the effects of the downdraft and velocity deficit on the helicopter. First, the effects on the total airspeed are described, followed by the effects on power required and thrust coefficient. Lastly, the geometrical trajectories are compared. All downdraft situations are combined and compared to the optimized trajectory derived from the boundary layer wind field. The colours of the various lines indicate the true wind direction and speed, the types of lines denote the various wind models. Since the effects are mostly observed close to the deck, bar graphs are added which contain the parameter's values at the end of the approach.

6.5.1. Airspeed variations

The total airspeed as a function of normalized time is illustrated in Figure 6.26 (left). As expected, downdraft or velocity deficit only affects the airspeed near the end of the approach, indicating that the helicopter does not anticipate the near-deck effects by adjusting its speed. Only between 80%-90% of the approach, the velocity deficit is observable by a sharp decrease in airspeed, except for the tailwind situation where the airspeed increases. This is because the absolute tailwind and relative headwind have opposite directions, which increases the total airspeed when the relative headwind decreases. After all, with decreased wind speed, the airspeed approaches the ground speed. The no-wind situation continues to have a stable airspeed path as only the horizontal component of the true wind is affected. All in all, downdraft strengths have insignificant effects on the true airspeed, even during the final approach, while the velocity deficit for higher wind speeds has the helicopter anticipate by adjusting its airspeed at around 60% of the approach.

A bar graph is shown on the right of Figure 6.26, which indicate the final values of the total airspeed at the end of the approach for the various wind speeds and downdraft situations. Here it can be clearly seen that the downdraft increases the total airspeed by small amounts. This is because a vertical component is added to the total velocity vector. It can also be seen that the airspeed approaches the ground speed in the cases of velocity deficit near the hangar. This effect becomes more pronounced with wind speed as the deficit is a percentage.

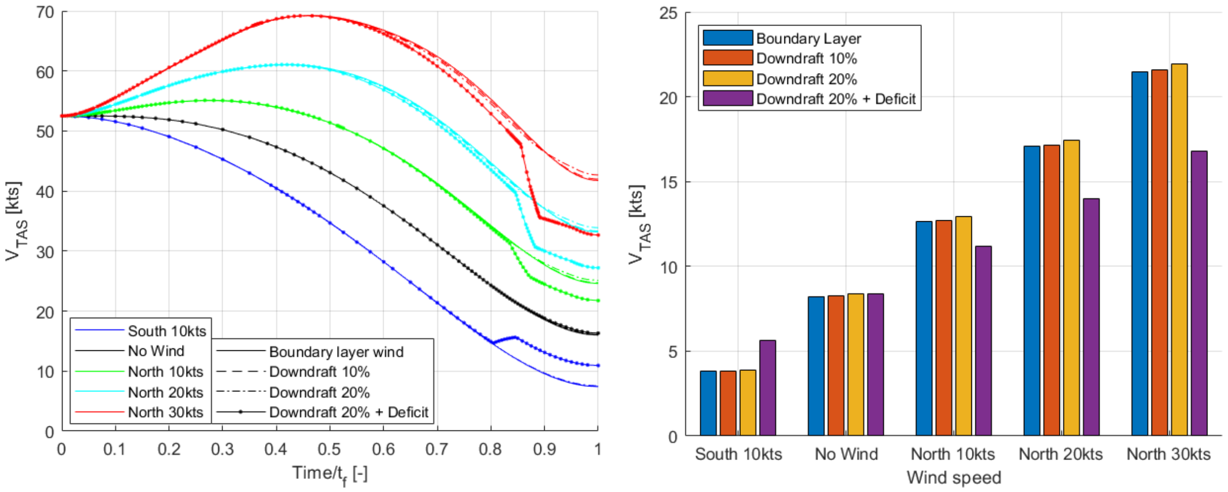

(a) True airspeed as function of normalized time

(b) True airspeed at the end of the trajectories

Figure 6.26: True airspeed as function of normalized time and final airspeed values of the approaches, resulting from the downdraft experiment

6.5.2. Performance effects

However, the power required is strongly affected by downdraft strengths, as shown in Figure 6.27. In the left graph, the required power during the approach is shown, which neither indicates anticipation of the helicopter. The small difference in the velocity deficit comes from the deviation in airspeed. Nevertheless, the downdraft causes the required power to rise close to the hangar, which becomes more severe and discontinuous for stronger downdraft strengths and wind speeds. The velocity deficit behind the hanger alleviates the power requirement for the tailwind and strongest headwind, but only by a negligible amount. This implies that the induced climb power is significantly more dominant than reduced airspeed. As can be seen from the right graph of Figure 6.27, all other relative wind speeds suffer from the velocity deficit due to the bucket shape of the power curve. The bar graphs show an extreme increase in required power to hover above the landing deck, which is also shown in Table 6.2. In this table, the deviations of the downdraft situations are compared to the boundary layer wind model results. It can be seen that power levels could rise significantly when the helicopter experiences downdraft.

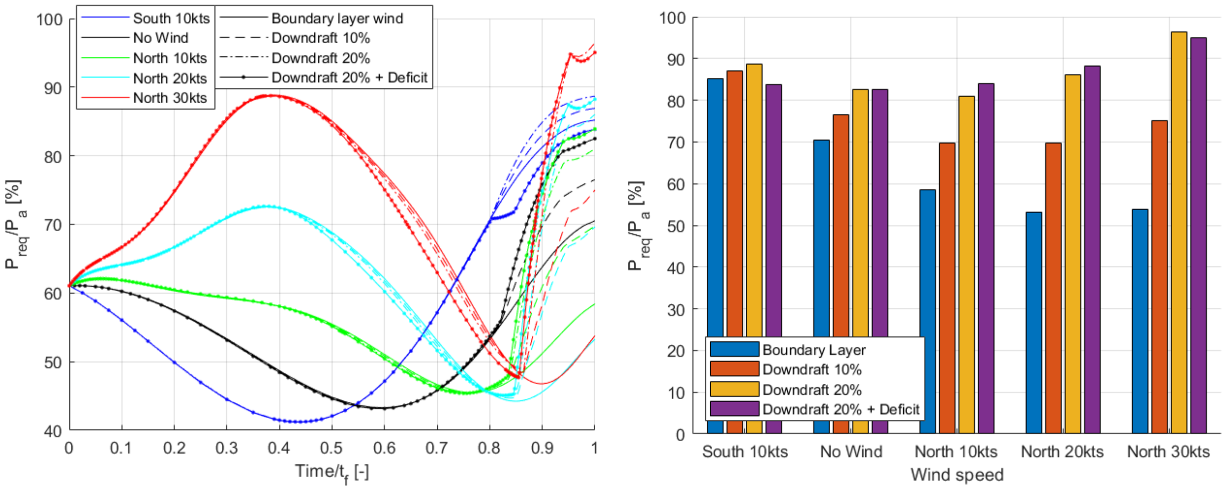

(a) Power required as function of normalized time **(b)** Power required at the end of the trajectories

Figure 6.27: Power required as a percentage of the maximum engine power as function of normalized time and final values of the approaches, resulting from the downdraft experiment

Table 6.2: Required power to hover above the flight deck prior to the landing for various relative wind speeds and downdraft strengths. The numbers in brackets indicate the deviation from the boundary layer wind model results (0% downdraft)

Downdraft / **Wind**	**0%**	**10%**	**20%**	**20% + Deficit**
Tail 10 kts	85.2	86.9 (+2.0%)	88.7 (+4.1%)	83.9 (-1.5%)
No wind	70.5	76.5 (+8.5%)	82.5 (+17.0%)	82.5 (+17.0%)
Head 10 kts	58.4	69.8 (+19.5%)	81.0 (+38.7%)	83.9 (+43.7%)
Head 20 kts	53.3	69.7 (+30.8%)	86.0 (+61.4%)	88.2 (+65.5%)
Head 30 kts	53.8	75.0 (+39.4%)	96.4 (+79.2%)	95.0 (+76.6%)

The airspeed, required power and the thrust coefficient are all connected, meaning that the latter is also affected by the downdraft (Figure 6.28). Similar to the required power, the helicopter adjusts the thrust halfway through the approach and increases it sharply in the final phase. This is because the helicopter effectively makes a climbing manoeuvre. Since the control effort is defined as the gradient of the thrust curve, it can be concluded that the control effort increases with downdraft strength. Although slightly decreasing in the final phase, the velocity deficit increases the control effort halfway through the approach as it prepares for its hover position above the landing deck. As can be seen from the right graph of Figure 6.28, the velocity deficit seems to reduce the total thrust in the final phase for Northerly winds, but the actual saving is only around 0.4% for the 30 kts headwind. The thrust actually increases in the tailwind case, due to the bucket shape of the power curve. Note that the variations may appear significant, but the deviation is only 1.16% when comparing the values between 20% downdraft and boundary layer results in a Northerly wind of 30 kts.

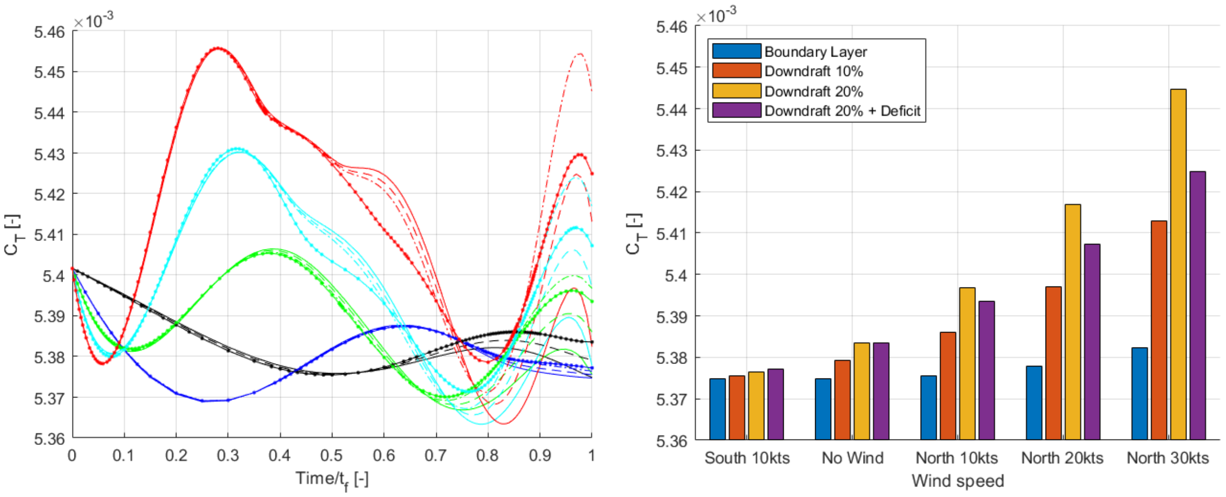

(a) Thrust coefficient as function of normalized time **(b)** Power required at the end of the trajectories

Figure 6.28: Thrust coefficient as function of normalized time and final values of the approaches, resulting from the downdraft experiment

6.5.3. Geometric characteristics

Lastly, the geometric deviations in the optimized trajectories are examined and depicted in Figure 6.29. Although the helicopter anticipates the near-deck effects by adjusting performance parameters, no deviations are observed halfway in the geometric paths towards the ship, except for the no-wind track which descents faster with increasing downdraft strength. By approaching the vessel from the desired hover altitude, the helicopter is able to absorb the downdraft better than when it is still descending. Other wind speeds display dissimilarities in vertical movements at the final approach. While the trajectory derived from the boundary layer model ascents to decelerate, paths subjected to the downdraft models exploit this effect to a lesser extent. This is to absorb the downdraft better close to the flight deck. Stronger headwinds subjected to the downdraft and deficit model tend to fly as low as possible, with minimal altitude changes.

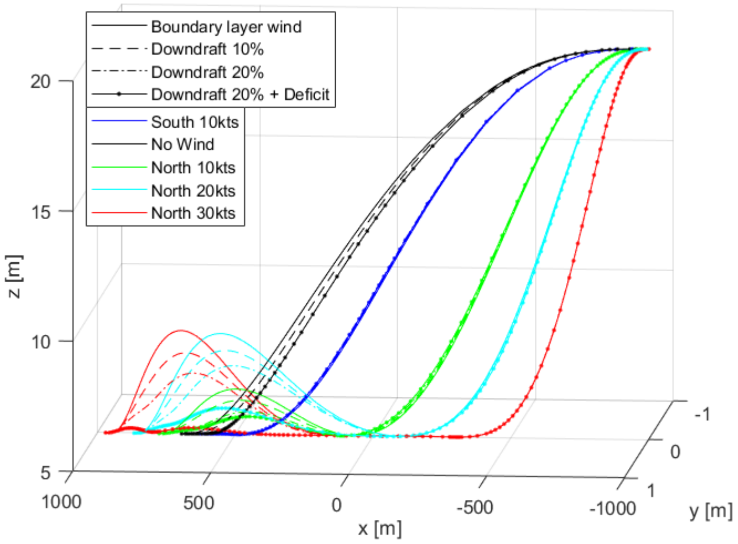

Figure 6.29: Optimized trajectories affected by the boundary layer wind field in combination with downdraft effects near the flight deck

6.5.4. Summary downdraft results

The downdraft model increases fidelity and accuracy compared to the boundary layer model and has significant impacts. The helicopter's airspeed is mostly affected by the wind velocity deficit behind the hangar, but not by the downdraft strength. On the other hand, downdraft strengths have significant effects on the required power, thrust, and control effort in the final phase of the approach. High wind speeds in combination with a strong downdraft could result in reaching the power limit prematurely as the power before the landing phase increases significantly. The wind velocity deficit does not alleviate this effect and could even deteriorate the power requirement due to the bucket shape of the power curve. Although not included in this experiment, the decrease in airspeed could increase the control effort even further due to other vortices and turbulence resulting from the ship's superstructure. Geometric deviations in the optimized trajectories are small, despite ascending less in the final phase of the approach.

6.6. Summary

This chapter discussed the results of all experiments in which three wind models were utilized for helicopter-ship approach trajectory optimization for four helicopter starting positions, eight wind directions and five wind speeds. The first two wind models involved a uniform and boundary layer wind profile, while the third detailed the flow behind the hangar. Trajectory shapes in windy environments were compared to the no-wind baseline tracks to reduce the overhead and keep the chapter manageable. After a thorough assessment, combinations of starting location, wind direction and speed were identified that violated constraints and are thus infeasible. Analysing dissimilarities between windy trajectories and the baseline tracks gave insight into the effect of wind direction and speed on the optimized trajectories.

The effects in the horizontal plane can be identified using the uniform wind field, while deviations in vertical movements can be observed through the boundary layer wind profile. The two give similar results for low to moderate wind speeds, but anomalies arise for strong winds. The change in vertical movement also affects the horizontal displacement of the helicopter, resulting in more practically feasible trajectories. However, adjustments should be made before implementing these trajectories into a flight controller. Additionally, the best starting locations per wind condition, based on the objective function, total energy consumption and by distance normalized quantities, were discussed and compared between the two wind models. Although the boundary layer model provides more accurate results, the best starting locations were highly similar with minor improvements. The last wind experiment included the downdraft effect behind the ship's hangar, increasing the power consumption, thrust, and control effort near the flight deck. This effect should be taken into account when approaching the vessel as it can be potentially dangerous.

This page is intentionally left blank.

7

Conclusions & Recommendations

This study focussed on optimized rotary-wing UAV approaches to the landing deck of a moving vessel in windy environments. For this objective, a trajectory optimization framework was created that involved models for helicopter dynamics and performance, a ship, several wind models and an optimal control transcription procedure and solver. Three wind models with increasing levels of accuracy were utilized to investigate how and to what extent the helicopter approaches were affected, but also to compare the results between wind models. Low-fidelity models were employed because of convergence success rates and computational costs that were already significant. Despite the limitations of these models, major effects and trends could be identified, providing the answer to the research question:

How does wind affect an optimal approach trajectory of an unmanned helicopter to the landing deck of a sailing small-deck Naval vessel?

The simulation framework generated results for optimized UAV-ship approaches in winds from seven directions and five different speeds. Furthermore, experiments were repeated for four different initial helicopter locations. On top of that, three different wind models were employed, resulting in many trajectories to conclude how wind affects optimal trajectories, how the initial location influences the result, to provide a sensitivity analysis of the different wind fields and to obtain knowledge how a large-scale effect around the flight deck influences optimal trajectories.

7.1. Conclusions

First of all, it can be concluded that the optimization framework with the various models works and can be employed for various situations. The framework can even be expanded to include multiple phases, such as an intermediate waiting station or the landing manoeuvre. Moreover, due to the large amount of experiments, a similarity measure was used to demonstrate deviations compared to an optimized path without being affected by wind. While it had to be tuned by hand, the LCSS algorithm showed great and intuitive results as the program can deal with varying time-history lengths and outputs a value between 0 and 1. Unlike the absolute distance between two measurement points, which did not yield eye-catching observations with a non-representing number. A similarity graph for a starting position can be estimated by the 000°-graph, rotated by its respective degree.

Optimized trajectories exploit the wind or wind gradient in such a way that extra ground speed in the initial phase or deceleration near the deck can be achieved. For example, crosswinds during the approach tend to deflect the optimal path with the wind and a vertical path is adjusted by using the wind gradient in the helicopter's advantage. Even though similarity values drop, the approaches are considered practical and can be used in maritime operations. The effect of wind shear (changing wind direction as function of altitude) was not considered, as this effect is assumed negligible during the approach. Deviations from the baseline tracks are minor for low wind speeds but become significant for higher velocities. However, clustering approaches based on a wind direction would be easier to implement in a flight controller, resulting in only minor penalties in flight time.

It has been shown that both wind direction and speed influence optimal approach trajectories, but changing the initial helicopter location can bypass adverse effects and performance constraints. A strong Northerly wind causes the power to reach the limit for starting positions 000° and 045°, but not for the other two, indicating that strong winds are better handled as a crosswind during the approach. Similarly, for a given wind condition, the best starting position was never the one that had a headwind during the approach. Tailwinds during the approach resulted in collision difficulties for positions 090° and 135°, partly due to the lower flight distance and the struggle to decelerate and match the ship's speed. Thus, starting from behind or from the vessel's starboard side is beneficial in Northerly to Westerly winds.

Headwinds, either during the approach or from the ship's perspective, and tailwinds from the ship's perspective generally require more power. This is independent of the helicopter's starting position. The former is because of the increased airspeed, reaching the limit for from-behind approaches for 40 kts wind speeds. The helicopter is capable of flying in this wind as the maximum velocity was never reached, but approaching the ship in minimal time requires maximum power. The power increase due to tailwinds is because of the decreased airspeed and bucket shape of the power curve. Even without the reduced power surplus, tailwinds are potentially dangerous because of backward flying limits (disc angle of attack, aft cyclic margins, etc) and vertical tail clearance with the flight deck.

Deviations in wind models become significant for stronger wind velocities, but do not depend on wind directions. Most remarkably, in the uniform wind field the helicopter exchanges potential and kinetic energy for strong headwinds because of the power restriction, while in the boundary layer wind field the helicopter flies as low as possible to obtain the weakest headwind possible. Between best starting positions, differences in objective function are insignificant, but total energy values deviate between -6% and 8%, meaning that a higher fidelity wind model is necessary to estimate performance characteristics in real wind scenarios. The downdraft behind the hangar in Northerly winds has a substantial impact on the required power before the landing phase, meaning that this effect should be taken into account while determining SUOLs. The downdraft strength depends on the ship's superstructure and hangar height and if doubled, the extra power required compared to the boundary layer wind model, is also doubled. The wind velocity deficit behind the hangar did not yield significant results on the control effort or power required. However, the instant drop in airspeed could result in dangerous situations when including other effects such as turbulence or strong vortices.

The Royal Netherlands Navy wishes to deploy UAVs with wind speeds up to wind force 7 on Beaufort's scale, equivalent to a wind speed of 30 kts. This study proved that UAV approaches can be executed in these winds without reaching the power limit. Even when including a severe downdraft, the power surplus is still 5%. However, not all starting positions can be used for these wind velocities as the NoGoZone constraint was violated for positions 090° and 135°. Despite being able to fly in these winds, the helicopter should not collide with the vessel, requiring either a different starting position or an adjusted velocity path. The created framework and results of this study can be used to determine newly standardized approach manoeuvres for maritime UAVs by clustering approaches based on wind direction and initial location. Furthermore, it can contribute to estimating SUOLs or handling qualities since the optimizer always attempts to find an approach manoeuvre within the imposed performance constraints; a performance limitation is reached when no approach is deemed feasible. Although SUOLs can be sketched by performance limitations, these operational limits also involve other aspects such as flight deck layout (cranes on deck) and ship-helicopter interactions, which need to be taken into account in either higher-fidelity models or actual flight tests.

7.2. Recommendations

This study investigated major wind effects on a low-fidelity helicopter model, for which some parameters were estimated. Future work should therefore include an assessment of both the UAV's capabilities and limitations. Knowing more about the aircraft could have resulted in a partial SUOL by applying its limits, especially for backwards flying during tailwinds. Even though the helicopter is a research aircraft, it resembles the maritime drone market and other UAVs with similar specifications will produce equivalent results.

Moreover, future work should validate the optimized trajectories, including the performance indicators. This can be done via a high-fidelity helicopter model or through actual flight tests. A flight controller for the PH-1AA Orange Eye helicopter has already been designed and validated in the NOTUS project. By implementing the optimized trajectories, one can validate the feasibility of the paths in the virtual system or actual flight tests. In this way, one can validate the applicability of the proposed trajectories and the effectiveness of using a low-fidelity point-mass model to optimize ship-helicopter approaches.

It is also important to do a sensitivity study on the objective function, initial helicopter speed and distance to the ship. By adjusting the weighting factor K_{t_f}, initial speed or distance, one might find fewer NoGoZone constraint violations. In this study, the optimizer had great difficulty recovering from a NoGoZone constraint violation, resulting in significantly deviating paths, mostly caused by a high initial speed and the urge for the lowest flying time. Lowering the importance of flying time in a sensitivity study might reveal more insight and expand the flight envelope. As actual SUOLs will be defined as a function of relative winds, the ship's speed is considered a secondary effect, which does not have to be included in the sensitivity study.

It is also advised to optimize trajectories for intermediate wind speeds, directions and starting positions to acquire a finer grid for the polar graphs. In particular cases, a trajectory has an unknown kink point, which can be determined by simulating intermediate wind speeds for the specific wind direction. Moreover, both similarity and best starting locations graphs indicate that intermediate positions might be advantageous over the proposed initial positions. Future work can include this hypothesis by optimizing approaches using the designed framework. Another option to use the framework is to optimize trajectories with a different objective, such as minimum energy trajectories. In addition, the LCSS algorithm can also be used as an objective if one is interested in how much a path needs to deviate from a reference case to be feasible in extreme weather conditions.

The framework can also be expanded to include multi-phase trajectory optimization, including a waiting station, phase-dependent constraints or the landing phase. Ship landings have been studied extensively, but not in the context of optimal paths in a wind field. The ship's airwake could have major effects on the landing trajectory, besides determining the best timing to initiate the landing due to the deck movements. Another way to utilize the created program is to optimize ship-helicopter take-off manoeuvres, for which SUOLs are necessary as well. Although flight characteristics in a certain wind field might be similar for approaches and take-offs, passing from the ship airwake to the undisturbed flow might bring complications.

Lastly, UAVs in maritime operations need communication links with the ship to approach and land on the vessel. A recommendation for future work is to study how to connect the RNLN's software with the UAV's on board flight controller and to implement standardized approach and landing manoeuvres. This could be done autonomously by implementing all paths into the aircraft's memory and using a grid as function of relative winds, by sending a specific manoeuvre to the UAV, using Artificial Intelligence/Neural Networks or by clustering optimal manoeuvres as a function of wind direction and have the UAV decide on the manoeuvre and starting position.

This page is intentionally left blank.

References

[1] J. Trent. “Data From Above: The Advantages of Unmanned Aircraft”. In: *Journal of Petroleum Technology* 65.10 (2013), pp. 36–43. DOI: `10.2118/1013-0036-JPT`.

[2] Commando Zeestrijdkrachten NLD and Bundesamt für Ausrüstung; Informationstechnik und Nutzung der Bundeswehr (BAAINBw) DEU. *Technical Arrangement to the Memorandum of Understanding between the Federal Ministry of Defence of the Federal Republic of Germany and the Minister of Defence of the Kingdom of the Netherlands concerning the Cooperation in the Field of Research and Technology on ShiP-deck Environment and Efficient Drone Operations (SPEEDOPS)*. 2023.

[3] NATO. *Helicopter Operations From Ships Other Than Aircraft Carriers (HOSTAC)*. Edition (H) Version (4). 2022. MPP-02 Volume I.

[4] Ministerie van Defensie. *Handboek Helikopter Handling*. LAND-CA-3D-4-42. Versie 3.1.

[5] Koninklijke Marine. *Opereren met helikopters aan boord van CZSK-eenheden*. 2022. V-CZSK ALG 010.

[6] J. Forsman and M. Westergren. “Potential and limitations with UAV deliveries to ships at sea”. In: *Department of Mechanics and Maritime Sciences, Chalmers University of Technology, Gothenburg, Sweden* (2019). Bachelor thesis in Marine Engineering.

[7] C. Castillo et al. “Autonomous UAV Landing on a Moving Vessel: Localization Challenges and Implementation Framework”. In: *Internet of Things, Smart Spaces, and Next Generation Networks and Systems* (Sept. 2019). DOI: `10.1007/978-3-030-30859-9_29`.

[8] R.J.J. Bakker, M. Voskuijl, and D. Zilver. *Simulation model and control system of the PH-1AA unmanned helicopter*. NLR-CR-2023-118. 2023.

[9] M. Voskuijl et al. “Simulation of automatic helicopter deck landings using nature inspired flight control and flight envelope protection”. In: *The Aeronautical Journal* 114.1151 (2010), pp. 25–34. DOI: `10.1017/S000192400000350X`.

[10] S. Abujoub, J. McPhee, and R. A. Irani. “Methodologies for landing autonomous aerial vehicles on maritime vessels”. In: *Aerospace Science and Technology* (2020). Department of Mechanical and Aerospace Engineering, Carleton University, Ottawa, Ontario, Canada. DOI: `10.1016/j.ast.2020.106169`.

[11] Alrik Hoencamp, Theo van Holten, and J. V. R. Prasad. “Relevant aspects of helicopter-ship operations”. In: 2008. URL: `https://dspace-erf.nlr.nl/server/api/core/bitstreams/120cca42-a008-47f8-872d-a423e542d5d3/content`.

[12] A. Hoencamp. “Helicopter-Ship Qualification Testing”. ISBN 978-94-6259-565-1. PhD thesis. Delft University of Technology, 2015.

[13] S. Coyle. *The Art and Science of Flying Helicopters*. ISBN 0-8138-2169-X. Iowa State University Press, 1996.

[14] European Helicopter Safety Team (EHEST). *Helicopter Performance for Helicopter Pilots - Training Leaflet*. 2017.

[15] Ger J.J. Ruijgrok. *Elements of airplane performance*. ISBN 978-90-6562-203-7. Delft Academic Press (DAP), 2009.

[16] A. Wall et al. *Opportunities for expanding shipboard-helicopter operational envelopes using modelling and simulation tools*. NATO STO-MP-MSG-159.

[17] G.H. Hegen, J.F. Hakkaart, et al. *Wind Tunnel Flow Visualization Tests on a Model of the LPD ”HR.MS. Rotterdam”*. NLR-CR-99106. 1999.

[18] R. Fang and P. J. A. Booy. *First of Class Trials on Board the Royal Netherlands Navy Landing Platform dock (LPD) ”Hr.Ms. Rotterdam” with the Westland Lynx SH-14D Helicopter*. NLRCR-2000-610. 2000.

[19] C.H. Kääirä. “Investigating the Impact of Ship Superstructure Aerodynamics on Maritime Helicopter Operations”. PhD thesis. University of Liverpool, 2012.

[20] Z. Feng et al. “Efficient Drone Hijacking Detection using Onboard Motion Sensors”. In: *Design, Automation and Test in Europe Conference Exhibition (DATE)* (2017), pp. 1414–1419. DOI: `10.23919/DATE.2017.7927214`.

[21] L. Wang and X. Bai. “Quadrotor Autonomous Approaching and Landing on a Vessel Deck”. In: *Journal of intelligent robotic systems* 92.1 (2018), pp. 125–143. DOI: `10.1007/s10846-017-0757-5`.

[22] JAPCC. “Transforming Joint Air Power”. In: *The Journal of the JAPCC* (). Edition 25, Winter 2017/2018. Retrieved from https://www.japcc.org/wp-content/uploads/JAPCC_J25_screen.pdf.

[23] N. Van Donghen et al. *Challenges of Operating VTOL UAS to Support Maritime Operations*. NATO Industrial Advisory Group (NIAG) Study Group 277. June 2023.

[24] S.A.H. Mohsan et al. “Unmanned aerial vehicles (UAVs): practical aspects, applications, open challenges, security issues, and future trends”. In: *Intelligant Service Robotics* 16 (2023), pp. 109–137. DOI: `10.1007/s11370-022-00452-4`.

[25] James S. Forrest et al. “Ship–Helicopter Operating Limits Prediction Using Piloted Flight Simulation and Time-Accurate Airwakes”. In: *Journal of Aircraft* 49.4 (2012), pp. 1020–1031. DOI: `10.2514/1.C031525`.

[26] S.J. Tate. “A Dynamic Challenge: Helicopter/Ship Interface Simulation – Development, Integration and Application”. In: *Defence Research Agency - Flight Dynamics and Simulation Department* (1995). AGARD-CP-577, AGARD Flight Vehicle Integration Panel Symposium on ‘FlightSimulation Where are the Challenges?’, Braunschweig, Germany, May 1995, pp. 10.1–10.16.

[27] P. Comeau, Alanna Wall, et al. “Supporting shipboard helicopter flight testing with simulation and metrics for predicting pilot workload”. In: *The Journal of Defense Modeling and Simulation* (2022). SAGE Publications. DOI: `10.1177/15485129221118937`.

[28] M. Voskuijl et al. “Simulation of automatic helicopter deck landings using nature inspired flight control and flight envelope protection”. In: *The Aeronautical Journal* 114.1151 (Jan. 2010), pp. 25–34. DOI: `10.1017/S000192400000350X`.

[29] Tri D. Ngo and Cornel Sultan. “Model Predictive Control for Helicopter Shipboard Operations in the Ship Airwakes”. In: *Journal of Guidance, Control and Dynamics* 39.3 (Mar. 2016), pp. 574–589. DOI: `10.2514/1.G001243`.

[30] I. Owen et al. “A virtual engineering approach to the ship-helicopter dynamic interface – a decade of modelling and simulation research at the University of Liverpool”. In: *The Aeronautical Journal* 121.1246 (Dec. 2017), pp. 1833–1857. DOI: `10.1017/aer.2017.102`.

[31] W.A. Memon, I. Owen, and M.D. White. “SIMSHOL: A Predictive Simulation Approach to Inform Helicopter–Ship Clearance Trials”. In: *Journal of Aircraft* 57.5 (Oct. 2020), pp. 854–875. DOI: `10.2514/1.C035677`.

[32] J.M.P. Figureira, A. Taghizad, and M. Abid. “The use of Simulation Tools to Estimate Ship-Helicopter Operating Limitations”. In: *AIAA Aviation Forum* (June 2017). AIAA Modeling and Simulation Technologies Conference. DOI: `10.2514/6.2017-4331`.

[33] P.J.A. Booij et al. “Dutch helicopter-ship qualification - Ready for the future”. In: *Nationaal Lucht- en Ruimtevaartlaboratorium (NLR)* (2006). NLR-TP-2006-568.

[34] T.R. Fell et al. “Initial Progress to Establish Flying Qualities Requirements for Maritime Unmanned Aircraft Systems”. In: *European Rotorcraft Forum (ERF)* (2014). Universities of Liverpool and Lincoln.

[35] T.R. Fell et al. “Towards establishing flying qualities requirements for maritime unmanned aircraft systems”. In: *Annual Forum Proceedings - AHS International* 2 (Jan. 2015), pp. 1465–1474.

[36] T.R. Fell et al. “Progress in Establishing Scalable Flying Qualities Requirements for Maritime Umanned Rotorcraft Systems”. In: *European Rotorcraft Forum (ERF)* (2016). Universities of Liverpool and Lincoln.

[37] T.M. Foster. *Dynamic Stability and Handling Qualities of Small Unmanned-Aerial-Vehicles*. MSc thesis. Brigham Young University. 2005.

[38] James S. Forrest and Ieuan Owen. “An investigation of ship airwakes using detached-eddy simulation”. In: *Computers & Fluids* 39.4 (2010), pp. 656–673. DOI: `10.1016/j.compfluid.2009.11.002`.

[39] N. Taymourtash et al. “Wind tunnel investigation of a helicopter model in shipboard operations”. In: *European Rotorcraft Forum* 1 (2019), pp. 111–123.

[40] J.S. Forrest et al. “An investigation of ship airwake phenomena using time-accurate CFD and piloted helicopter flight simulation”. In: *European Rotorcraft Forum* (2008).

[41] A. Sharma et al. “Simulation of Maritime Helicopter Dynamics During Approachto Landing With Time-Accurate Wind-Over-Deck”. In: (2019). DOI: `10.2514/6.2019-0861`.

[42] A. Sharma, A. Padthe, and P.P. Friedmann. “Helicopter Shipboard Landing Simulation Including Wind, Deck Motion and Dynamic Ground Effect”. In: *JOURNAL OFAIRCRAFT* 58.3 (2021), pp. 467–486. DOI: `10.2514/1.C035973`.

[43] D. Lee et al. “Simulation of Helicopter Shipboard Launch and Recovery with Time-Accurate Airwakes”. In: *Journal of Aircraft* 42.2 (2005), pp. 448–461. DOI: `10.2514/1.6786`.

[44] D.E. Siccama. *Helicopter response to 3-D turbulent flow around high-rise buildings*. MSc thesis. Delft University of Technology. 2004.

[45] S. Jacobs et al. “The advantages and disadvantages of using High Fidelity Simulation as an environment to observe undergraduate nurses’ actions and their alignment with clinical judgement characteristics”. In: *Clinical Nursing Studies* 8.1 (2020). SCIEDU, pp. 15–20. DOI: `10.5430/cns.v8n1p15`.

[46] T. Horeman, K. Akhtar, and G.J. Tuijthof. *Effective Training of Arthroscopic Skills - Physical simulators*. ISBN: 978-366244943-1, 978-366244942-4. Springer Berlin Heidelberg, 2015. DOI: `10.1007/978-3-662-44943-1_6`. pp. 57-69.

[47] Z.B. Zabinsky, G. Pedrielli, and H. Huang. “A Framework for Multi-fidelity Modeling in Global Optimization Approaches”. In: *Machine Learning, Optimization and Data Science* 11943 (2019). 5th International Conference on Machine Learning, Optimization, and Data Science, pp. 335–346. DOI: `10.1007/978-3-030-37599-7_28`.

[48] L. Xia and Z. Gao. “Application of variable-fidelity models to aerodynamic optimization”. In: *Applied Mathematics and Mechanics* 27.8 (Aug. 2006), pp. 1089–1095. DOI: `10.1007/s10483-006-0809-z`.

[49] M.H. Bakr et al. “Review of the Space Mapping Approach to Engineering Optimization and Modeling”. In: *Optimization and Engineering* 1 (2000), pp. 241–276. DOI: `https://doi.org/10.1023/A:1010000106286`.

[50] H.G. Visser. *Course AE4447 Aircraft Performance Optimization*. Jan. 2014.

[51] M. Kelly. “An Introduction to Trajectory Optimization: How to Do Your Own Direct Collocation”. In: *Society for Industrial and Applied Mathematics* 59.4 (Nov. 2017). SIAM REVIEW, pp. 849–904. DOI: `https://doi.org/10.1137/16M106256`.

[52] M. Kelly. “Transcription Methods for Trajectory Optimization: a beginners tutorial”. In: *arXiv: Optimization and Control* (Feb. 2015). URL: `https://api.semanticscholar.org/CorpusID:119307108`.

[53] D. Mosconi, C.E. Luizete, and A.A.G. Siqueira. “Direct Collocation Method For Solving Optimal Control Problems”. In: Engineering - Automation, Robotics, Metrology and Energy: Studies and Trends - Volume 1 - Chapter 16. Crossref, 2023, pp. 246–264. DOI: `10.37885/230111777`.

[54] Z. Cai et al. “Obstacle Avoidance and Tajectory Tracking Control of a Quadcopter UAV Under Wind Conditions”. In: *International Conference on Guidance, Navigation and Control* (2023), pp. 6053–6062. DOI: `10.1007/978-981-19-6613-2_585`.

[55] S. Dugar, S. Choudhury, and S. Scherer. “Smooth Trajectory Optimization in Wind: First Results on a Full-Scale Helicopter”. In: *Annual Forum & Technology Display* (2017).

[56] S. Hartjes. “An Optimal Control Approach to Helicopter Noise and Emissions Abatement Terminal Procedures”. PhD thesis. Delft University of Technology, 2015.

[57] Y. Zhao, A.A. Jhemi, and R.T.N. Chen. “Optimal Vertical Takeoff and Landing Helicopter Operation in One Engine Failure”. In: *Journal of Aircraft* 33.2 (1996), pp. 337–346.

[58] H.G. Visser. “OPTIMIZATION OF BALANCED FIELD LENGTH PERFORMANCE OF MULTI-ENGINE HELICOPTERS”. In: *AIAA* (2000), pp. 150–162. DOI: `10.2514/6.1999-4019`.

[59] S.F. Tang. *Optimization of Helicopter Noise Abatement Arrival Trajectories with the Software Tool NOISHHH*. MSc thesis. Delft University of Technology. 2007.

[60] D.J. Hendriks. *Optimization of Helicopter Noise and Emissions Abatement Departure Procedures*. MSc thesis. Delft University of Technology. 2013.

[61] T. Tsuchiya et al. “Numerical Simulation of Real-Time Trajectory Optimization for Helicopter Noise Abatement”. In: *Journal of Mechanical Systems for Transportation and Logistics* 3.2 (2010), pp. 415–430. DOI: `10.1299/jmtl.3.415`.

[62] T. Tsuchiya et al. “Real-Time Trajectory Optimization for Noise Abatement of Helicopter Landings”. In: *Journal of Mechanical Systems for Transportation and Logistics* 4.2 (2011), pp. 95–110. DOI: `10.1299/jmtl.4.95`.

[63] *U.S. Standard Atmosphere, 1976*. NOAA-S/T 76-1562. U.S. Government Printing Office, Washington, D.C.

[64] E. Mooij. *The motion of a vehicle in a planetary atmosphere*. 1.4. ISBN 90-5623-003-4. Delft University of Technology - Faculty of Aerospace Engineering, Dec. 1997.

[65] H.G. Visser, M.D. Pavel, and S.F. Tang. “Optimization of Rotorcraft Simultaneous Non-Interfering Noise Abatement Approach Procedures”. In: *Journal of Aircraft* 46.6 (2009), pp. 2156–2161. DOI: `https://doi.org/10.2514/1.39763`.

[66] T. van Holten and J.A. Melkert. *AE4-213 Helicopter Performance Stability and Control*. Translation and revision of the original Dutch version by B. Marrant and M. Pavel. Faculty of Aerospace Engineering - Delft University of Technology, 2002.

[67] G.D. Padfield. *Helicopter Flight Dynamics including a treatment of Triltrotor Aircraft*. 3rd ed. ISBN 9781119401056. Wiley, 2018.

[68] I.C. Cheeseman and W.E. Bennet. “The Effect of the Ground on a Helicopter Rotor in Forward Flight”. In: *Aeronautical Research Council - Reports and Memoranda* 3021 (1955).

[69] United States Army Aviation and Missile Command. *Aeronautical Design Standard - Performance Specification Handling Qualities Requirements for Military Rotorcraft*. ADS-33E-PRF. May 1996.

[70] G. Guglieri and R. Celi. “Some Aspects of Helicopter Flight Dynamics in Steady Turns”. In: *Journal of Guidance, Control and Dynamics* 21.3 (1998), pp. 383–390. DOI: `10.2514/2.4270`.

[71] A.V. Romero. “Aircraft Trajectory Optimization Using Parametric Optimization Theory”. ISBN 978-94-6259-565-1. PhD thesis. Universidad de Sevilla Escuala Téchnica Superior de Ingeniería, 2012.

[72] Z. Cai et al. “Obstacle Avoidance and Trajectory Tracking Control of a Quadrotor UAV Under Wind Disturbance”. In: *Springer, Singapore* 845 (2023). Advances in Guidance, Navigation and Control. ICGNC 2022. Lecture Notes in Electrical Engineering, pp. 6053–6062. DOI: `10.1007/978-981-19-6613-2_585`.

[73] F. Xiang, T. Shen, and D. Li. “Trajectory planning for mini unmanned helicopter in obstacle and windy environments”. In: *Aircraft Engineering and Aerospace Technology* 90.5 (2018). School of Aeronautic Science and Engineering, Beihang University, pp. 806–814. DOI: `10.1108/AEAT-05-2016-0080`.

[74] Y. Nie, O. Faqir, and E.C. Kerrigan. “ICLOCS2: Try this Optimal Control Problem Solver Before you Try the Rest”. In: *2018 UKACC 12th International Conference on Control (CONTROL)*. Sept. 2018, pp. 336–336. DOI: `10.1109/CONTROL.2018.8516795`.

[75] M. Diehl. *Lecture Notes on Numerical Optimization (Preliminary Draft)*. Department of Microsystems Engineering and Department of Mathematics, University of Freiburg, Germany, Mar. 2016.

[76] J. Wieringa and P.J. Rijkoort. *Windklimaat van Nederland*. Koninklijk Nederlands Meteorologisch Instituut - De Bilt. ISBN 90 12 044669. Staatsuitgeverij, Den Haag, 1983.

[77] J.C. Kaimal and J.J. Finnigan. *Atmospheric Boundary Layer Flows - Their Structure and Measurement*. ISBN 0-19-506239-6. Oxford University Press, 1994.

[78] N.J. Cook. “The Deaves and Harris ABL model applied to heterogeneous terrain”. In: *Journal of Wind Engineering and Industrial Aerodynamics* 66.3 (1997), pp. 197–214. DOI: `10.1016/S0167-6105(97)00034-2`.

[79] S. A. Hsu and E. A. Meindle D. B. Gilhousen. “Determining the Power-Law Wind-Profile Exponent under Near-Neutral Stability Conditions at Sea”. In: *American Meteorological Society* (1994), pp. 757–765. DOI: `10.1175/1520-0450(1994)033<0757:dtplwp>2.0.co;2`.

[80] Y. Tominaga and M. Shirzadi. “Wind tunnel measurement dataset of 3D turbulent flow around a group of generic buildings with and without a high-rise building”. In: *Data in Brief* 39 (2021). DOI: `10.1016/j.dib.2021.107504`.

[81] Y. Tao et al. “A comparative analysis of trajectory similarity measures”. In: *GIScience Remote Sensing* 58.5 (2021), pp. 643–669. DOI: `10.1080/15481603.2021.1908927`.

[82] M. Vlachos, G. Kollios, and D. Gunopulos. “Discovering similar multidimensional trajectories”. In: *Proceedings 18th International Conference on Data Engineering*. 2002, pp. 673–684. DOI: `10.1109/ICDE.2002.994784`.

[83] T. Górecki. “Using derivatives in a longest common subsequence dissimilarity measure for time series classification”. In: *Pattern Recognition Letters* 45 (2014), pp. 99–105. DOI: `10.1016/j.patrec.2014.03.009`. URL: `https://api.semanticscholar.org/CorpusID:34210631`.

[84] M.V. Cook. *Flight Dynamics Principles - A Linear Systems Approach to Aircraft Stability and Control*. 3rd ed. ISBN 978-0-08-098242-7. Elsevier, 2009.

[85] C. Rumsey. *2DN00: 2D NACA 0012 Airfoil Validation Case*. NASA - Langley Research Center - Turbulence Modeling Resource. Sept. 2020. URL: `https://turbmodels.larc.nasa.gov/naca0012_val.html`. Date accessed: 10 Jan 2024.

[86] J.G. Leishman. *Principles of Helicopter Aerodynamics*. ISBN 0-521-66060-20. Cambridge University Press, 2000.

[87] S.A.S. Hassan et al. *Helicopter Design & Aerodynamics*. Experiment Findings. June 2023.

[88] W. Johnson, H. Yeo, and C.W. Acree. “Performance of Advanced Heavy-Lift, High-Speed Rotorcraft Configurations”. In: *Aeroflight Dynamics Directorate (AMRDEC) - Aeromechanics Branch (NASA)* (2017). NASA and U.S. Army Research, Development, and Engineering Command Ames Research Center, Moffett Field, California. URL: `https://ntrs.nasa.gov/citations/20080047713`.

This page is intentionally left blank.

Additional Sources

A. Aircraft Systems Tech. Helicopter Flight Conditions (Hovering, Vertical, Forward Flight and Autorotation). url: https://www.aircraftsystemstech.com/p/helicopter-flight-conditions.html. Date accessed: 17 Nov 2023

B. Leonardo. Helicopters for naval missions. Sept. 2017. url: https://www.leonardo.com/en/news-and-stories-detail/-/detail/helicopters-for-naval-missions. Date accessed: 3 Nov 2023

C. Fabrice Wolf. Bij de Nederlandse Marine draait het allemaal om drones! Apr. 2024. url: https://meta-defense.fr/nl/2024/04/17/nederlandse-marine-heeft-alles-drone. Date accessed: 25 Apr 2024

D. C. Ryan. Drone vs. Helicopters – Utility Inspections. Constellation - Clearsight. url: https://constellationclearsight.com/blog/drone-vs-helicopters-utility-inspections. Date accessed: 10 Nov 2023

E. Jaime Karremann. Amfibische Transportschepen krijgen mogelijk doorlopend dek. Apr. 2024. url: https://marineschepen.nl/nieuws/Meer-details-Amfibische-Transportschepen-090424.html. Date accessed: 25 Apr 2024.

F. Ampelmann. Do you need access to an offshore platform? We'll get you there. url: https://www.ampelmann.nl. Date accessed: 29 Apr 2024

G. Joe Hudson. Ground effect: What it is, and what is isn't. HeliSimmer. Feb. 2019. url: https://www.helisimmer.com/articles/ground-effect. Date accessed: 30 Apr 2024

H. Aviation Safety Staff. Water Effect? Aviation Safety Digital Issue. Dec. 2019. url: https://www.aviationsafetymagazine.com/unicom/water-effect. Date accessed: 30 Apr 2024

I. Aircraft Systems Tech. Helicopter Flight Conditions (Hovering, Vertical, Forward Flight and Autorotation). url: https://www.aircraftsystemstech.com/p/helicopter-flight-conditions.html. Date accessed: 17 Nov 2023

J. National Weather Service. Beaufort Wind Scale. url: https://www.weather.gov/mfl/beaufort. Date accessed: 10 Nov 2023.

K. National Weather Service. Saffir-Simpson Hurricane Scale. url: https://www.weather.gov/mfl/saffirsimpson. Date accessed: 03 May 2023

L. Start NOTUS-project. July 2020. url: https://faculteitmilitairewetenschappen.nl/news/view/92b996ee-39d5-4a53-a64c-cf7cfadd2b9b/start-notus-project. Date accessed: 8 Nov 2023

M. NLR draagt bij aan onderzoek onbemande helikopter-schip operaties. Dec. 2017. url: https://www.nlr.nl/nieuws/nlr-draagt-bij-aan-onderzoek-onbemande-helikopter-schip-operaties. Date accessed: 8 Nov 2023

N. DARPA. Tern (Archived). Defence Advanced Research Projects Agency (DARPA). 2015. url: https://www.darpa.mil/program/tern. Date accessed: 13 May 2024

O. Loughborough University. Autonomous landing of a helicopter at sea: advanced control in adverse conditions(AC2). UK Research and Innovation (UKRI). 2017-2019. url: https://gtr.ukri.org/projects?ref=EP%2FP012868%2F1. Date accessed: 13 May 2024

P. NAVY Lookout. PROTEUS – developing an uncrewed helicopter for the Royal Navy. Independent Royal Navy news and analysis. Oct. 2023. url: https://www.navylookout.com/proteus-developing-an-uncrewed-helicopter-for-the-royal-navy. Date accessed: 13 May 2024

Q. Y. Lee. South Korea Launches Development Of Ship-Based UAV. Naval News. Feb. 2024.
url: https://www.navalnews.com/naval-news/2024/02/south-korea-launches-development-of-ship-based-uav. Date accessed: 13 May 2024

R. E. Huberdeau. Naval unmanned aerial system tested at sea from a French Navy frigate. AIRBUS Helicopters. Oct. 2023.
url: https://www.airbus.com/en/newsroom/press-releases/2023-10-naval-unmanned-aerial-system-tested-at-sea-from-a-french-navy. Date accessed: 13 May 2024

S. Global Times. China's AVIC completes onboard testing flight for shipborne unmanned helicopter. July 2022.
url: https://www.globaltimes.cn/page/202207/1271201.shtml. Date accessed: 13 May 2024

T. T. Hollingsbee. COLUMN | SHIP-LAUNCHED UAVS SET TO REVOLUTIONISE NAVAL AVIATION [NAVAL GAZING]. Baird Maritime. July 2022.
url: https://www.bairdmaritime.com/security/naval/column-ship-launched-uavs-set-to-revolutionise-naval-aviation-naval-gazing. Date accessed: 13 May 2024

U. F. Tan. The Differences Between Low Fidelity vs. High Fidelity Prototyping. Protopy - Industry Guide. July 2021.
url: https://www.protopie.io/blog/low-fidelity-vs-high-fidelity-prototyping. Date accessed: 10 Nov 2023

V. Searforces Naval Information. Holland class Offshore Patrol Vessel / OPV.
url: https://www.seaforces.org/marint/Netherlands-Navy/Offshore-Patrol-Vessel/Holland-class.htm. Date accessed: 15 Feb 2024

W. Mathworks. Matlab Optimization Toolbox, 2014

X. National Oceanic and Atmospheric Administration (NOAA). National Data Buoy Center. NASA - Langley Research Center - Turbulence Modeling Resource.
url: https://www.ndbc.noaa.gov. Date accessed: 10 Jan 2024

Y. Longest Common Subsequence (LCS). 2024.
url: https://www.geeksforgeeks.org/longest-common-subsequence. Date accessed: 13 March 2024

A

Derivation of the helicopter model

This chapter elaborates on the helicopter model. First, the coordinate systems are explained which are needed to derive the equations of motion. After that, the helicopter dynamics in wind are derived from Newton's second law.

A.1. Coordinate systems

Ruijgrok utilizes four right-handed and rectangular Cartesian coordinate systems to describe the motion of an aerial vehicle [15]. In these coordinate systems, all displacements, velocities and accelerations are positive along the positive senses of the axes and angles are positive in clockwise direction, looking in the positive direction of the appropriate axis. The four coordinate systems are (i) the Earth Fixed axis or Ground axis system $\{\underline{E}_g\}$, (ii) the Moving Earth axis system $\{\underline{E}_e\}$, (iii) the Body axis system $\{\underline{E}_b\}$ and (iv) the Air-Path axis system $\{\underline{E}_a\}$. To simplify the equations of motion for helicopters, the body axis system $\{\underline{E}_b\}$ is often replaced by the Main-Rotor axis system $\{\underline{E}_{mr}\}$.

A.1.1. Earth Fixed (i) and Moving Earth (ii) axis systems

The Earth Fixed or Ground axis system $\{\underline{E}_g\}$ and Moving Earth axis system $\{\underline{E}_e\}$ are used to define the helicopter's motion and are depicted in Figure A.1. The origin of The Earth Fixed or Ground axis system is at any point on the Earth's surface. The $\underline{X}_g$ and $\underline{Y}_g$ axes lie in the horizontal plane on the Earth's surface and the $\underline{Z}_g$ axis points vertically upwards, which is different from Ruijgrok. The Moving Earth axis system describes the trajectory of an aerial vehicle relative to the Earth. The origin of this system is the centre of gravity of the aerial vehicle and the $\underline{X}_e$, $\underline{Y}_e$ and $\underline{Z}_e$ axes are parallel to the corresponding axes of the Earth Fixed system. However, this definition may vary in other studies. Normally, the attitude of the helicopter is described relative to the Moving Earth system by three successive rotations of the yaw (ψ), pitch (θ) and roll (ϕ) angles. These angles are not considered due to the implementation of a point-mass model, which is why only the flight path relative to the Earth is relevant.

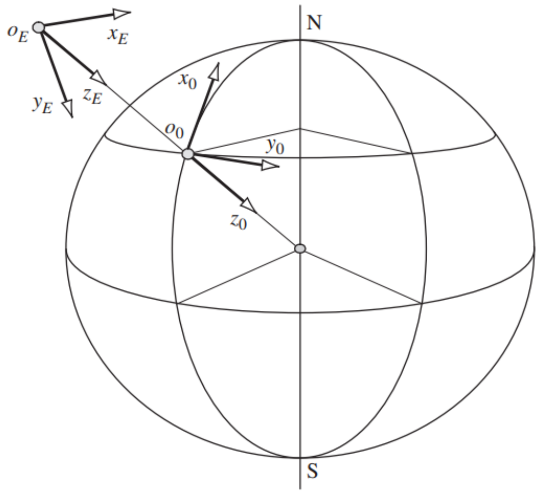

Figure A.1: Earth Fixed and Moving Earth axis systems [84]

A.1.2. Main-Rotor axis system (iii)

The Main-Rotor axis system $\{\underline{E}_{mr}\}$ is often used instead of the Body axis system $\{\underline{E}_b\}$ to simplify equations of motion for helicopters, as shown in Figure A.2. This coordinate system is used to derive the helicopter's equations of motion. The main advantage of this system is that the thrust vector $\underline{T}$ is aligned with the $\underline{Z}_{mr}$ axis, which is positive pointing outwards of the main rotor hub. The $\underline{X}_{mr}$ axis is perpendicular to the $\underline{Z}_{mr}$ axis and lies in the plane of symmetry. The $\underline{Y}_{mr}$ axis is positive pointing to the left of the helicopter, which is not necessarily parallel to the left wing. The angles β_{long} and β_{lat} convert the thrust vector from the Main-Rotor to the Moving Earth axis system.

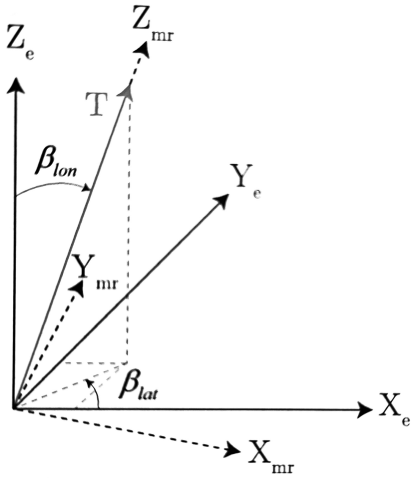

Figure A.2: Main-Rotor axis system relative to the Moving Earth axis system [60]

A.1.3. Air-Path axis system (iv)

The last coordinate system is the Air-Path axis system $\{\underline{E}_a\}$ in which the velocity vector is placed, as illustrated in Figure A.3. This system is used to compute the flight path angle γ and heading angle χ along a trajectory, as these angles transform the Air-Path system into the Moving Earth system. The bank angle μ is not depicted due to the alignment of the velocity vector with the $\underline{X}_a$ axis. The origin of this coordinate system is the centre of gravity of the aerial vehicle and the $\underline{Z}_a$ is taken in the plan of symmetry and is positive upwards, which differs from the convention used by Ruijgrok. The $\underline{Y}_a$ is positive to port-side.

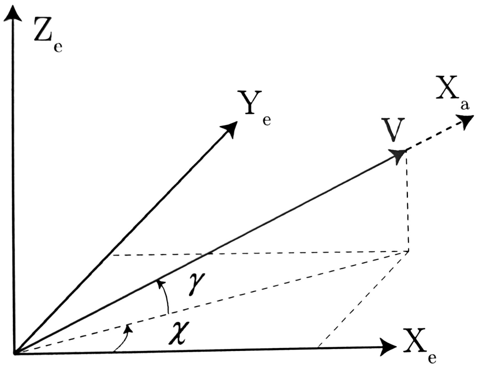

Figure A.3: Air-Path axis system relative to the Moving Earth axis system [60]

From this figure the azimuth angle χ and flight path angle γ can be derived:

$$\tan(\chi) = \frac{v}{u}$$
$$\tan(\gamma) = \frac{w}{V_{xy}} \text{ or } \sin(\gamma) = \frac{w}{V} \tag{A.1}$$

Where u, v and w are the velocity components in the X, Y and Z directions, respectively. Besides, $V_{xy} = \sqrt{u^2+v^2}$ is the horizontal component of the total velocity $V = \sqrt{u^2+v^2+w^2}$.

A.2. Derivation of the equations of motion

The generic equations of motions of a helicopter in the Earth reference frame can be written as:

$$(m\ddot{x})\{\underline{E}_e\} = (\underline{F}_{mr} + \underline{F}_{fus})\{\underline{E}_e\} \tag{A.2}$$

In this equation, m is the mass of the helicopter, $\ddot{x}$ the accelerations in x, y and z directions, $\underline{F}_{mr}$ the force on the main rotor and $\underline{F}_{fus}$ the forces acting on the fuselage. All parameters are expressed in the helicopter's moving earth axis system, meaning integrating the accelerations results in velocities relative to the ground.

A.2.1. Forces on the Main Rotor

A dominant force acting on the helicopter is the thrust $\underline{T}$ generated by the main rotor blades. Although a drag $\underline{H}$ and side force $\underline{S}$ act on the main rotor of a helicopter as well, they are neglected as the thrust is more dominant [60]. The thrust vector $\underline{T}$ is defined in the main rotor axis system $\{\underline{E}_{mr}\}$, which is shown in Figure A.2. Therefore a transformation in axes systems has to be done to convert the thrust to the moving earth reference system $\{\underline{E}_e\}$. This can be done by using the two angles β_{long} and β_{lat}, which are respectively the angles between the X_e axis and the component of $\underline{T}$ projected on the $\{\underline{E}_e\}$ XY-plane and the angle between the Z_b and Z_e axes. The relation between the thrust components in the two reference systems is shown in Equation A.3.

$$\underline{F}_{mr} = \begin{bmatrix} 0 \\ 0 \\ T \end{bmatrix} \{\underline{E}_{mr}\} = \begin{bmatrix} T_x \\ T_y \\ T_z \end{bmatrix} \{\underline{E}_e\} = \begin{bmatrix} T\sin\beta_{long}\cos\beta_{lat} \\ T\sin\beta_{long}\sin\beta_{lat} \\ T\cos\beta_{long} \end{bmatrix} \{\underline{E}_e\} \tag{A.3}$$

Other terms can substitute the thrust and drag forces. Firstly, the thrust T can be defined as [58]:

$$T = C_T\rho(\Omega R)^2\pi R^2 \tag{A.4}$$

Here, ρ is the air density, ΩR is the rotor tip speed and πR^2 is the rotor disc area. Furthermore, C_T is the thrust coefficient and can be decomposed along the three axes directions:

$$\begin{aligned} C_x &= C_T\sin\beta_{long}\cos\beta_{lat} \\ C_y &= C_T\sin\beta_{long}\sin\beta_{lat} \\ C_z &= C_T\cos\beta_{long} \\ C_T &= \sqrt{C_x^2+C_y^2+C_z^2} \end{aligned} \tag{A.5}$$

The directional thrust coefficients can substitute the trigonometric functions containing β_{long} and β_{lat} in Equation A.3:

$$\begin{aligned} \cos\beta_{lat} &= \frac{C_x}{C_{xy}} \quad & \cos\beta_{long} &= \frac{C_z}{C_T} \\ \sin\beta_{lat} &= \frac{C_y}{C_{xy}} \quad & \sin\beta_{long} &= \frac{C_{xy}}{C_T} \end{aligned} \tag{A.6}$$

The resulting equations for the forces on the main rotor are:

$$\underline{F}_{mr} = \begin{bmatrix} 0 \\ 0 \\ T \end{bmatrix} \{\underline{E}_{mr}\} = \begin{bmatrix} C_x\rho(\Omega R)^2\pi R^2 \\ C_y\rho(\Omega R)^2\pi R^2 \\ C_z\rho(\Omega R)^2\pi R^2 \end{bmatrix} \{\underline{E}_e\} \tag{A.7}$$

A.2.2. Forces on the Fuselage

The dominant forces acting on the helicopter's fuselage are the weight $\underline{W}$ and (parasite) drag $\underline{D}$:

$$\underline{F}_{fus}\{\underline{E}_e\} = \underline{D}\{\underline{E}_e\} + \underline{W}\{\underline{E}_e\} \tag{A.8}$$

Per definition, the weight is directed towards the Earth's center of gravity, hence in the negative Z_e axis:

$$\underline{W} = \begin{bmatrix} 0 \\ 0 \\ -W \end{bmatrix} \{\underline{E}_e\} = \begin{bmatrix} 0 \\ 0 \\ -mg \end{bmatrix} \{\underline{E}_e\} \tag{A.9}$$

Similarly, the drag force is by definition directed opposite to the velocity vector V_{TAS}, thus pointing in the negative X_a axis. Drag depends on the total airspeed of a vehicle, which means that wind should be included. From Figure A.3, it can be seen that the velocity vector in $\{\underline{E}_e\}$ is defined by the aerodynamic flight path and heading angles γ and χ. The transformations of the velocity and drag force vectors are depicted below.

$$\begin{aligned} \underline{V}_{TAS} &= \begin{bmatrix} V_{TAS} \\ 0 \\ 0 \end{bmatrix} \{\underline{E}_a\} = \begin{bmatrix} V_x \\ V_y \\ V_z \end{bmatrix} \{\underline{E}_e\} = \begin{bmatrix} V_{TAS}\cos\gamma\cos\chi \\ V_{TAS}\cos\gamma\sin\chi \\ V_{TAS}\sin\gamma \end{bmatrix} \{\underline{E}_e\} \\ \underline{D} &= \begin{bmatrix} -D \\ 0 \\ 0 \end{bmatrix} \{\underline{E}_a\} = \begin{bmatrix} -D\cos\gamma\cos\chi \\ -D\cos\gamma\sin\chi \\ -D\sin\gamma \end{bmatrix} \{\underline{E}_e\} \end{aligned} \tag{A.10}$$

Next, the parasite drag force is defined by [66].

$$D = f_e \frac{1}{2} \rho V_{TAS}^2 \tag{A.11}$$

In this equation, f_e is the equivalent flat plate area and V_{TAS} the true airspeed, which combines the total helicopter ground and wind speeds. The relation between the three velocities is expressed below [64]:

$$\underline{V}_{vehicle/ground} = \underline{V}_{vehicle/air} + \underline{V}_{air/ground} \tag{A.12}$$

This relation states that the velocity of a vehicle with respect to the ground is the vectorial sum of the vehicle's airspeed and the wind speed. The equation can be rearranged to find the Total Airspeed V_{TAS}:

$$V_{TAS} = \left|\underline{V}_g - \underline{V}_w\right| = \sqrt{(u-u_w)^2 + (v-v_w)^2 + (w-w_w)^2} \tag{A.13}$$

Furthermore, other terms can exchange the trigonometric relations for γ and χ:

$$\begin{aligned} \cos\gamma &= \frac{V_{xy}}{V_{TAS}} \quad & \cos\chi &= \frac{V_x}{V_{xy}} \\ \sin\gamma &= \frac{V_z}{V_{TAS}} \quad & \sin\chi &= \frac{V_y}{V_{xy}} \end{aligned} \tag{A.14}$$

Where $V_{xy} = \sqrt{V_x^2 + V_y^2}$ and $C_{xy} = \sqrt{C_x^2 + C_y^2}$ are respectively the horizontal components of the total airspeed and thrust coefficient. Moreover, the velocities $V_x = u - u_w$, $V_y = v - u_w$ and $V_z = w - w_w$ are the total airspeed components decomposed along the three axes directions.

The forces on the fuselage can be written as:

$$\underline{F}_{fus}\{\underline{E}_e\} = \underline{D}\{\underline{E}_e\} + \underline{W}\{\underline{E}_e\} = \begin{bmatrix} -f_e\frac{1}{2}\rho(u-u_w)V_{TAS} \\ -f_e\frac{1}{2}\rho(v-v_w)V_{TAS} \\ -f_e\frac{1}{2}\rho(w-w_w)V_{TAS} \end{bmatrix} \{\underline{E}_e\} + \begin{bmatrix} 0 \\ 0 \\ -mg \end{bmatrix} \{\underline{E}_e\} \tag{A.15}$$

A.3. Total Equations of Motion

Additional differential equations that describe the development of the helicopter position are required to complete the model. The rate of change of position is equal to the helicopter's ground velocity in that direction:

$$\begin{aligned}\dot{x} &= u \\ \dot{y} &= v \\ \dot{z} &= w\end{aligned} \tag{A.16}$$

By taking into account the helicopter's ground velocity components $\underline{\dot{x}} = \begin{bmatrix} u & v & w \end{bmatrix}^T$, Equation A.2, Equation A.7 and Equation A.15 can be combined to complete the set of equations of motion that describe the helicopter's accelerations, velocities and position relative to the ground as a function of time:

$$\begin{aligned}\dot{u} &= \frac{1}{m}\left(C_x\rho(\Omega R)^2\pi R^2 - f_e\frac{1}{2}\rho\,(u-u_w)V_{TAS}\right) \\ \dot{v} &= \frac{1}{m}\left(C_y\rho(\Omega R)^2\pi R^2 - f_e\frac{1}{2}\rho\,(v-v_w)V_{TAS}\right) \\ \dot{w} &= \frac{1}{m}\left(C_z\rho(\Omega R)^2\pi R^2 - f_e\frac{1}{2}\rho\,(w-w_w)V_{TAS} - mg\right) \\ \dot{x} &= u \\ \dot{y} &= v \\ \dot{z} &= w\end{aligned} \tag{A.17}$$

This page is intentionally left blank.

B

Helicopter Parameters

This appendix covers the derivation of some helicopter parameters and will conclude with a table containing all values. Some parameters of the PH-1AA Orange Eye helicopter are not clearly defined or yet known, such as main rotor friction drag coefficient, maximum engine thrust and power and other airframe restrictions such as never-exceed speeds. These parameters are estimated or assumed because of their importance for the helicopter model.

Firstly, many wind tunnel experiments have studied the friction drag coefficient of NACA0012 airfoil profiles [85]. Although these studies have shown that the coefficient is a function of other flow and airfoil characteristics, such as Reynolds number, surface roughness and lift coefficient, it is possible to estimate a mean value for the friction drag quantity as a function of the maximum thickness-to-chord ratio t/c [86]. Substituting the maximum thickness-to-chord ratio of $\frac{t}{c} = \frac{12}{100}$ of a NACA0012 airfoil into Equation B.1 gives a mean profile drag coefficient of $c_d = 0.010$.

$$c_d \approx 0.007 + 0.025\frac{t}{c} \tag{B.1}$$

Secondly, the equivalent flat plate area f_e is estimated from Figure B.1. A helicopter's gross weight of $m = 100\,\mathrm{kg}$, equivalent to $220.46\,\mathrm{lb}$, results in an equivalent flat plate area of $f_e = 2\,\mathrm{ft}^2 = 0.1858\,\mathrm{m}^2$.

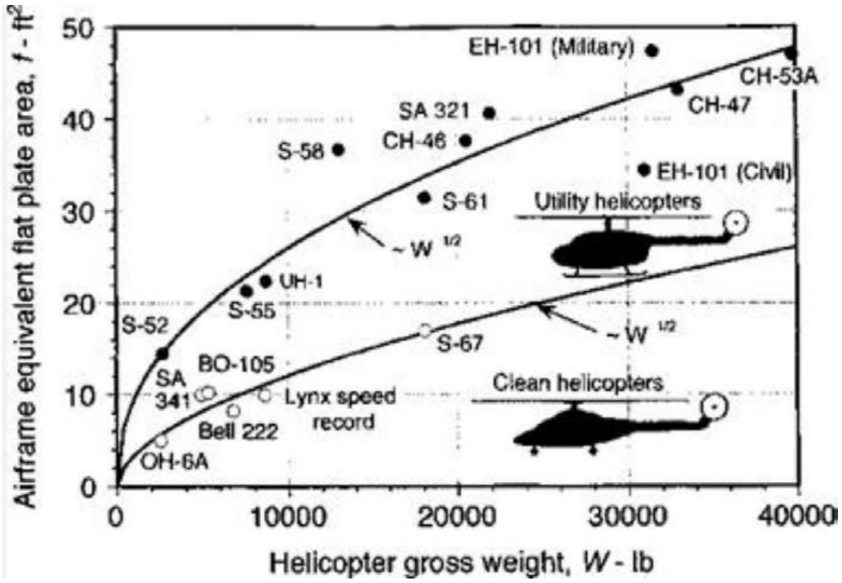

Figure B.1: Equivalent flat plate area as a function of Gross Weight [87]

Furthermore, engine performance parameters have not been studied yet by NLR. However, reliable estimations of the maximum thrust and power available are required as path constraints. Therefore, a Power Reserve Ratio (PRR) of 10% is assumed. This quantity defines the helicopter's power surplus when hovering at sea level and can thus be used to estimate the maximum power available P_a. To accompany margins for control secondary power requirements, a conservative number is assumed as typical values of the PRR are in the range of 20% to 30% [88]. The required power to hover at sea level is computed using Equation 4.5 (for clarity repeated below) and is equal to $P_{req,hov}$ = $9.528\,$kW. Using the PRR, the helicopter's available power is equal to $P_a = 10.48$kW.

$$C_{P_{req}} = C_T\sqrt{\frac{1}{2}C_W}(K_{ind}f_G\overline{v}_i + \overline{U_C}) + \frac{1}{8}\sigma c_d(1 + 4.65\tilde{\mu}^2)$$

The actuator disk theory also provides a way to calculate the power required to hover and can be used as a comparison. Equation B.2 defines this expression in which the ideal power to drive the rotor in hover can be computed [66]. According to this expression, the ideal power to hover equals P_{id} = $6.647\,$kW.

$$P_{id} = Tv_i = W\sqrt{\frac{W}{2\rho\pi R^2}} \tag{B.2}$$

Using the fact that $T = W$ and $v_{i,hov} = \sqrt{\frac{W}{2\rho\pi R^2}}$ in hover. Combining this ideal power with the actual power required to hover, a Figure of Merit of $M = 0.698$ is found (Equation B.3), which is a realistic value [66].

$$M = \frac{P_{id}}{P_{hov}} \tag{B.3}$$

The maximum thrust coefficient is calculated using the actuator disk theory for a helicopter in hover with the assumed power available, as expressed in Equation B.4 [66]. This results in a maximum coefficient of $C_{T_{max}}$ = 0.0059 at sea level conditions.

$$C_{T_{max}} = \frac{T_{hov}}{\rho(\Omega R)^2\pi R^2} \quad \text{with} \quad T_{hov} = \frac{P_a}{M}v_{i,hov} \tag{B.4}$$

Lastly, the helicopter's cruise and never exceed speeds are evaluated for the optimization problem. The maximum range velocity is the velocity where the slope of the power-velocity curve's tangent is lowest. As can be seen from Figure B.2, this velocity is equal to V_{range} = $27.01\,$m/s or $52.50\,$kts. The never-exceed speed of this helicopter is reached when the advance ratio of the main rotor blade is equal to $\tilde{\mu} = \frac{V_{TAS}}{\Omega R} = 0.4$ [66]. For this helicopter, this results in a never-exceed speed of V_{NE} = $52.32\,$m/s or $101.69\,$kts. Even though the maximum power available restricts the maximum velocity to a value of V_{max} = $38.56\,$m/s or $74.95\,$kts, the never-exceed speed could be reached during a nosedive by converting potential energy to kinetic energy.

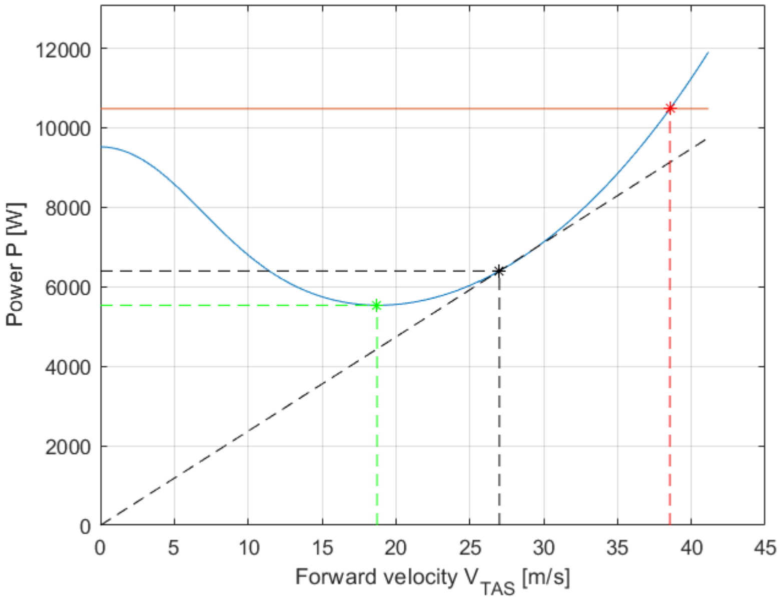

Figure B.2: Power curve as function of true airspeed evaluated for the PH-1AA Orange Eye helicopter flying at an altitude of $z = 20$ m (approach level) and with ground effect. Lines of various colours indicate the power curve, minimum power and maximum endurance velocity, maximum range power and velocity, maximum power available and maximum velocity.

Table B.1: PH-1AA Orange Eye parameters

Parameter	**Symbol**	**Value**	**Unit**
Mass	m	100	kg
Main rotor rotational speed	Ω	750 (78.5398)	rpm (rad/s)
Main rotor radius	R	1.6652	m
Main rotor blade chord	c	0.11	m
Main rotor blade friction drag coefficient	c_d	0.010 (NACA0012)	-
Equivalent flat plate area	f_e	2 (0.1858)	ft^2 (m^2)
Number of blades	N_b	3	-
Height from ground to main rotor hub	H_R	0.9251	m
Induced power factor	K_{ind}	1.15	-
Power Reserve Ratio	PRR	10	%
Figure of Merit	M	0.6977	-
Power available (sea level)	P_a	10.48	kW
Maximum thrust coefficient	$C_{T_{max}}$	0.0059	-
Maximum endurance velocity	V_{endur}	18.78 (36.50)	m/s (kts)
Maximum range velocity	V_{range}	27.01 (52.50)	m/s (kts)
Maximum velocity	V_{max}	38.56 (74.95)	m/s (kts)
Never-exceed speed	V_{NE}	52.32 (101.69)	m/s (kts)

C

Helicopter approach procedures

Straight-in

The straight-in approach is also used for degraded modes and/or single-engine conditions as an additional emergency landing procedure. In an emergency, the helicopter weight should be minimized before starting the approach to the ship to reduce power requirements. In general conditions, this is not necessary. The FDO positions itself either to port or starboard side of the ship's centre line to maintain eye contact with the pilot flying. The pilot flying can either be seated left or right[5]. This flight path can be divided into two distinct segments.

- **Approach;** The helicopter approaches the ship from astern along the ship's centre line until the helicopter is above the landing spot.
- **Landing;** The helicopter descends to land on the ship's deck. After touchdown, the deck-lock system is engaged immediately to secure the helicopter on deck.

The take-off procedure can be carried to either the port or starboard side and is as follows:

- **Alignment;** If required, align the helicopter's longitudinal axis with the ship's centre line so both headings are equal.
- **Take-off;** The helicopter ascents to hover position above the landing spot. This hover position is approximately 10 ft above the flight deck. The helicopter maintains the ship's forward speed and heading during this hover.
- **Transition;** The helicopter adjusts its heading by 30° to 45° and flies forward with a climb away from the ship.

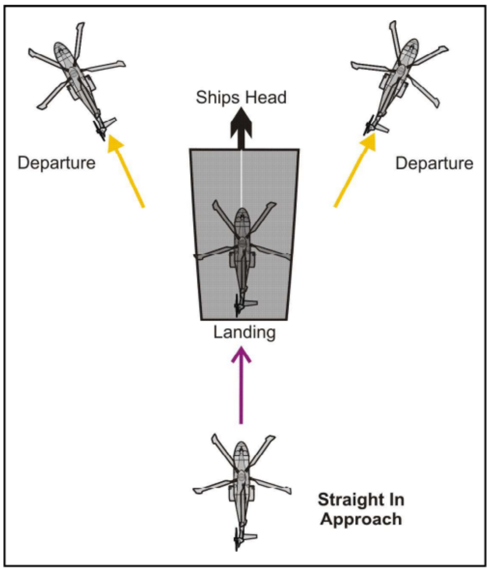

Figure C.1: Straight-in procedure [3]

Oblique procedure

In the oblique procedure, the helicopter's longitudinal axis is aligned at a $45°$ angle with the ship's heading. This procedure can be applied towards starboard or port side of the ship and is at the pilot's discretion to choose either one. In case the pilot flying is positioned right, the manoeuvre will be flown from starboard side. The flight path can be divided into three segments.

- **Approach;** The helicopter approaches the ship from the leeward side at a $45°$ angle with the ship's centre line.
- **Transition;** The helicopter continues its flight to the hover position above the landing spot. In the hover position, the helicopter maintains an altitude of approximately $10\,\mathrm{ft}$ above the flight deck and a $45°$ deviation from the ship's heading.
- **Landing;** After the bridge's approval the helicopter descends to land on the ship's deck. After touchdown, the deck-lock system is engaged immediately to secure the helicopter on deck.

After the bridge's approval, the take-off is carried out as follows:

- **Alignment;** If required, align the helicopter's longitudinal axis at a $45°$ angle with the ship's centre line.
- **Take-off;** The helicopter ascents to hover position above the landing spot. This hover position is approximately $10\,\mathrm{ft}$ above the flight deck. The helicopter maintains a $45°$ deviation in heading during this hover. If necessary the helicopter moves sideways until it is clear of the ship's superstructure and other obstacles.
- **Transition;** The helicopter flies forward with a climb away from the ship.

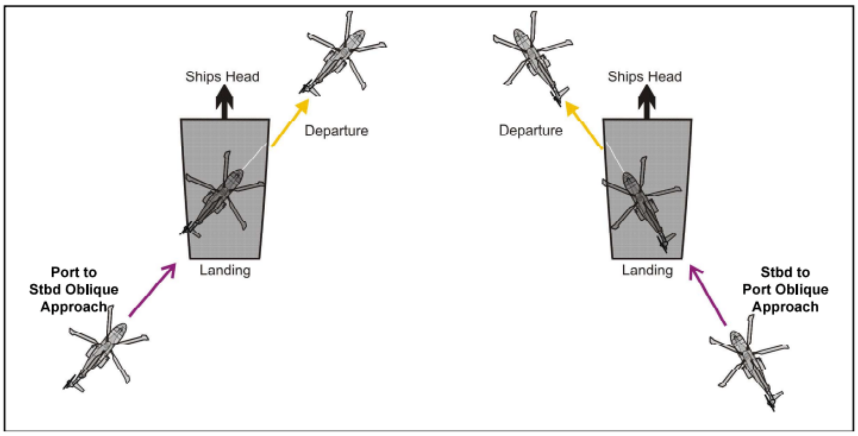

Figure C.2: Oblique procedure [3]

Lateral procedure

In the lateral procedure, the helicopter is aligned with the ship's heading and can either be applied from starboard or port side of the ship. The helicopter pilot decides from which side the ship will be approached. However, the lateral-port procedure is mostly used since generally the pilot flying is positioned in the right seat, enabling the best visuals with the ship. The entire approach can be divided into three segments.

- **Approach;** The helicopter approaches the ship to hover wait position perpendicular to the landing spot. The hover wait position is approximately 3/4 rotor diameter next to the ship and 10 ft above the flight deck. The helicopter's longitudinal axis is parallel to the ship's centre line so both headings are equal.
- **Transition;** The helicopter makes a side-step manoeuvre from the hover wait position to hover above the landing spot. During this manoeuvre, the helicopter maintains its forward speed and altitude. The hover height above the landing spot is approximately 10 ft.
- **Landing;** The helicopter descends to land on the ship's deck. After touchdown, the deck-lock system is engaged immediately to secure the helicopter on deck.

After the bridge's approval, the take-off is carried out as follows:

- **Alignment;** If required, align the helicopter's longitudinal axis with the ship's centre line so both headings are equal.
- **Take-off;** The helicopter ascents to hover position above the landing spot. This hover position is approximately 10 ft above the flight deck. The helicopter maintains the ship's forward speed and heading during this hover.
- **Transition;** The helicopter manoeuvres sideways with a simultaneous slow climb until the helicopter is approximately 1.5 rotor diameter perpendicular to the landing spot. The helicopter yaws approximately 30° away from the ship and flies away with a climbing path.

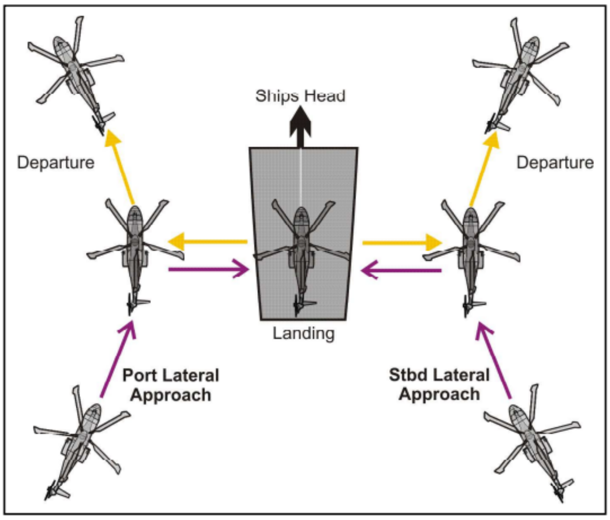

Figure C.3: Lateral procedure [3]

45° Procedure

The 45° approach is similar to the lateral procedure, the key difference is the transition phase towards the helicopter deck. During the entire approach, the helicopter is aligned with the ship's heading and can either be applied from starboard or port side of the ship. Because generally the pilot flying is positioned in the right seat the 45port approach is more common. The entire approach can be divided into three segments.

- **Approach;** The helicopter approaches the ship to hover wait position at a 45° relative angle to the landing spot. The hover wait position is approximately 10 ft above the flight deck. The helicopter's longitudinal axis is parallel to the ship's centre line so both headings are equal.
- **Transition;** The helicopter makes a 45°-step manoeuvre from the hover wait position to hover above the landing spot. During this manoeuvre, the helicopter maintains its heading and altitude. The hover height above the landing spot is approximately 10 ft.
- **Landing;** The helicopter descends to land on the ship's deck. After touchdown, the deck-lock system is engaged immediately to secure the helicopter on deck.

The take-off procedure can be carried to either port or starboard side and is as follows:

- **Alignment;** If required, align the helicopter's longitudinal axis with the ship's centre line so both headings are equal.
- **Take-off;** The helicopter ascents to hover position above the landing spot. This hover position is approximately 10 ft above the flight deck. The helicopter maintains the ship's forward speed and heading during this hover.
- **Transition;** The helicopter adjusts its heading by 30° to 45° and flies forward with a climb away from the ship.

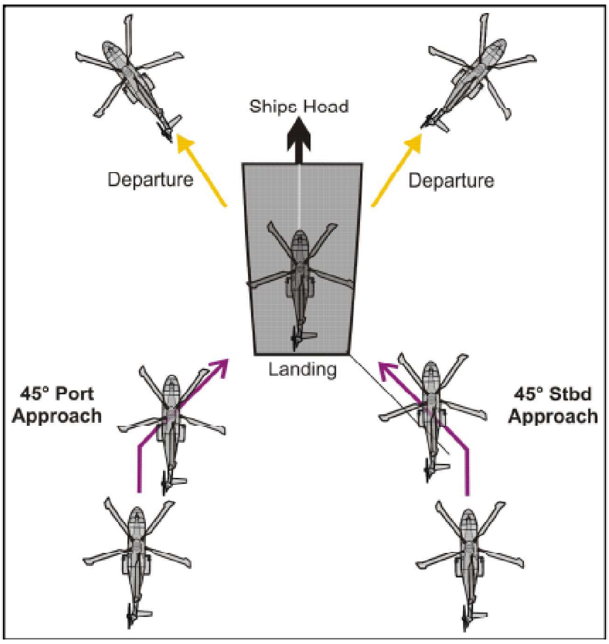

Figure C.4: 45° Procedure [3]

Athwartships procedure

In the athwartships procedure the helicopter's longitudinal axis is aligned at a 90° angle with the ship's heading. This procedure can also be applied towards starboard or port side of the ship and is at the pilot's discretion to choose either one. In case the pilot flying is positioned right, the manoeuvre will be flown from starboard to port. The flight path can be divided into three segments.

- **Approach;** The helicopter approaches the ship from the leeward side at a 90° angle with the ship's centre line.
- **Transition;** The helicopter continues its flight to the hover position above the landing spot. In the hover position, the helicopter maintains an altitude of approximately 10 ft above the flight deck and a 90° deviation from the ship's heading.
- **Landing;** After the bridge's approval, the helicopter descends to land on the ship's deck. After touchdown, the deck-lock system is engaged immediately to secure the helicopter on deck.

The take-off is carried out as follows:

- **Alignment;** If required, align the helicopter's longitudinal axis at a 90° angle with the ship's centre line.
- **Take-off and Transition;** The helicopter ascents with the 90° heading deviation. This is followed by a forward transition with a climb away from the ship

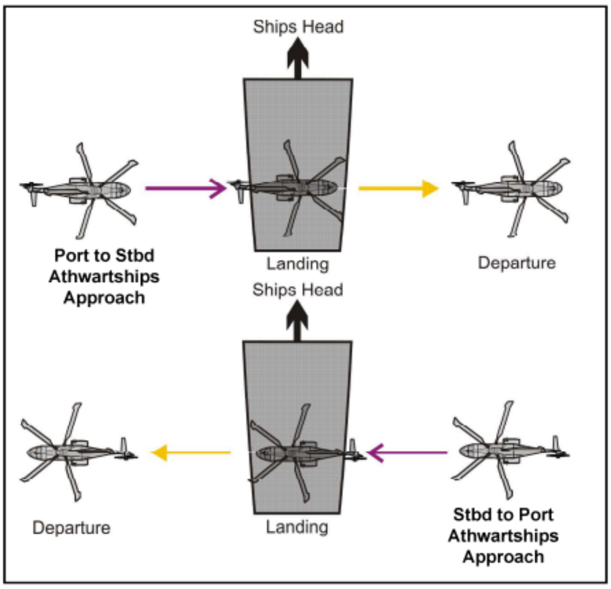

Figure C.5: Athwartships Procedure [3]

D

LCSS Algorithm

This appendix contains the Longest Common Subsequence (LCSS) algorithm based on a Bottom-Up Tabulation method[Y].

Algorithm 1: $[C, S] = LCSS(A, B)$

```
Input: $A = [x_A, y_A, z_A], B = [x_B, y_B, z_B]$
Parameters: $\epsilon, \delta$
Output: $C, S$
$m = rows(A)$                                   ▷ Initialize parameters
$n = rows(B)$
$L = [m+1, n+1]$                                ▷ Initialize matrix of size (m+1)×(n+1)
for $i \leftarrow 1$ to $m+1$ do
    for $j \leftarrow 1$ to $n+1$ do
        if $i == 1$ or $j == 1$ then
            $L(i, j) = 0$
        else if $D_\infty(A_{[i-1]}, B_{[j-1]}) \leq \epsilon$ and $|i-j| \leq \delta$ then
            $L(i, j) = L_{[i-1, j-1]} + 1$
        else
            $L(i, j) = \max[(L_{[i-1, j]}, L_{[i, j-1]}]$
        end
    end
end
$C = L_{[m+1, n+1]}$                            ▷ Contains the length of the LCSS of $A(1:m)$ and $B(1:n)$
$S = \frac{C}{\min[m, n]}$                      ▷ Normalization
```

E

Beaufort Wind Scale

True winds are categorized on the Beaufort Wind Scale, which was created in 1805 by Britain's Admiral Sir Francis Beaufort (1774-1857)[J]. The scale relates true wind speed to observed conditions on land or at sea and ranges from 0 (no wind) to 12 (approaching hurricane phenomena). The table in this appendix provides the Beaufort Wind Scale and its specifications for each wind speed. It is important to note that these speeds are mean speeds, typically averaged over 10 minutes and do not involve wind gusts.

Table E.1: The Beaufort Wind Scale

Wind force	**Description**	**Wind speed**		**Specifications**	
		km/h	kts	For use at sea	For use on land
0	Calm	0-1	0-1	Sea like a mirror	Calm; smoke rises vertically
1	Light Air	1-5	1-3	Ripples with the appearance of scales are formed, but without foam crests	Direction of wind shown by smoke drift, but not by wind vanes.
2	Light Breeze	6-11	4-6	Small wavelets, still short, but more pronounced. Crests have a glassy appearance and do not break.	Wind felt on face; leaves rustle; ordinary vanes moved by wind.
3	Gentle Breeze	12-19	7-10	Large wavelets. Crests begin to break. Foam of glassy appearance. Perhaps scattered white horses.	Leaves and small twigs in constant motion; wind extends light flag.
4	Moderate Breeze	20-28	11-16	Small waves, becoming larger; fairly frequent white horses.	Raises dust and loose paper; small branches are moved.
5	Fresh Breeze	29-38	17-21	Moderate waves, taking a more pronounced long form; many white horses are formed.	Small trees in leaf begin to sway; crested wavelets form on inland waters.
6	Strong Breeze	38-49	22-27	Large waves begin to form; the white foam crests are more extensive everywhere.	Large branches in motion; whistling heard in telegraph wires; umbrellas used with difficulty.
7	Near Gale	50-61	28-33	Sea heaps up and white foam from breaking waves begins to be blown in streaks along the direction of the wind.	Whole trees in motion; inconvenience felt when walking against the wind.
8	Gale	62-74	34-40	Moderately high waves of greater length; edges of crests begin to break into spindrift. The foam is blown in well-marked streaks along the direction of the wind.	Breaks twigs off trees; generally impedes progress.

Wind force	**Description**	**Wind speed**		**Specifications**	
		km/h	kts	For use at sea	For use on land
9	Strong Gale	75-88	41-47	High waves. Dense streaks of foam along the direction of the wind. Crests of waves begin to topple, tumble and roll over. Spray may affect visibility	Slight structural damage occurs (chimney pots and slates removed)
10	Storm	89-102	48-55	Very high waves with long overhanging crests. The resulting foam, in great patches, is blown in dense white streaks along the direction of the wind. The whole surface of the sea takes on a white appearance. The tumbling of the sea becomes heavy and shock-like. Visibility affected.	Seldom experienced inland; trees uprooted; considerable structural damage occurs.
11	Violent Storm	103-117	56-63	Exceptionally high waves (small and medium-size ships might be for lost for some time to view behind the waves). The sea is completely covered with long white patches of foam lying along the direction of the wind. Everywhere the edges of the wave crests are blown into froth. Visibility affected.	Very rarely experienced; accompanied by wide-spread damage.
12	Hurricane	118+	64+	The air is filled with foam and spray. The sea is completely white with driving spray; visibility is very seriously affected.	Devastation. Hurricane categories 1-5 in Saffir-Simpson Hurricane Scale

F

Extra Figures

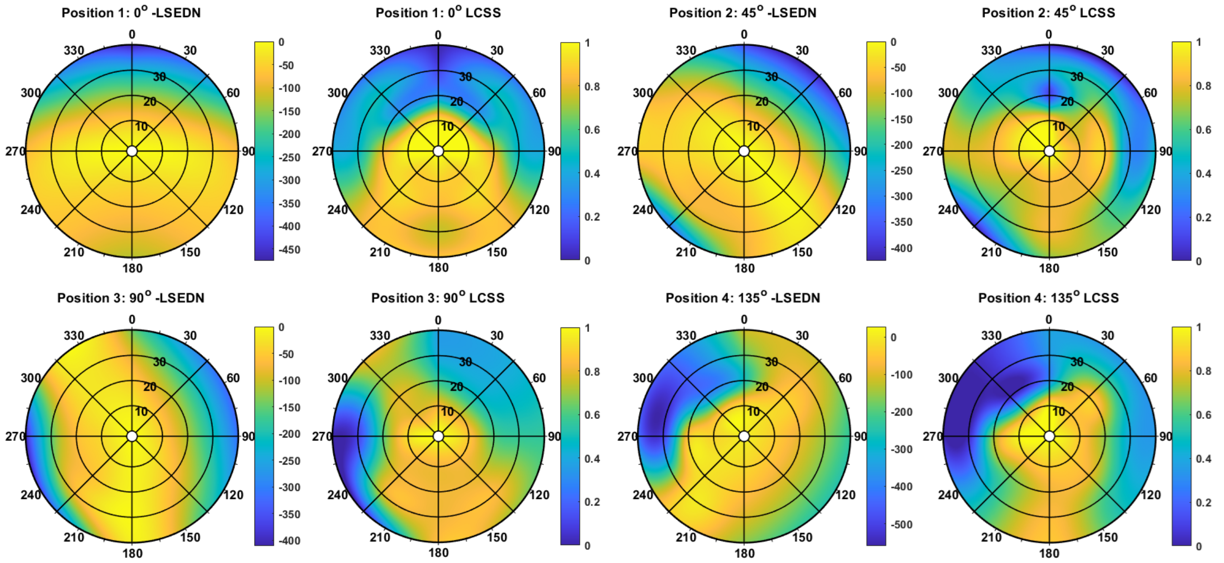

Figure F.1: Lock-Step Euclidean Distance Normalized (LSEDN) and Longest Common SubSequence (LCSS) geometric total path similarity measures of optimized trajectories in a uniform wind field compared to no wind conditions for all helicopter starting positions

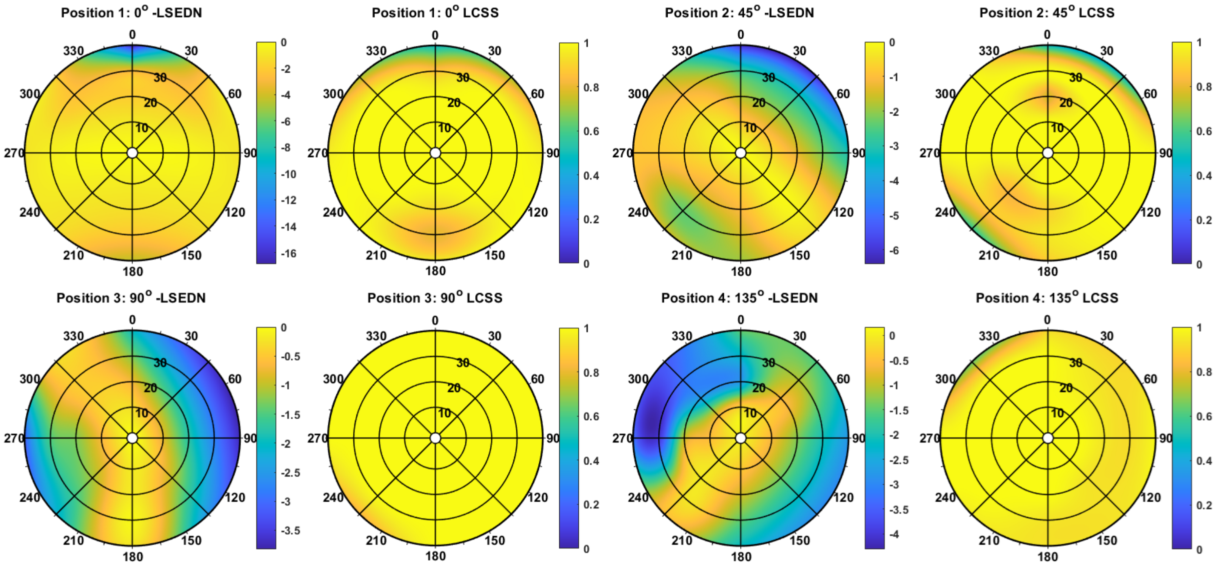

Figure F.2: Lock-Step Euclidean Distance Normalized (LSEDN) and Longest Common SubSequence (LCSS) geometric vertical path similarity measures of optimized trajectories in a uniform wind field compared to no wind conditions for all helicopter starting positions